NTNU – Trondheim
Norwegian University of
Science and Technology

The effects of seismic anisotropy and upscaling on rock physics interpretation and AVO analysis

Mayowa Adeleye

Petroleum Geosciences
Submission date: June 2015
Supervisor: Alexey Stovas, IPT
Co-supervisor: Per Avseth, IPT

Norwegian University of Science and Technology
Department of Petroleum Engineering and Applied Geophysics

NTNU
Norwegian University of
Science and Technology

The effects of seismic anisotropy and upscaling on the rock physics interpretation and its implications on AVO analysis

Mayowa Michael Adeleye

Petroleum Geosciences

Submission date: June 2015

Supervisor: Alexey Stovas, IPT

Co-supervisor: Per Avseth, Tullow oil

Norwegian University of Science and Technology

Department of Petroleum Engineering and Applied Geophysics

The effects of seismic anisotropy and upscaling on the rock physics interpretation and its implications on AVO analysis

by

Mayowa Michael Adeleye

A thesis presented to the Department of Petroleum Engineering and Applied Geophysics,
Norwegian University of Science and Technology
in Partial fulfillment of the Requirements for the Master of Science Degree in fulfillment
of the Petroleum Geophysics

June, 2015

Acknowledgements

I would like to express my special appreciation and thanks to my supervisors, Professor Alexey Stovas and Professor Per Avseth, for their guidance, encouragement and valuable comments through every phase of this work. It has been an honour and privilege to be one of their students. My special thanks to the lecturers and colleagues at the Department of Petroleum Engineering and Applied Geophysics, NTNU for their discussion and valuable input.

I am extremely thankful and indebted to my parents, Christopher and Titilayo Adeleye and my siblings for their unconditional and continuous support, prayers and encouragement. I am also grateful to the lady I cherished most, Caroline, for her patience and support throughout this venture. I would like to thank my brother, Solomon Adeleke for proofreading and all the encouraging words during the course of this programme and also my appreciation goes to his entire family.

I thank all the people with whom I had the privilege to share great times with at NTNU. The list is large, but some of the names that come to my mind right now are Samuel, Isabel, Ola, Stian, Emmanuel, Mohammed, Matteo, Kome... My sense of gratitude to one and all, who directly or indirectly, have lent their hand in this venture.

Above all, I could not have completed this programme without the help of Almighty God, whose mercy, grace and love are sufficient and abundant during the period of this masters programme.

Abstract

In seismic reservior characterization, it is important that the measured sonic log used is accurate and consistent. Due to anisotropic effects in the reservoir, which is majorly caused as a results of interbedded sequence of sand and shales, sonic log (compressional and shear wave velocities) acquired in vertical wells are different from those acquired in deviated wells. Rock physics models are created for anisotropic heterogeneous sand-shale sequence. These models are varied as a function of angle, porosity, saturation and net to gross. Variation of Thomsen anisotropic parameters and anelliptic parameters as a function of saturation and net-to-gross are investigated in order to understand the significant of anisotropy on these properties. From the rock physics modelling, anisotropic effect becomes more pronounced at high propagation angle and also the variation of the geologic parameters strongly depends on the propagation angle. Anisotropy effects decreases with increasing net-to-gross and anelliptic parameters are more sensitive to fluid saturation compared to Thomsen anisotropy parameters.

A method is proposed for anisotropy correction of deviated wells using core measurement (model rock properties) of sand and shale from the study area, the inclination angle of the well and the net to gross ratio of the reservoir. The anisotropy corrected logs are then used for improved rock physics interpretation using the rock physics templates(RPT) and AVO analysis. The proposed correction is lithology dependent and the correction is significant in regions with low net-to-gross. Discrimination of lithologies and fluid saturation on the rock physics template is enhanced as a result of the anisotropy correction.

The rock physics templates are constructed for different net to gross and propagation angles for varying fluid saturation in order to account for anisotropic effects. There is better separation of water sands and gas sand on the horizontal RPT(created at 72°) compared to vertical RPT(created at 0°). Vertical well, deviated well and anisotropy corrected well log data from the North Sea are superimposed on the rock-physics templates. Poor separation of lithology and saturation is observed on the RPT using the deviated well. It can be observed that the anisotropy corrected deviated well follows similar trends as the vertical well. Anisotropy effect on the reservoir properties that are accounted for using the proposed method are clearly seen on 3D rock physics templates. AVO inversion is also performed on the horizon attribute data from study area. The inverted rock physics properties are plotted on the created rock physics models for two vertical wells from the study area. The two vertical wells show different AVO class response. The net-to-gross and porosity are different for the two wells and in general, these observations are constrained by local geology.

Table of Contents

List of Figures

List of Tables

Chapter 1

Introduction

Petroleum reservoirs vary in internal structure and constituents. These heterogeneities occur at a much smaller scale compared to seismic wavelength (Ikelle and Amundsen, 2005). If sonic wells are penetrated through this anisotropic formation, the sonic velocities measured in vertical wells will be different compared to corresponding velocities acquired from deviated wells within the same vertical depth limit. The presence of seismic anisotropy causes the velocities to vary with angle of deviation. To capture the information about the internal structure and gain more important geophysical information as well as to account for these anisotropic effects, it is important to consider the reservoir as an effective anisotropic medium.

1.1 Objectives

The goal of this master thesis is to account for the effect of seismic anisotropy in rock physics interpretation using rock physics template and better understand its impact on amplitude variation with offset (AVO) modelling using the AVO cross-plot. Rock physics template is an important tool for lithology and fluid prediction, which is created using the combination of depositional and diagenetic trend models with Gassmann fluid substitution(Avseth et al., 2005). And AVO cross-plot is simply cross-plotting AVO attributes such as intercept and gradient. I create a more accurate model from seismic anisotropy and use it in rock physics interpretation of both vertical and deviated well log data from the North Sea and AVO analysis of seismic data from the same location. A methodology and its workflow will be presented to correct for anisotropic effects on deviated wells using core measurement (model rock properties) of sand and shale from the study area, the inclination angle of the well and the net to gross ratio of the reservoir. The preciseness of the method is examined by comparing the corrected deviated well with the available vertical well. Transverse isotropic models are assumed for the reservoir and the Thomsen (1986) anisotropy parameters and Tsvankin and Thomsen (1994) anelliptic parameters are employed to characterize the magnitude of the anisotropy. The vertical well is used to relate the Thomsen parameters to the vertical velocities and the result provide a basis for the magnitude of the seismic anisotropy. Rock physics templates are created

following the suggested workflows presented by Avseth et al. (2010). The templates are created for different fluid saturation at varying net to gross and angles. The templates are then superimposed on the study well data and the various effects are investigated.

1.2 Thesis Structure

This thesis consists of six chapters including this introductory chapter and the appendix. The chapters follow a systematic order in which the tasks are carried out. This thesis is organized as follows:
In chapter 2, the background theory of seismic anisotropy, Gassmann fluid substitution, Backus averaging, rock physics interpretation with focus on rock physics template (RPT) and AVO modelling are discussed. Also this chapter details the modelling carried out in this work and the workflows are demonstrated. The computational results of the modelling are also shown in this chapter.
Chapter 3 describes the methods used in achieving the results that will be presented in Chapter 4. A proposed method for accounting for the effect of anisotopy is also explained in this chapter and the workflows for creating the rock physics template are presented in this chapter. The methods for performing AVO inversion for rock physics attributes are also discussed in this chapter.
Chapter 4 begins with the description of the available data and the remainder of the chapter focuses on the analysis of the data and presentation of the results from the analysis.
Chapter 5 focuses on the interpretation of results. The results from the comparison of the vertical well, deviated well and the anisotropy corrected deviated well are discussed. The preciseness of the proposed method is also discussed. The summary and conclusion are detailed in the last chapter, chapter 6.

Chapter 2

Background theory

2.1 Seismic Anisotropy

In general sense, when a material is measured at the same location and its properties are directionally dependent, such material is said to be anisotropic. Anisotropy as a concept in geophysics originated when a heterogeneous material is treated as homogeneous on a scale of the wavelengths used to probe them (Winterstein, 1990). In order to adequately identify a material as anisotropic in geophysics, it is important to consider the scale in relation to the probing wavelength. Thomsen et al. (2002) simply defined seismic anisotropy as the dependence of seismic velocity on direction. And by seismic velocity, he did not only implies P- and S-wave velocities but also various forms of velocities such as group and phase velocities, which are discussed later in this work. The main types (or causes) of anisotropy can basically be classified into lithological (or intrinsic) anisotropy or stress-induced (extrinsic) anisotropy. Lithological (or intrinsic) anisotropy results from the rock texture and it can be caused by the bedding or lamination at larger scales and the preferential arrangement of sediment grains and pores. While stress-induced (extrinsic) anisotropy is caused by the resulting strain from fracturing and stress (Wang, 2001).

In the previous project work carried out, the reservoir subsurface was assumed to be isotropic heterogeneous medium. Isotropic heterogeneous medium has the seismic properties of the reservoir varying from one point (particle) to another and for a particular point, these seismic properties are independent of the propagating direction. And anisotropic medium has its seismic properties of the reservoir at any particular point to be directionally dependent.

2.1.1 Seismic Anisotropic Symmetry

Symmetry is the variation in the direction in which a material is arranged together and for any medium or material, there are different numbers of way it can be arranged (Winterstein, 1990). The arrangement of the various physical constituents in a medium consequently results in its symmetry properties. Symmetry is a function of the elastic constants in the sense that decrease in the elas-

tic constants leads to increase in symmetry. Unlike isotropic medium, in which only two moduli are independent, an anisotropic elastic medium can have as much as 21 elastic constants that are independent (Anderson, 1989).

This results from the fact that stress and strain in a medium can each be resolved into six components, which are basically three compressional and three shear stress and strain and based on Hooke's law, each stress or strain component can be expressed as a linear combination of the strain or stress components as shown in equation 2.1 (Anderson, 1989).

$$\sigma_{ij} = c_{ijkl}\varepsilon_{kl}, \tag{2.1}$$

where σ_{ij} is the stress tensor, ε_{kl} is the stress tensor and c_{ijkl} is the tensorial stiffness.

Considering that there are three independent spatial directions i.e x, y and z which correspond to 1,2 and 3 in a Cartesian coordinate system, i, j, k and l may take three different values individually. Thus the 4^{th} order tensor has $3^4(81)$ components of which only 21 elements are independent since i, j, k and l can be interchanged as in equation 2.2

$$c_{ijkl} = c_{jikl} = c_{ijlk} = c_{klij}. \tag{2.2}$$

Using the well known Voigt notation, the 21 independent components, which is the most general anisotropic model (triclinic symmetry) can be rewritten by denoting c_{ijkl} with C_{IJ} where $ij \rightarrow I$ and $kl \rightarrow J$ with I and J from 1 to 6, conforming to $11, 22, 33, 23, 31, 12 \leftrightarrow 1, 2, 3, 4, 5, 6$ respectively. This can be represented by a symmetrical 6x6 matrix as shown in equation 2.3:

$$C = \begin{bmatrix} C_{11} & C_{12} & C_{13} & C_{14} & C_{15} & C_{16} \\ C_{12} & C_{22} & C_{23} & C_{24} & C_{25} & C_{26} \\ C_{13} & C_{23} & C_{33} & C_{34} & C_{35} & C_{36} \\ C_{14} & C_{24} & C_{34} & C_{44} & C_{45} & C_{46} \\ C_{15} & C_{25} & C_{35} & C_{45} & C_{55} & C_{56} \\ C_{16} & C_{26} & C_{36} & C_{46} & C_{65} & C_{66} \end{bmatrix} \tag{2.3}$$

Based on the relative orientation of the symmetry planes, anisotropic symmetry systems are grouped int eight different symmetry systems and the common systems are shown in figure 2.1 (Crampin, 1984). The simplest realistic symmetry in the anisotropic case is the hexagonal symmetry which

has 5 independent elastic constants and it is classified into based on the symmetry axis. A hexagonal symmetry medium with vertical symmetry axis is termed transversely isotopic medium while that with a horizontal symmetry axis is called azimuthally anisotropic medium. Most sedimentary rocks especially horizontally layered formation exhibit anisotropy that is peculiar to transversely isotopic(TI) symmetry. This type of anisotropy is also referred to as polar anisotropy with five independent anisotropic moduli(Thomsen et al., 2002).

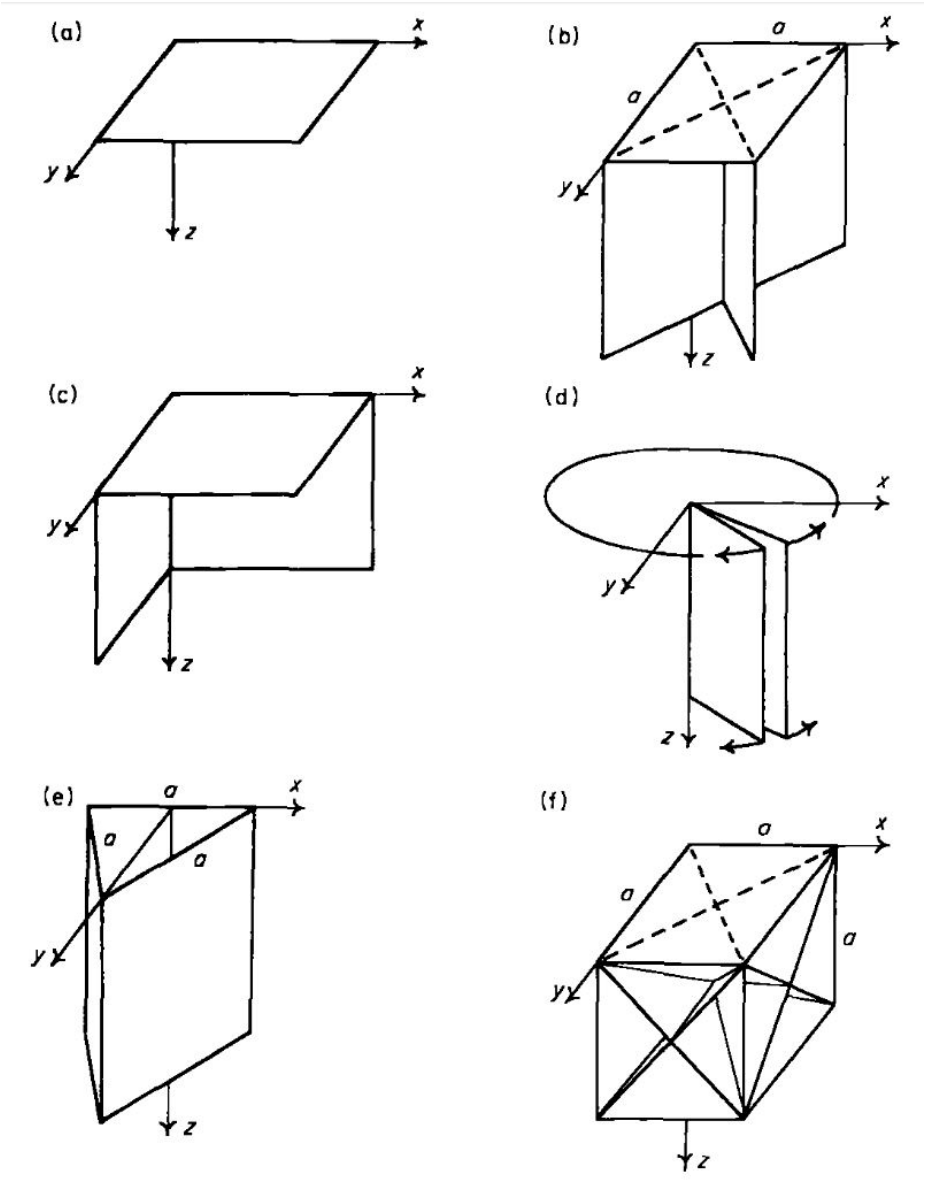

Figure 2.1: Arrangement of symmetry planes of the common symmetry systems: (a) monoclinic; (b) tetragonal; (c) orthorhombic; (d) hexagonal; (e) trigonal; and (f) cubic.(Crampin, 1984)

.

2.1.2 Anisotropy Parameters

Thomsen (1986) proposed notations that give better understanding of the influences of anisotropy and thus quantify its effect. So instead of using the stiffness coefficients in describing the impact of anisotropy on a VTI media, we can as well use the simplified parameters by Thomsen (1986). These parameters will be zero for isotropic media. And which obviously means that the higher the values of these parameters, the stronger the anisotropy. Equations 2.4 to 2.8 show the V_P and V_{SV} vertical velocities and the three anisotropic parameters.

$$V_P = \sqrt{\frac{C_{33}}{\rho}}, \tag{2.4}$$

$$V_{SV} = \sqrt{\frac{C_{44}}{\rho}}, \tag{2.5}$$

$$\gamma = \frac{C_{66} - C_{44}}{2C_{44}}, \tag{2.6}$$

$$\delta = \frac{(C_{66} - C_{44})^2 - (C_{66} - C_{44})^2}{2C_{44}(C_{33} - C_{44})}, \tag{2.7}$$

$$\varepsilon = \frac{C_{11} - C_{33}}{2C_{33}}, \tag{2.8}$$

where V_P and V_{SV} are the vertical P-wave velocity and S-wave velocity respectively, ρ is the density and C_{ij} are the independent elastic constants. γ, δ and ε are the dimensionless anisotropy parameters.

qP- and qSV-wave velocities depend on the parameters V_P, V_{SV}, ε, and δ, while the qSH-wave is controlled by V_{SV}, and γ (Ikelle and Amundsen, 2005).

Tsvankin and Thomsen (1994) introduces the parameters σ and η given in equation 2.9 and 2.10, which are important notations that reduce the requirement of the more intuitive Thomsen anisotropy parameters. For elliptical anisotropy, σ is equal to zero. SV-wave velocities and moveout equations are influenced by this parameter.

$$\sigma = (\varepsilon - \delta)\left(\frac{V_{P0}}{V_{s0}}\right)^2, \tag{2.9}$$

$$\eta = \frac{\varepsilon - \delta}{1 + 2\delta}, \tag{2.10}$$

In weak anisotropy approximation case i.e a case in which the absolute value of the anisotropy parameters are far less than one (1), the phase velocity and group velocity (which will be discussed later in this chapter) are assumed to be the same. So if,

$$|\gamma|,\ |\delta|,\ |\varepsilon| \ \ll\ 1,\ V_{Ph} = V_{Gr}, \tag{2.11}$$

where V_{Ph} and V_{Gr} are the phase and group velocity respectively.

2.1.3 Seismic Anisotropic Velocity

Contrary to isotropic elastic media, which have two types of elastic waves namely the compressional and shear wave, anisotropic media waves are not entirely longitudinal or transverse, except in certain directions. The particle motion has components both parrallel and perpendicular to the direction of propagation (Anderson, 1989). And the S-wave velocity is affected by both the propagating direction and polarization. As a result of different polarization of s-wave, a phenomenon called shear wave splitting (birefringence) occurs and this leads to two shear waves with different speeds of propagation. These waves are called quasi-P (qP), quasi-longitudinal (qSH) or quasi-transverse (qSV) waves since the wave polarizations are not strictly parallel or perpendicular to the propagating direction (Winterstein, 1990).

2.1.4 Phase and Group Velocity

Wave propagations are in different manner in isotropic and anisotropic media. In isotropic media, the wavefront is spherical and therefore the velocities (group and phase velocity) are the same at all angles and directions. However, anisotropic media are dispersive i.e velocity is dependence on the propagating direction (Ikelle and Amundsen, 2005). As a result of this directional dependence, the wavefront is not spherical and consequently, the seismic velocity in anisotropy results in phase and group velocity that are generally different (Winterstein, 1990).

According to Winterstein (1990), phase velocity is defined as the speed at which a point of constant wavelet phase travels in a direction normal to the wave surface in a homogeneous medium and the speed of a plane wave traveling in the same direction in such a medium. Phase velocity is affected

by angular dispersion. While group velocity is the speed at which wave surface and wave energy travel in a given direction radially outward from a point source in a homogeneous medium and it varies with direction in anisotropic media.

Figure 2.2 gives an illustrative explanation to phase and group velocity. The figure shows wavefronts propagating away from a point source. The medium within the wavefront is assumed to be homogeneous VTI medium. The group velocity is represented by the dashed line and it travels in the source-receiver direction. And the phase velocity is represented by the straight line and it travels in an orthogonal direction to the wavefront.

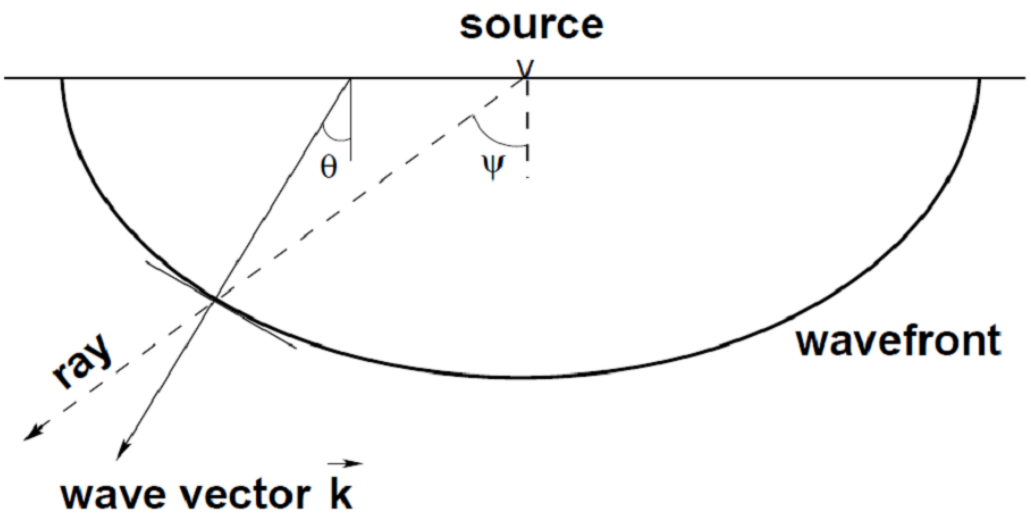

Figure 2.2: Phase and group velocity (Thomsen, 1986)

.

Phase velocities for qP-, qSV-, and SH-waves for a medium with transversely isotropic(hexagonal) symmetry can be expressed as a function of elastic moduli (Thomsen (1986); Banik (1984); Ikelle and Amundsen (2005)) using the solution of Christoffel equation given by equation2.12 below:

$$\left[C_{ijkl}n_j n_i - \rho v^2 \delta_{ik}\right]\left[u_k^o\right] = 0, \tag{2.12}$$

where δ_{ik} is the Kronecker delta (which is 1 when i = k and 0 where i $\neq$ k).

Two solutions as shown in equation 2.13 can be derived from equation 2.12 for an isotropic case:

$$V_P = \sqrt{\frac{\lambda + 2\mu}{\rho}} \quad and \quad V_S = \sqrt{\frac{\mu}{\rho}}, \tag{2.13}$$

where V_P is the P-wave velocity and V_S is the S-wave velocity.

For a VTI media, there are three solutions given by equation 2.14 and 2.15.

$$2\rho V_{SH}^2(\theta) = C_{66}\sin^2\theta + C_{44}\cos^2\theta, \tag{2.14}$$

$$2\rho V_{P,SV}^2(\theta) = (C_{11} + C_{44})\sin^2\theta + (C_{33} + C_{44})\cos^2\theta \pm \sqrt{D}, \tag{2.15}$$

where $D = \left[(C_{11} - C_{44})\sin^2\theta - (C_{33} + C_{44})\cos^2\theta\right]^2 + 4(C_{33} + C_{44})\sin^2\theta\cos^2\theta$,

and V_P and V_{SV} is the P-wave velocity corresponding to + solution and SV-wave velocity corresponding to - solution respectively in equation 2.15, and V_{SH} is the SV-wave velocity.

Contrary to phase velocity that can be estimated directly from the Christoffel equation, group velocity are obtained by differentiating frequency with respect to wave vector (Winterstein, 1990).

2.1.5 Application of seismic anisotropy

Seismic anisotropy has been gaining increasing application in the petroleum industry as a result of the additional information of the subsurface that can be obtained. Thereby significantly reducing the risk involved in exploration and decision making. Of its numerous applications in the industry, focus will be on its application for the correction of deviated wells, moveout velocities, amplitude versus offset (AVO) and prestack migration.

Seismic properties from deviated well data can be corrected using seismic anisotropy. In most cases, the measured seismic velocity in a deviated well is higher than that of a vertical well at a given depth. The anisotropy parameters of the rocks close to the well are the major reasons for this difference in the propagation velocity. Previous works by Hornby et al. (2003), Wild et al. (2011) considered anisotropy correction for deviated wells by creating an inversion scheme to estimate the anisotropy-corrected vertical well logs recorded in a deviated well and used the corrected log for a more accurate well tie. The non-hyperbolic moveout behavior of reflections from horizontal interfaces is an important source of velocity information for processing, especially in anisotropic media. In most anisotropic media, the nonhyperbolic moveout is relatively large, larger, in fact, than that in typical vertically heterogeneous isotropic media. Therefore, it usually is observable and measurable and thus can be used to invert for medium parameters (Alkhalifah, 1997). This can however by achieved by considering the anisotropy parameters. Alkhalifah and Tsvankin (1995)

carried out velocity analysis for transversely isotropic (TI) media by inverting the dependence of P-wave moveout velocities on the ray parameter and tested the method on synthetic and real data, which consequently provided reasonable information to perform all major time-processing steps, including dip moveout and prestack and poststack time migration. Anisotropy is also important in amplitude versus offset (AVO) modelling. For anisotropic media such as horizontal transverse isotropy (HTI), the seismic velocities vary at different angles (or azimuths) and consequently the reflection coefficients of a propagating incident P-wave on the boundary of such media will also be different at any arbitrary angle. So considering amplitudes of a reflected wave at various angles, one may obtain more information about the strength of anisotropy of such reservoirs. Rüger (1998, 2001) and Thomsen et al. (2002) derived and showed various approximate equations of the reflection coefficient of incident P-wave at an arbitrary angle in a case where the upper and lower layer are both horizontal transverse isotropy (HTI) media.

Prestack depth migration is important and carried out in areas with intense geological activities. Therefore adequate information are required in order to carry out migration of all traces before it is moved to zero offset. By applying P-wave anisotropic prestack depth migration, a more consistent and accurate seismic image of the subsurface can be obtained in depth and space, hereby enhancing the characterization of reservoir. Harris et al. (2002) applies anisotropy parametrization in depth migration in order to improve the accuracy of the lateral positioning of the target overlied by anisotropic sediments.

2.2 Gassmann Fluid Substitution

The Gassmann (1951) equation is the most frequently used tool for fluid substitution and it is applied to predict the changes in rock modulus or stiffness with variation of the pore fluid contents using the frame properties. It estimates the stiffness coefficients of an isotropic fluid saturated porous media as shown in equation 2.16 to 2.17 using the known bulk moduli of the rock matrix, the frame (skeleton rock sample), and the pore fluid, which can be water, oil, gas or combination of any of the three (Wang, 2001).

$$C_{33} = K_{fr} + \frac{4}{3}\mu + \frac{(K_{fr} - K_{ma})^2}{K_{ma}(1 - \phi + \phi\frac{K_{ma}}{K_f} + \frac{K_{fr}}{K_{ma}})}, \tag{2.16}$$

where K_{fr} is the bulk modulus of the frame, K_f is the bulk modulus of the fluid, K_{ma} is the rock

matrix bulk modulus and ϕ is the porosity. Since fluid saturation has no effect on the shear modulus of the rock, therefore

$$C_{44} = \mu, \tag{2.17}$$

where μ is the frame shear modulus of the rock. The bulk modulus K_f can be computed for a fluid mixture using the fluid mixing law of Wood (Wood, 1941):

$$\frac{1}{K_f} = \frac{S_w}{K_w} + \frac{S_o}{K_o} + \frac{S_g}{K_g}, \tag{2.18}$$

where K_w, K_w, K_o and K_g are the bulk moduli of water, oil, and gas respectively. S_w, S_w and S_w are the water, oil, and gas saturations, respectively, which are expressed as the volume fractions of the pore space (i.e the sum of these saturations must be equal to one) and this equation is based on the assumption that the fluid is uniformly distributed in the pores. The density of the isotropic fluid saturated porous media is simply estimated using the equation below:

$$\rho = \phi\rho_f + (1 - \phi)\rho_{ma}, \tag{2.19}$$

where ρ_{ma} is the rock matrix density and ρ_f is the bulk density of the fluid mixture given by

$$\rho_f = S_w\rho_w + S_o\rho_o + S_g\rho_g, \tag{2.20}$$

where ρ_w, ρ_o and ρ_g denotes water, oil, and gas densities respectively.

The fundamental assumptions as explained by Wang (2001) for the application of gassmann equation are firstly the rock (both the matrix and the frame) is macroscopically homogeneous. Secondly all the pores are interconnected and are filled with a frictionless fluid (liquid, gas, or mixture). Thirdly, the rock-fluid system under study is closed (undrained). And lastly the pore fluid does not interact with the solid in a way that would soften or harden the frame.

2.3 Backus Averaging

Backus averaging method (Backus, 1962) is an important upscaling approach for the estimation of the effective elastic constant for a stack of isotropic or anisotropic thin layers. This upscaling approach approximates a stack of thin intercalating layers of two or more isotropic media as one effective anisotropic medium and elastic properties is averaged at a particular wavelength or frequency

as shown in figure 2.3. Consequently, the resulting effective elastic constants of the homogeneous volume are equivalent to that of the heterogeneous sequence. This method assumes that the stack of layers is smaller than the propagating seismic wavelength.

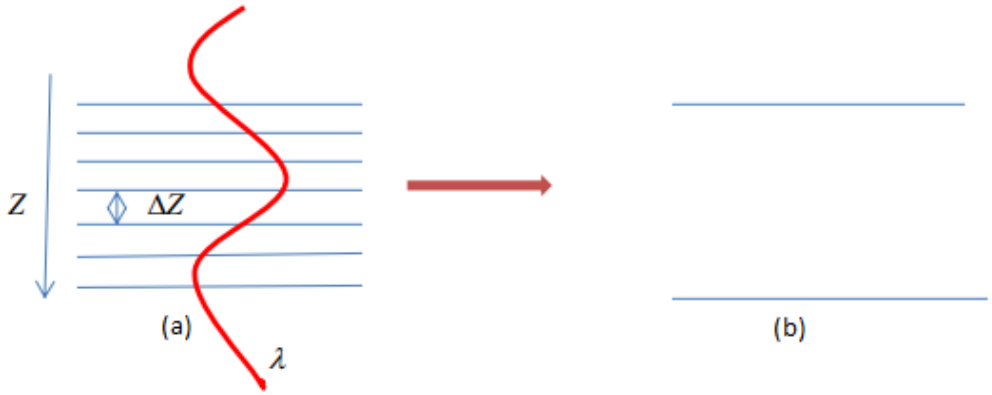

Figure 2.3: Backus averaging from a horizontally layered inhomogeneous medium(a) to an effectively homogeneous medium(b) ensuring that $\lambda >> \triangle z$. Where λ is the wavelength and $\triangle z$ is the layer thickness.

The backus averaging equations (Backus, 1962) for computing the effective stiffness coefficients and density for a stack of anisotropic thin layers are shown in equation 2.21 and 2.22 respectively.

$$\begin{aligned}
\widetilde{C_{33}} &= \langle C_{33}^{-1} \rangle^{-1}, \\
\widetilde{C_{44}} &= \langle C_{44}^{-1} \rangle^{-1}, \\
\widetilde{C_{13}} &= \langle C_{33}^{-1} \rangle^{-1} \langle C_{13}.C_{33}^{-1} \rangle, \\
\widetilde{C_{11}} &= \langle C_{11} - C_{13}^{2}.C_{33}^{-1} \rangle + \langle C_{33}^{-1} \rangle^{-1} \langle C_{13}.C_{33}^{-1} \rangle^{2}, \\
\widetilde{C_{66}} &= \langle C_{66} \rangle,
\end{aligned} \tag{2.21}$$

$$\widetilde{\rho} = \langle \rho \rangle, \tag{2.22}$$

where $\widetilde{C_{ij}}$ and $\widetilde{\rho}$ are the stiffness coefficients and bulk density for the effective media respectively. C_{ij} and ρ are coefficients of the stiffness tensor and bulk density of the individual local layer. Angle brackets represent averaging of local layer properties of sand and shale end members using the proportion of sand in the entire sequence (NG) and proportion of shale in the entire sequence (1-NG). NG is the Net-to-gross, which is an important parameter to determine the degree of heterogeneity of sands. It is the measure of the fraction of pay sand in the overall reservoir(i.e. reservoir sands and interbedded shales) and anisotropy intrinsically depend on this. Net-to-gross(N/G) ranges from 0 to 1. N/G of zero (0) being a shale package and N/G of 1 corresponding to pure isotropic sand.

When upscaling sequence of alternating lithologies to an effective medium, it is important to predict the net-to-gross (Avseth et al., 2010). Various works (Vernik et al. (2002), Stovas et al. (2006), Connolly and Kemper (2007)) have been published, which predict the net-to-gross using different approaches.

In this work, the net-to-gross is predicted from the shale volume (V_{sh}) curve, which is calibrated from the gamma-ray log. The shale volume (V_{sh}) is estimated by linearly interpolating between the clean sand(minimum) and impermeable shale(maximum) gamma-ray log responses as shown in equation 2.23.

$$V_{sh} = \frac{GR_l - GR_{min}}{GR_{max} - GR_{min}}, \tag{2.23}$$

where GR_l is the gamma-ray log value of the depth of interest. The net-to-gross is estimated as $NG = 1 - V_{sh}$ implying that NG of 1 corresponds to 0% shale volume. The major limitation of these approach is that the shale volume estimated is the laminar shale volume and it is not accounting for the dry volume of the clay minerals in the bedding. So the estimated values of NG is a rough estimate since it is not an accurate representation of the reservoir heterogeneity.

2.4 Rock Physics Templates

Rock physics templates (RPT) were proposed by Ødegaard and Avseth (2003) based on theory by Dvorkin and Nur (1996), as a tool, in which the fluid and lithology of a reservoir could be predicted on a crossplot of V_P/V_S versus acoustic impedance. RPT assess the relation between rock physics properties and local geologic paraters such as mineralogy, porosity, fluid type, pressure and grain contacts. There are basically four procedures involved in constructing RPT (Ødegaard and Avseth, 2003), which are:

1. Estimation of the moduli of the dry rock frame for a given porosity/pressure using the Hertz-Mindlin theory(Mindlin, 1949).

2. Estimation of the moduli of the dry rock frame over a range of porosities using the lower Hashin-Shtrikman bound(Hashin and Shtrikman, 1963).

3. Perform fluid substitution with the Gassmann equations(Gassmann, 1951).

4. Calculationn of the density, P-wave velocity, S-wave velocity for each case and cross-plotting V_P/V_S against acoustic impedance.

The initial dry rock values can be computed using using Hertz-Mindlin contact theory, the Gregory-Pickett method (the lower Hashin-Shtrikman bound) or Dvorkin and Nur's cemented sand model(Ødegaard and Avseth, 2003). Rock physics template (RPT) is illustrated in figure 2.4 which is presented as cross-plots of VP/VS versus AI. The template includes porosity trends for different lithologies, and increasing gas saturation for sands (assuming uniform saturation), background shale trend, a brine-sand trend and an increasing gas saturation as a function of sand porosity curve. The black arrows show various geologic trends (conceptually): (1) increasing shaliness, (2) increasing cement volume, (3) increasing porosity, (4) decreasing effective pressure, and (5) increasing gas saturation. (Avseth et al., 2005).

It is important to note that RPT interpretation of well log data may also be a stand-alone tool for quality control of well log data and for interpretation of the data for the determination of the type of lithology and the fluid content. In this work, rock physics template is plotted for varying geologic parameters such as net-to-gross, deviation angle and so and some trends in fluid and lithology are investigated, which are discussed in chapter five.

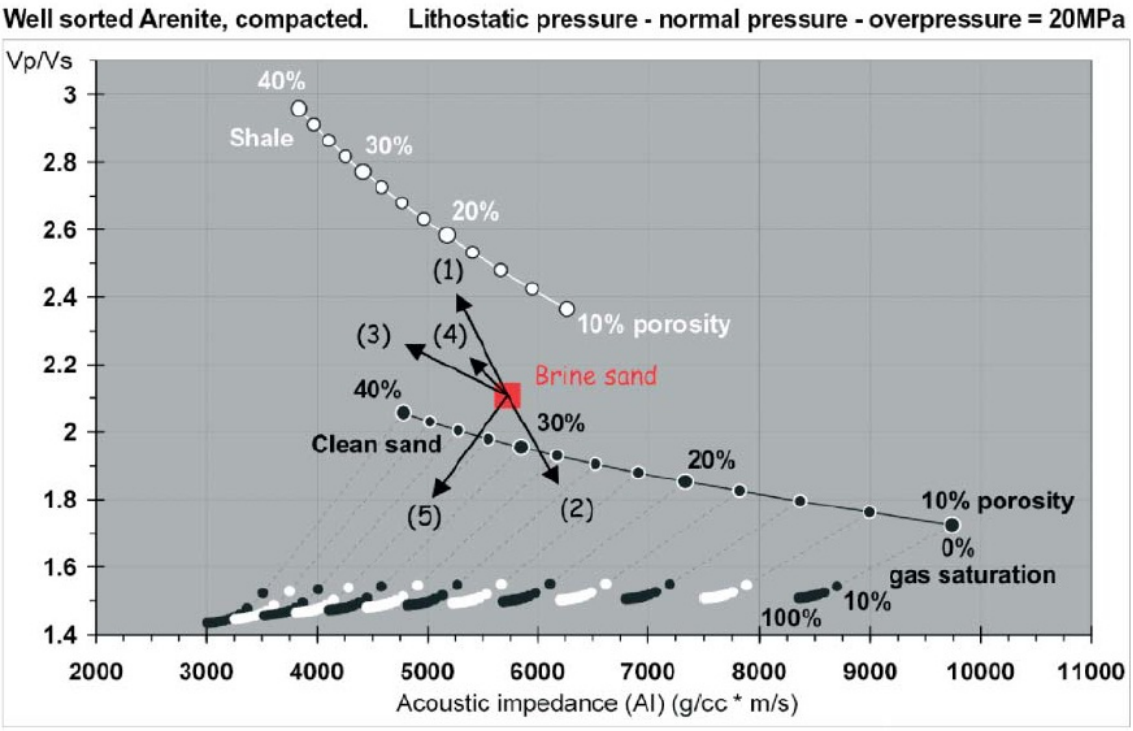

Figure 2.4: A typical illustration of rock physics template (RPT) as cross-plots of V_P/V_S versus Acoustic impedance. The lines are constant cement lines of 2% with different fluid saturation. The sand lines are computed at 70° Celsius and 20MPa pressure and the shale line is computed at 50° Celsius and 18 MPa pressure (Avseth et al., 2005)

.

2.5 Amplitudes Variation with Offset (AVO)

Amplitude variation with offset refers to the dependency of the seismic attribute and amplitude with the distance between the source and receiver (the offset). In recent time, it has become an important tool for hydrocarbon prospecting to detect fluids. Before carrying out AVO analysis, it is important to find out if it is the appropriate tool to be used. It will work only if the rock physics and fluid characteristics of the target reservoir are expected to give a good AVO response (Avseth et al., 2005).

Various AVO attributes such as reflection coefficient intercept at normal incidence, the reflection-coefficient gradient at normal incidence, P-wave and S-wave normal-incidence reflectivity are available for AVO analysis. These attributes are derived from various approximation(Foster et al., 2010). Interpretation of AVO anomalies is facilitated by crossplotting these attributes. AVO intercept and gradient for brine-saturated sandstones and shales follow a well-defined "background" trend for various geologic conditions . AVO anomalies" are properly viewed as deviations from this background and may be related to hydrocarbons or lithologic factors(Castagna and Swan, 1997). Figure 2.5 shows a simple cross plot of Intercept versus slope and deviation from the background (fluid) trend.

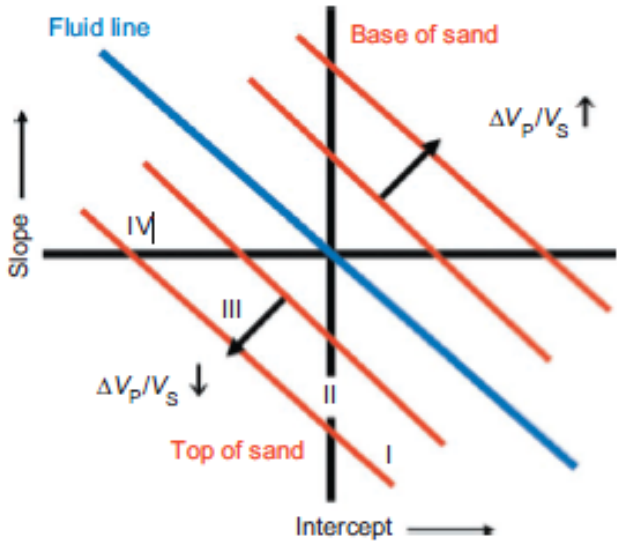

Figure 2.5: Intercept versus gradient crossplot indicating background trend and deviation from this background.(Foster et al., 2010)

.

2.5.1 AVO for isotropic media

Shuey (1985) shows that the P-wave reflection coefficient $R(\theta)$ for the isotropic media from the Aki and Richards (1980) approximation for weak layer contrasts can be further approximated by an equation of the form given by equation 2.24 to 2.27:

$$R(\theta) = R(0) + Gsin^2\theta + F(tan^2\theta - sin^2\theta), \tag{2.24}$$

where

$$R(0) = \frac{1}{2}(\frac{\Delta V_P}{V_P} + \frac{\Delta\rho}{\rho}), \tag{2.25}$$

$$G = \frac{1}{2}\frac{\Delta V_P}{V_P} - 2\frac{V_S^2}{V_P^2}(\frac{\Delta\rho}{\rho} + 2\frac{\Delta V_S}{V_S}), \tag{2.26}$$

and

$$F = \frac{1}{2}(\frac{\Delta V_P}{V_P}), \tag{2.27}$$

where R(0) is the reflection coefficient at normal incidence and is controlled by the contrast in acoustic impedances. G, often referred to as the AVO gradient, describes the variation of reflection amplitudes at intermediate offsets and F is a far offset attribute, which can can ignored in AVO analysis for relatively small angles of incidence, usually less than 30°. θ is the angle of incidence, V_P, V_S, and ρ are the averages of the vertical P-wave velocity, vertical S-wave velocity, and density above and below the reflecting interface, respectively. ΔV_P, ΔV_S and $\Delta\rho$ are the differences in P-wave velocity, S-wave velocity,and density between these layers, respectively.

2.5.2 AVO for anisotropic media

For weak anisotropy media with small offsets, the AVO attributes can be expressed by introducing anisotropy parameters(Rüger, 1998). In this case, the AVO gradient, G and far offset attribute, F can be rewritten as shown in equation 2.28 to 2.29

$$G = \frac{1}{2}\frac{\Delta V_P}{V_P} - 2\frac{V_S^2}{V_P^2}(\frac{\Delta\rho}{\rho} + 2\frac{\Delta V_S}{V_S}) + \frac{1}{2}\Delta\delta, \tag{2.28}$$

and

$$F = \frac{1}{2}(\frac{\Delta V_P}{V_P}) + \frac{1}{2}\Delta\varepsilon, \tag{2.29}$$

where $\Delta\delta$ and $\Delta\varepsilon$ are the differences in anisotropy parameters between these layers, respectively.

2.5.3 AVO Cross-plot analysis

Crossplotting of AVO gradient versus intercept can be used for the interpretation of AVO attribute. Hydrocarbons can be classified based on this crossplot. Figure 2.6 shows the various classes and the descriptions are given in table 2.1.

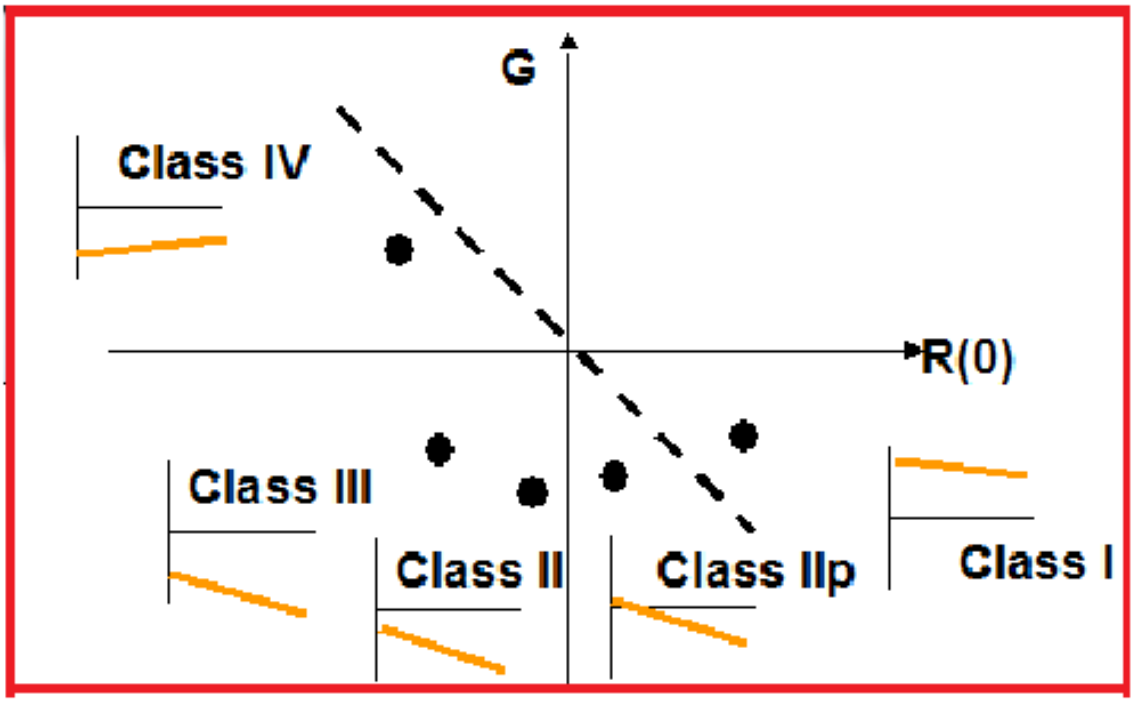

Figure 2.6: Intercept versus gradient crossplot illustrating the various classes of AVO signatures(Avseth et al., 2005)

.

Table 2.1: AVO classes(Avseth et al., 2005)

Class	Relative impedance	Quadrant	R(0)	G	AVO product
I	High impedance sand	4th	+	-	Negative
IIp	No or low contrast	4th	+	-	Negative
II		3rd	-	-	Positive
III	Low impedance	3rd	-	-	Positive
IV	Low impedance	2nd	-	+	Negative

2.6 Estimation of upscaled anisotropic parameters for effective model

Anisotropic heterogeneous interbedded sand-shale sequence is created by intercalating impermeable shale in clean sand units. The shale parameters used for these modellings are shown in table 2.2. The properties of this shale rock are assumed to be constant throughout the layers at any given depth. Then, I assume isotropic, homogeneous sandstone with interconnected pores and saturated with gas, oil and/or water, so $C_{33} = C_{11}, C_{44} = C_{66}, C_{13} = C_{33} - 2C_{44}$ implying vertical velocities are the same with the horizontal velocities. This is purposely to estimate the stiffness coefficients and density for the sandstone. These assumptions are important in order to apply Gassmann's equation. Based on these assumptions and the sandstone information in table 2.2, I apply the Gassmann's equation given by equation 2.16 to 2.18 to compute the stiffness coefficients and equation 2.19 to compute the density for the isotropic sandstone.

By assuming the individual layer thickness is smaller compared to the wavelength, the isotropic sand is combined with the anisotropic shale to have a mixed lithology. Backus averaging given by equation 2.21 and 2.22 is then employed to compute the effective stiffness coefficients and density for the anisotropic sand-shale sequence. Certain uncertainties are introduced in the models, based on the assumption that sand and shale properties in thin layer where $1 > NG > 0$ are similar to those measured with NG=1 (clean sand) and with NG=1 (clean shale). Secondly the assumption that sand and shale average layer thicknesses are very small in order to satisfy the Backus averaging condition(Vernik, 2007).

Before, the estimation of the velocities of effective model, the anisotropic parameters discussed in section 2.1.2 are computed. This is to determine the magnitude of anisotropy on the VTI model. The values of the anisotropic parameters ($\varepsilon = 0.0744, \gamma = 0.1871, \delta = 0.0401$) obtained are smaller than one ($\ll 1$). Based on this, the anisotropy is said to be weak. In a situation where we have weak anisotropy approximation, the phase velocity and group velocity are assumed to be the same as shown in equation 2.11. Also, when the wellbore penetrating a VTI media is vertical (that is the deviation is 0°), the wave propagation is parallel to the symmetry axis and consequently the phase and group velocities coincide.

I then compute the quasi phase velocities and associated elastic stiffness vectors from the solution of Kelvin-Christoffel equations given by equation 2.14 and 2.15 for an arbitrary propagation direction

from the TI symmetry axis. Table 2.2 consists of the elastic constants and density of sandstone, shale rock and fluids used for the modelling and other geophysical processes carried out in this study(Golikov et al., 2013).

Table 2.2: Model Parameters(Golikov et al., 2013)

Shale parameters	Sandstone parameters	Fluid parameters
$C_{11} - 19.7GPa$	$K_{fr} - 5GPa$	$K_w - 2.7GPa$
$C_{33} - 14.7GPa$	$K_{ma} - 35GPa$	$K_o - 1GPa$
$C_{13} - 11.1GPa$	$\mu - 3.5GPa$	$K_g - 0.1GPa$
$C_{44} - 2.4GPa$	$\rho_{ma} - 2.65g/cm^3$	$\rho_w - 1.02g/cm^3$
$C_{66} - 4.7GPa$	$\phi - 0.35$	$\rho_o - 0.75g/cm^3$
$\rho - 2.3g/cm^3$	$\rho_{bulk} - 1.72g/cm^3$	$\rho_g - 0.2g/cm^3$

2.7 Estimation of anisotropic AVO gradient and intercept for effective model

AVO modelling is also performed on the effective model created in the section above. This effective model is assumed to be overlain by shale.

The vertical P-wave and S-wave velocities as well as density for the overlying shale are obtained from the shale parameters in table 2.2. These parameters and the computed vertical velocities and density for the effective model are used for the AVO analysis. The averages and differences of the parameters of these two layers are estimated and input into equation 2.25 and 2.28 to compute the AVO gradient and intercept respectively. The results from the modelling are presented in the next section.

2.8 Computational results of the modelling

The study formation is categorized as a slow formation, which has its propagating compressional wave velocity greater than the shear wave velocity. Since VTI medium is constant with respect to any rotation about the well azimuth, I therefore show the plot of the computed phase velocities

(qP-, qSV-, and SH-wave velocities) as a function of the well deviation angle in figure 2.7 and 2.8. Figure 2.9 shows the cross-plot of V_P/V_S versus acoustic impedance (AI) as a function of varying phase angle, water saturation, net-to-gross and porosity. Figure 2.9 shows the contour plots for the dependence of anisotropy parameters and anelliptic parameters on net-to-gross ratio and water saturation.

For the AVO modelling, figure 2.11 and figure 2.12 show the AVO crossplot of intercept, R(0) and gradient, G as a function of varying water saturation and net-to-gross. Figure 2.14 and 2.13 show the contour plots for the dependence of AVO intercept and gradient on net-to-gross ratio and water saturation respectively.

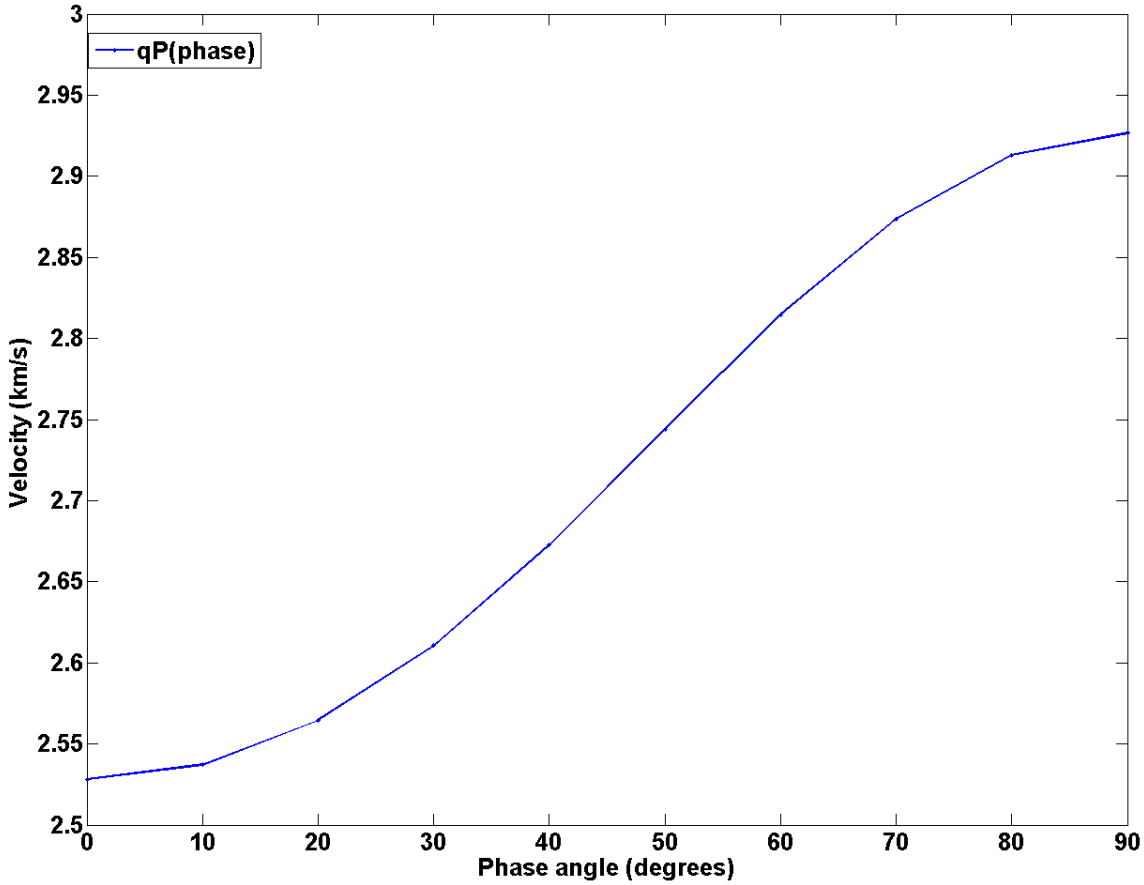

Figure 2.7: Estimated phase velocity for qP-wave as a function of propagation angle

.

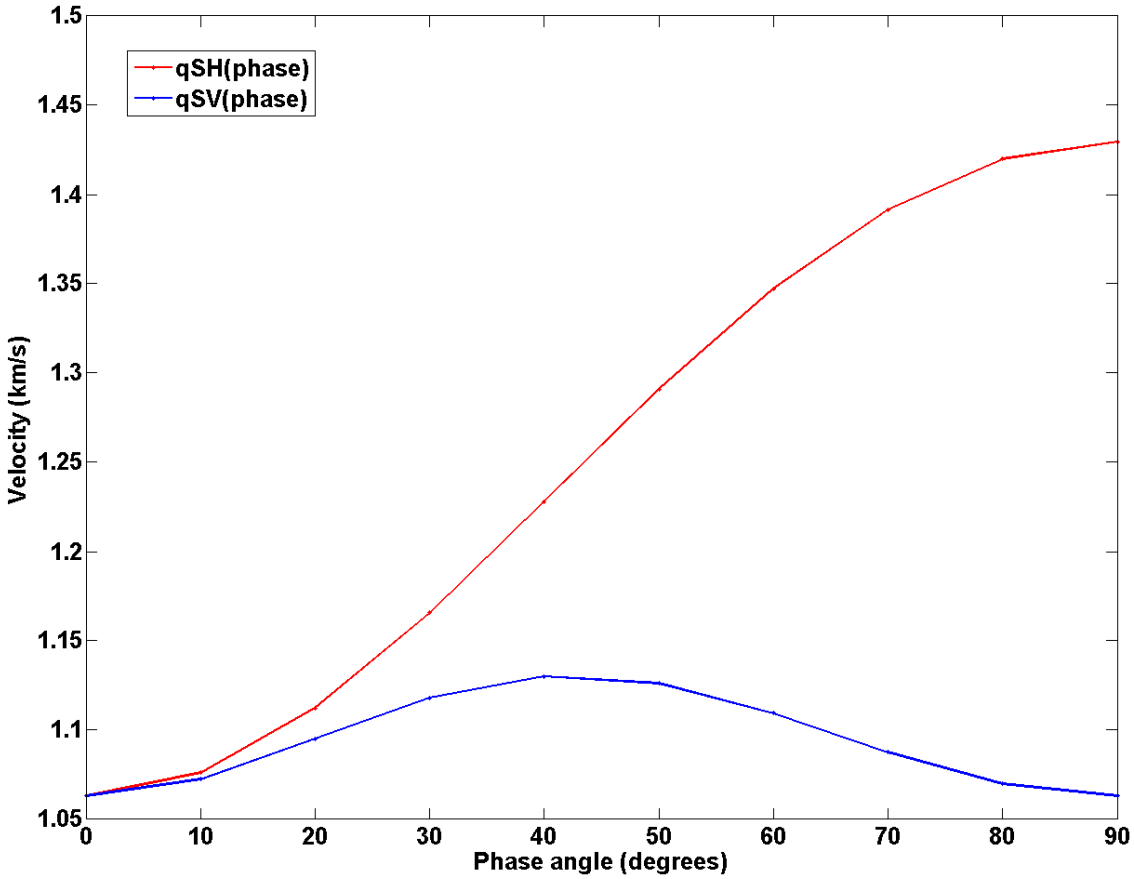

Figure 2.8: Estimated phase velocity for qSH- and qSV-wave as a function of propagation angle

.

Figure 2.7 illustrates the behavior of the estimated phase velocity for quasi-P (qP) wave as function of deviation angle from the VTI symmetry axis in the slow formation of the study area. As seen on the plot, the propagation speed for the quasi-P (qP) wave is slower for the vertical direction (i.e $0°$) as compared to the horizontal direction ($90°$). It can be noticed that there is small change (slight increase) in qP-wave phase velocity for small incident angle ($0°$-$30°$). The increase in velocity becomes more pronounced for large incident angles (>$30°$). The dependence of angle on phase velocity for quasi-P (qP) wave in the horizontal direction region is controlled by the Thomsen anisotropy parameter, ε and the transition from vertical to horizontal of the P-wave velocity is controlled by the anisotropy parameter, δ.

Figure 2.8 shows the behavior of the estimated phase velocities for qSH- and qSV-wave as function of deviation angle from the VTI symmetry axis in the slow formation of the study area. As seen on the plot, the propagation of phase velocity for qSH-wave shows similar behavior as that of the qP-wave. The only significant difference is the difference in the velocities range based on the fact that the VTI medium is a slow formation . The propagation of phase velocity for qSV-wave is complex

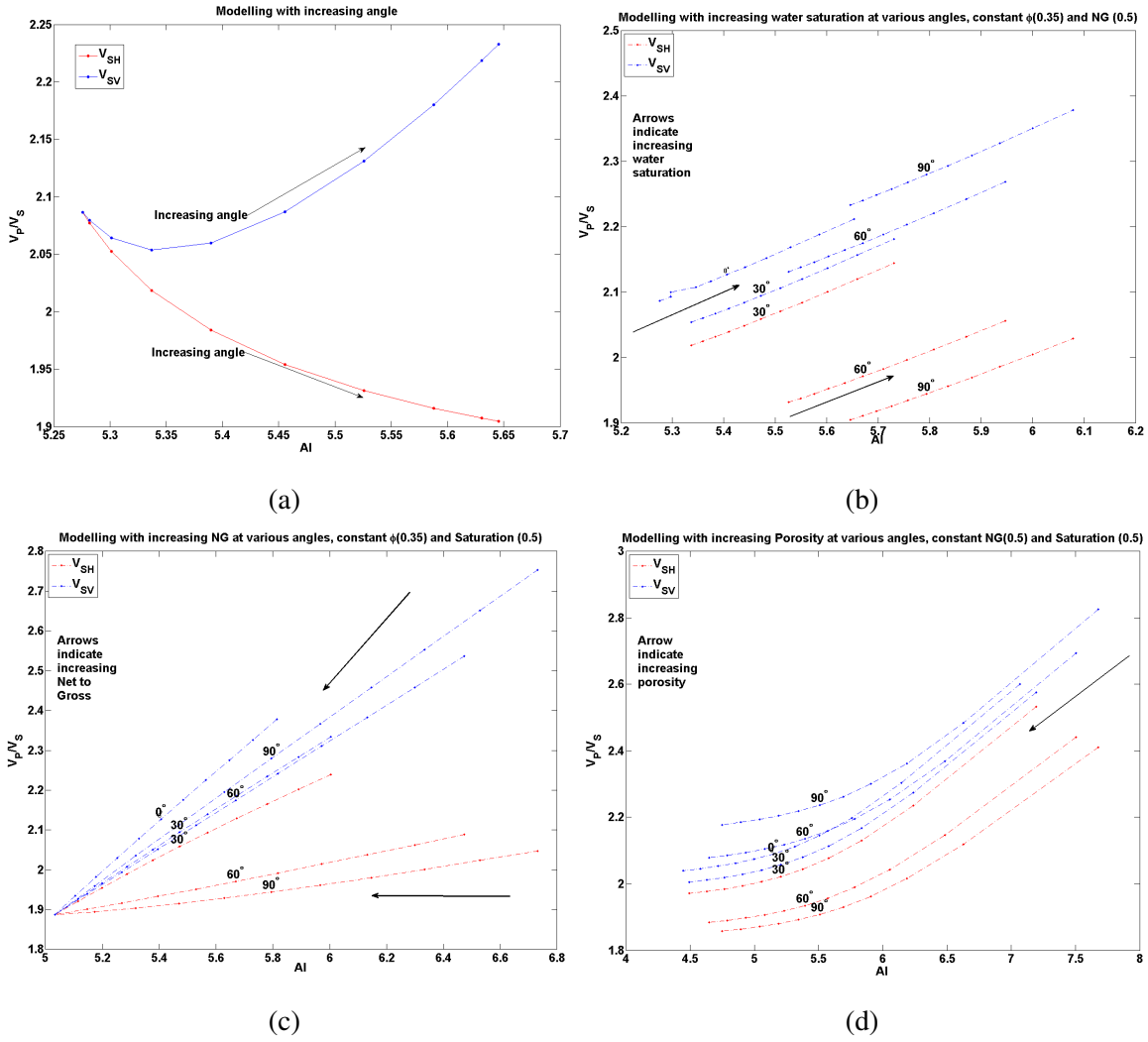

Figure 2.9: Cross-plot of V_P/V_S versus acoustic impedance as a function of varying parameters. a) Angle b) Saturation c) Net-to-gross d) Porosity.

than that of both qSH- and qP-wave. A convex region is observed in the mid-part of the deviation angle for qSV-wave phase velocity.

Figure 2.9a shows the cross-plot of V_P/V_S versus acoustic impedance for qSH- and qSV- wave velocities as function of varying angles. From the cross-plot, one observes that the qSV-wave velocity increases as a result of increasing angles. However, for qSH-wave velocity, which in its case decreases as a function of increasing angles. Figure 2.9b shows the cross-plot of V_P/V_S versus acoustic impedance for the results of increasing water saturation from 0 to 1 for various angles. The angles considered are $0°$, $30°$, $60°$ and $90°$. The arrows indicate the trends for increasing water saturation. This scenario is carried out for porosity of 0.35 and net-to-gross ratio of 0.5. Based on the plot, one observes that the acoustic impedance and the S-wave velocities (both qSV and qSH) increase with increase in the water saturation. It is quite important to mention that the trend for both

qSV- and qSH- wave velocities overlaps at 0° and this is because both velocities are equal at no inclination angle.

Figure 2.9c shows the cross-plot of V_P/V_S versus acoustic impedance for the results of increasing net-to-gross from 0 to 1(0 implies shale and 1 corresponds to the pure isotropic sandstone.) for various angles. The angles considered are 0°, 30°, 60° and 90°. The arrows indicate the trends for increasing net-to-gross. This scenario is carried out for water saturation of 0.5 and Porosity of 0.35. Based on the plot, one can see that the acoustic impedance and the S-wave velocities (both qSV and qSH) decrease with increase in the net-to-gross.

Figure 2.9d shows the cross-plot of V_P/V_S versus acoustic impedance for the results of increasing porosity from 0 to 1 for various angles. The angles considered are 0°, 30°, 60° and 90°. The arrow indicates the trends for increasing porosity. This scenario is carried out for water saturation of 0.5 and net-to-gross ratio of 0.5. Based on the plot, it is observed that the acoustic impedance and the S-wave velocities (both qSV and qSH) decrease with increase in the porosity.

Figure 2.10a shows the contour plot of the dependence of anisotropy parameter (ε) on net-to-gross ratio and water saturation. This scenario is carried out for constant porosity of 0.35. Based on the plot, it is observed that ε decreases with increasing net-to-gross ratio. This implies anisotropy effect decreases with increasing net-to-gross. However the sensitivity of ε to water saturation is low as shown on the plot. The dependence of anisotropy parameter (δ) on net-to-gross ratio and water saturation is shown in figure 2.10b and the porosity is kept constant. It can be seen that δ increases with decreasing net-to-gross and increasing water saturation.

Figure 2.10c and 2.10d show the contour plot of the dependence of anelliptic parameter (η) on net-to-gross ratio and water saturation. This scenario is carried out for constant porosity of 0.35. The trends show similiar pattern. Generally, there is better discrimination of saturation for the anelliptic parameters and the variation of net-to-gross is relatively the same for all scenarios.

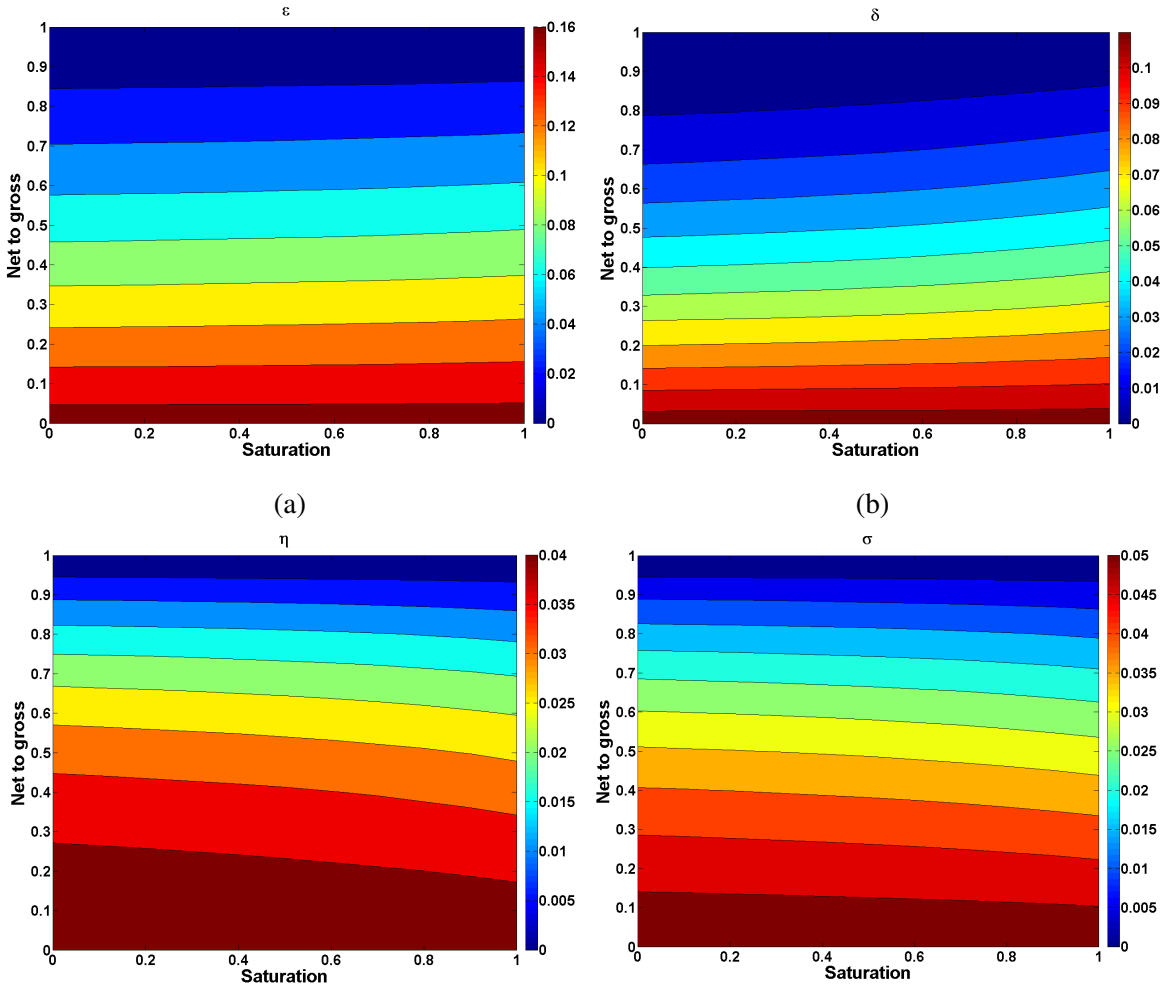

Figure 2.10: Contour plots showing the dependence of anisotropy parameters, ε, δ, η and σ on net-to-gross ratio and water saturation. The colour bar indicates the values of the anisotropy parameters.

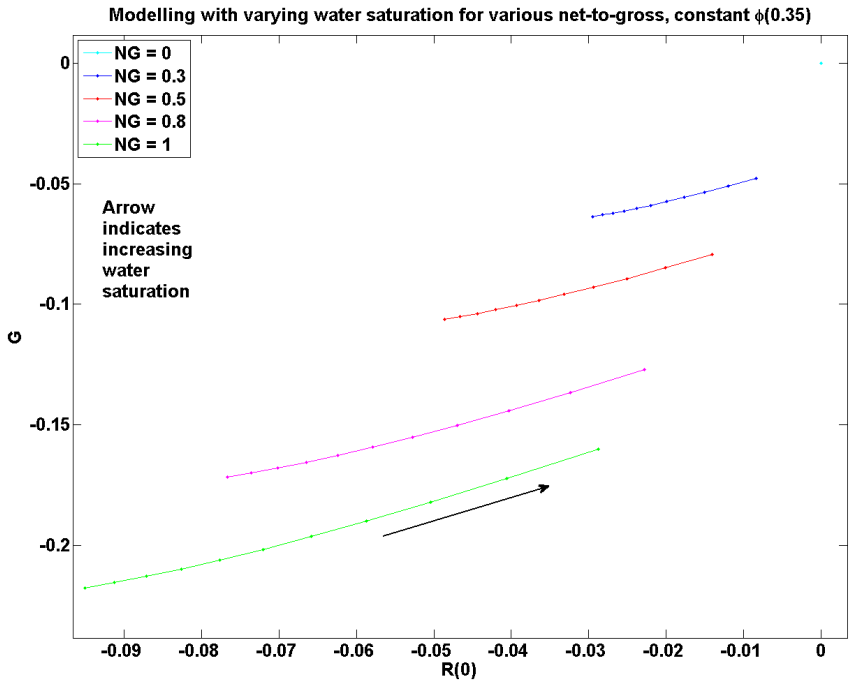

Figure 2.11: AVO crossplot of intercept, R(0) and gradient, G as a function of varying Water saturation

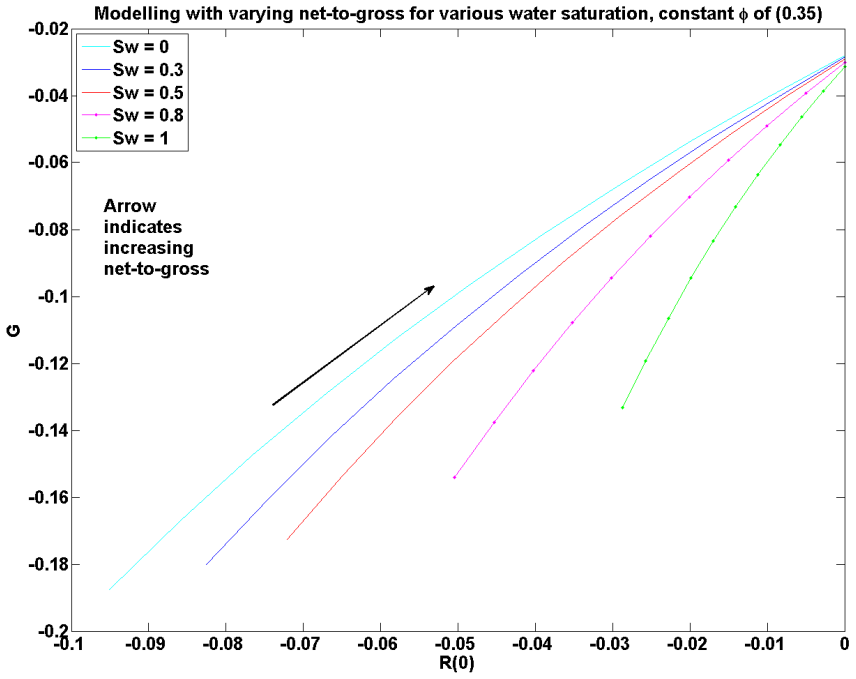

Figure 2.12: AVO crossplot of intercept, R(0) and gradient, G as a function of varying net-to-gross

.

Figure 2.11 shows the AVO cross-plot of intercept and gradient for the results of increasing water saturation for constant porosity of 0.35 for various net-to-gross. One notice that the gradient and intercept increase with increasing water saturation for any particular net-to-gross. Also it can be

observe that the effect of water saturation on these AVO attributes becomes less pronounced for lower net-to-gross. The AVO cross-plot of intercept and gradient for the results of increasing net-to-gross for constant porosity of 0.35 for various water saturation is shown on figure 2.12 and it can be seen that the gradient and intercept decrease with increasing net-to-gross and the decrease in these attributes becomes less pronounced for 100% water saturation.

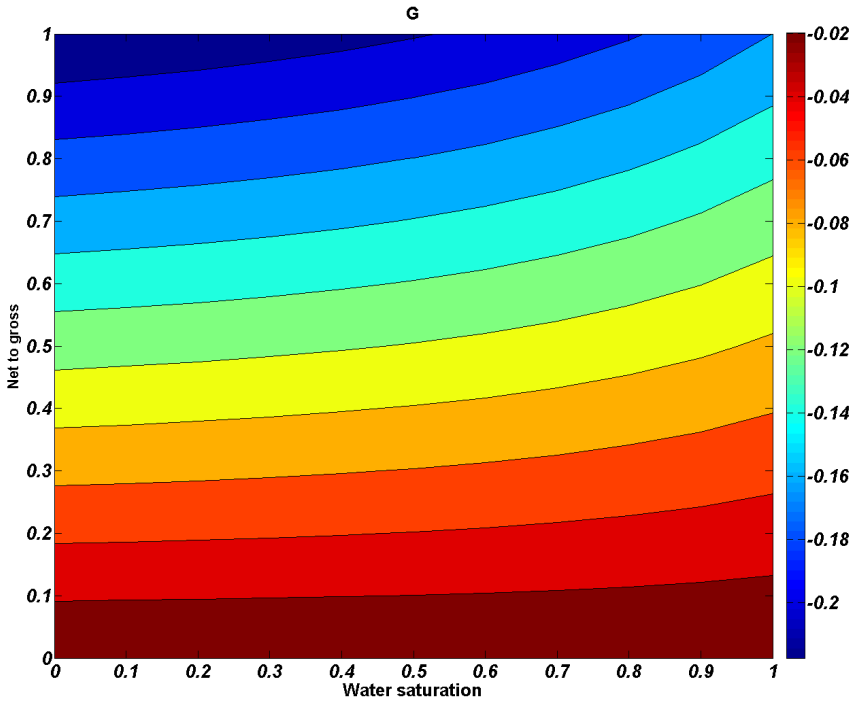

Figure 2.13: Contour plots showing the dependence of AVO gradient(G) on net-to-gross ratio and water saturation

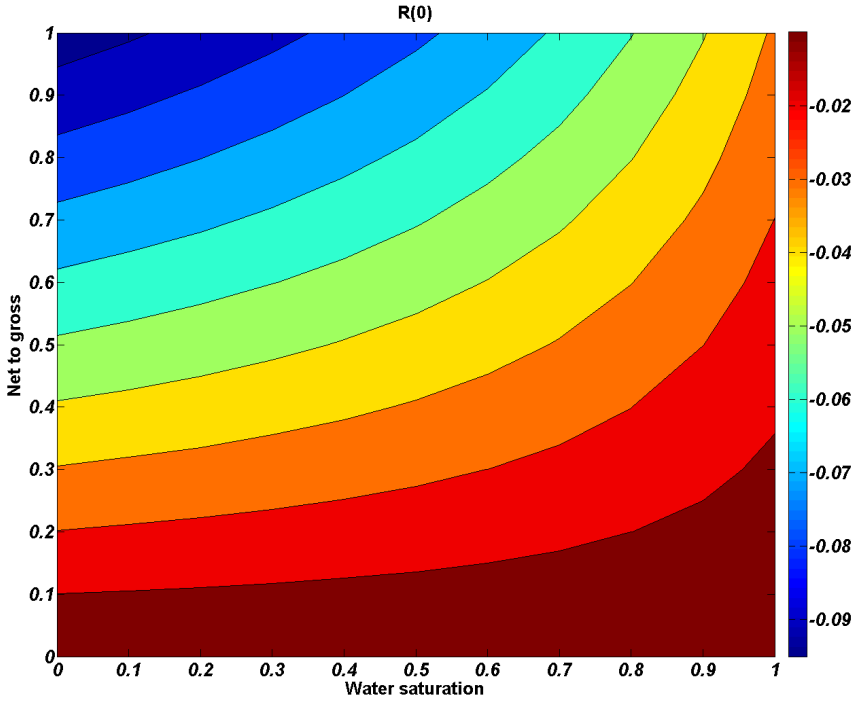

Figure 2.14: Contour plots showing the dependence of intercept(R(0)) on net-to-gross ratio and water saturation

.

The dependence of AVO gradient and intercept on net-to-gross and water saturation is shown on the contour plot in figure 2.13 and 2.14 respectively. The intercept and gradient increase with increasing water saturation as the net-to-gross increases. The effect of net-to-gross and saturation is more significant on AVO intercept compared to gradient.

The modelling results are important in understanding the order of variation of rock physics and AVO attributes as a function of these various geological parameters, when these models are applied on real datasets.

Chapter 3

Methodology

3.1 Data overview

The elastic properties of the formation are obtained from the borehole sonic data. Three wells from the North sea are examined in this study. Two of these wells (Well 25/4-7 and 25/4-K3H) penetrate the same lobe structure(Kneler structure) and both encountered oil only. Well 25/4-7, which is a vertical well is located to the west of the Heimdal Field in the North sea. From NPD's open well database website, the oil-water contact is located at 2132.5m and it consists predominantly of heterolithic dominated sequence and massive sandstone. The second well, well 25/4-K3H, is however a deviated well, which has its deviation angle at a range of $45 - 72°$. The seismic section with the location of these two wells is shown in figure 3.1 and the composite log of these two wells are also shown in figure 3.2.

The third well, well 24/6-2(Kamelon discovery) is a vertical well from the Alvheim field and this well encountered both oil and gas. The oil and gas were encountered within the Heimdal T60 sand. The gas zone extended from the top of the reservoir at 2099m and down to the oil-gas contact at 2151m (52m gross) and the oil extended down to the oil- water contact at 2168m (17m gross). Figure 3.3 shows the seismic section including near, far and computed far-near stack with the location of this well(well 24/6-2) in relation to the vertical well 25/4-7 and figure 3.4 shows the composite log of well 24/6-2. These provided sonic data composed of compressional velocity, shear velocities, bulk density, gamma ray, resistivity and neutron log. The gamma ray log is used to estimate the volume of shale, and the shale volume is consequently used to compute the net to gross. V_p/V_s ratio and acoustic impedance are estimated from these basic acquired data.

By contrast, the velocities of the vertical well(figure 3.2a) is observed to slower than the velocities of the deviated well at same vertical depth range. Furthermore, this difference is more significant in region with higher gamma log value (predominantly shale units). In the next section, I proposed a method to correct for the deviated well and account for the effect of anisotropy.

Another set of data used in this work is the AVO horizon attribute data and slides for the top of

the reservoir at Alvheim field. The data composed of calibrated AVO intercept as well as gradient, two way traveltime and inline and xline information. The two vertical wells (25/4-7 and 24/6-2) top reservoir levels are located on this horizon slides as shown in figure 3.5a and 3.5b. The calibrated AVO intercept(R_0) and gradient(G) will be inverted for rock physics attributes (V_p/V_s and acoustic impedance) and the crossplot of these attributes will be superimposed on the rock physics templates and the variations in net-to-gross between the two wells are investigated.

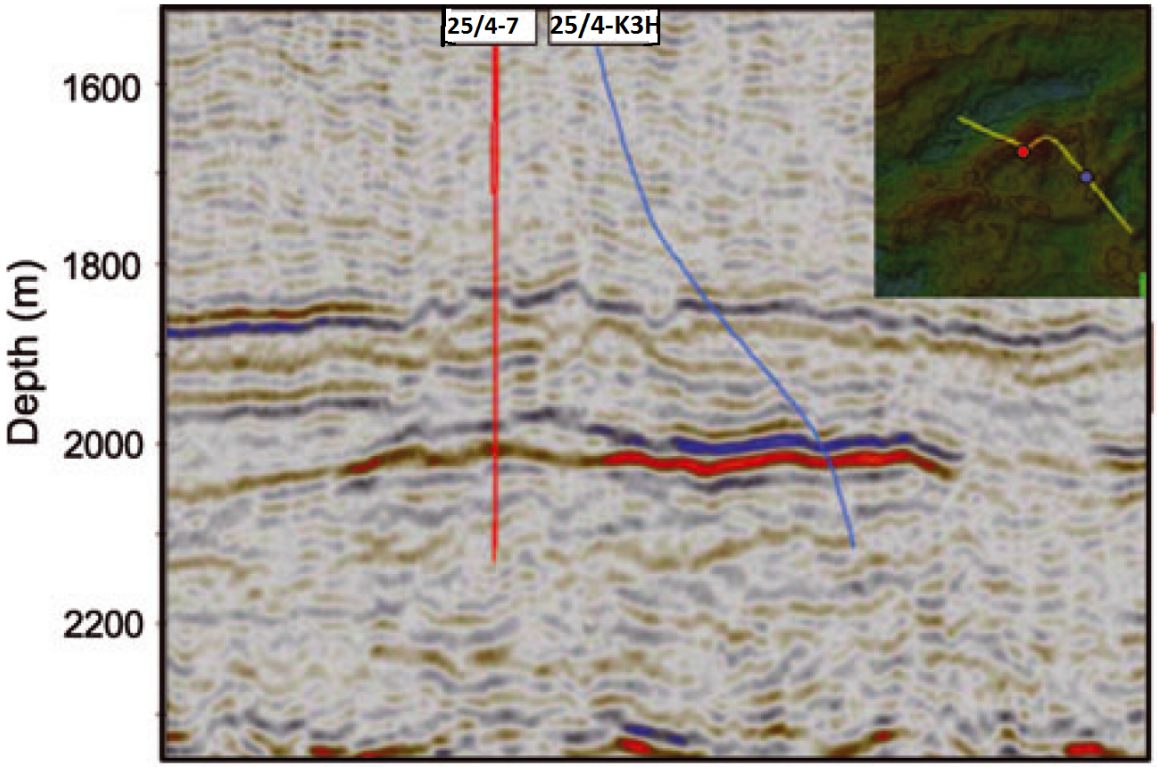

Figure 3.1: Seismic section with the location of two of the three wells studied(Golikov et al., 2013). Well 25/4-7 (indicated by the red line) is a vertical well and well 25/4-K3H (indicated by the blue line) is the deviated well. Both wells penetrate the same lobe structure (Kneler structure).

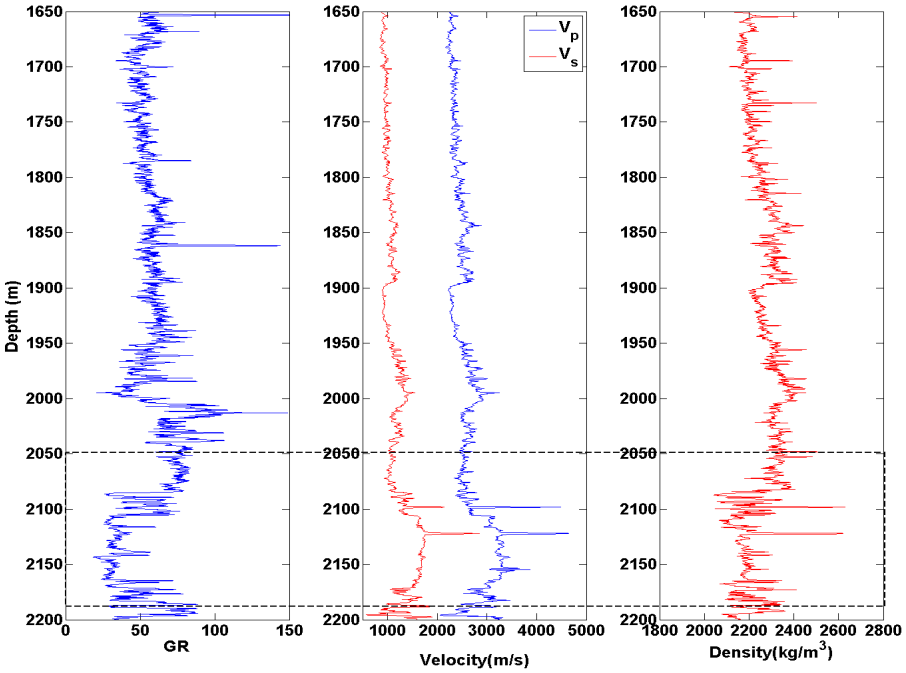

(a)

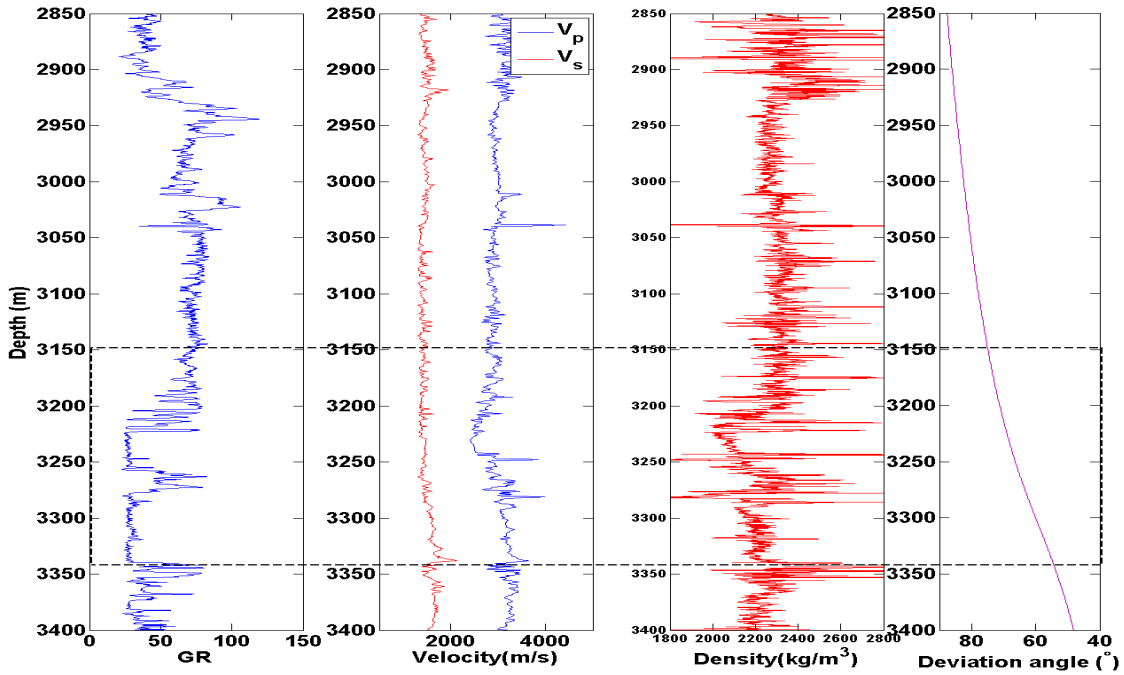

(b)

Figure 3.2: Composite well Log of two of the three wells used in this study. The upper well log(a) is the vertical well (Well 25/4-7) and the lower log (b) is the corresponding deviated well (Well 25/4-K3H). The first, second and third track of the two wells consist of gamma ray, velocities (Compressional and shear) and bulk density respectively. The fourth track in the lower log (b) is the apparent deviation angle. The target zone(reservoir region) is marked by the black dashed line

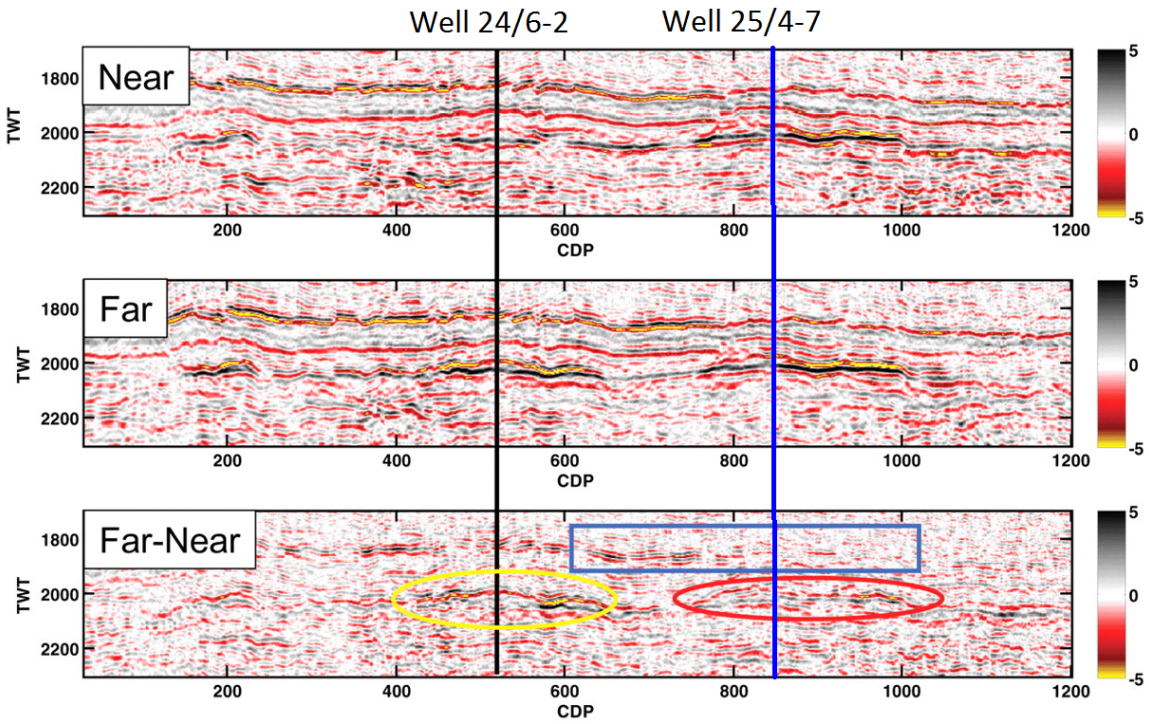

Figure 3.3: Seismic section including near, far and computed far-near stack with the indication of the two vertical wells studied. Well 24/6-2 (Kamelon discovery well), which has both oil and gas discovery (indicated by black line) and well 25/4-7 (Kneler discovery), which is only an oil discovery (indicated by blue line). This reservoir zones are indicated by the red and yellow oval shape and the background trend is indicated by the blue retangle

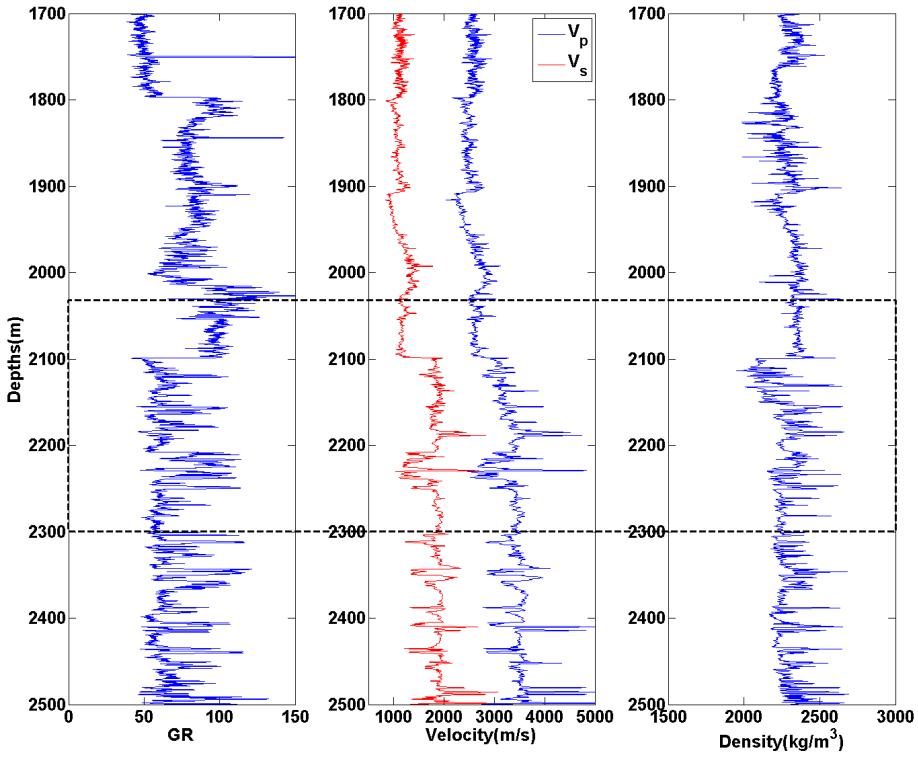

Figure 3.4: Composite well Log of third well, well 24/6-2 examined in this study. The first, second and third track of the two wells consist of gamma ray, velocities (Compressional and shear) and bulk density respectively. The target zone(reservoir region) is marked by the black dashed line

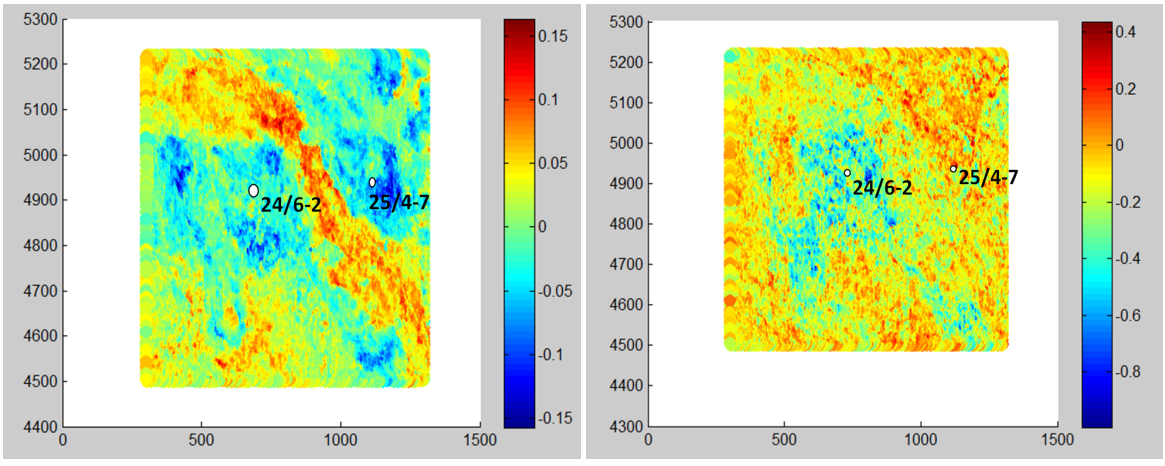

(a) (b)

Figure 3.5: AVO horizon attribute slides for the top of the reservoir at Alvheim field showing the location of the two vertical wells (well 24/6-2 and well 25/4-7). a) Calibrated AVO intercept b) Calibrated AVO gradient

3.2 Rock physics modelling workflow

This section follows the modification of rock physics modeling and upscaling of sand-shale sequences workflow presented in Avseth et al. (2010). The modified workflow uses the anisotropic velocities given by equation 2.14 and 2.15 to estimate the seismic velocities propagating through the effective medium at any particular angle. All 5 independent stiffness coefficients for the effective medium are averaged for various net to gross values using the Backus equation given by equation 2.21. The algorithm for the workflow is as follows:

- The Hertz Mindlin contact theory (Mindlin, 1949) is applied to estimate the elastic moduli of pure closely packed sand at critical porosity. The elastic moduli of the dry well-sorted end member at critical porosity is given by the Hertz-Mindlin theory below:

$$K_{HM} = \left[\frac{n^2 \cdot (1-\phi_c)^2 \cdot \mu^2}{18 \cdot \pi^2 \cdot (1-\nu)^2} \cdot P\right]^{\frac{1}{3}}, \tag{3.1}$$

$$\mu_{HM} = \frac{5-4\nu}{5 \cdot (2-\nu)} \left[\frac{3 \cdot n^2 \cdot (1-\phi_c)^2 \cdot \mu^2}{2 \cdot \pi^2 \cdot (1-\nu)^2} \cdot P\right]^{\frac{1}{3}}, \tag{3.2}$$

  where K_{HM} is the dry bulk modulus, and μ_{HM} is the shear modulus, both at critical porosity, ϕ_c, P is the effective pressure (i.e, the difference between the overburden pressure and the pore pressure); μ and ν are the shear modulus and Poisson's ratio of the solid phase; and n is the coordination number (the average number of contacts per grain).

- Secondly, the moduli of the dry sands with porosities from 0 to ϕ_c are "interpolated" between the zero porosity mineral point and the high porosity well-sorted end member using the lower Hashin and Shtrikman (1963) bound. Also model the modified Hashmin –Shtrikman bound, contact cement model, and the constant cement lines from 0% to 10% can also be applied.

  At porosity ϕ the concentration of the pure solid phase in the rock is $1 - \phi/\phi_c$ and that of the original sphere-pack phase is $1 - \phi/\phi_c$. Therefore, the bulk (K_{dry})and shear (μ_dry)moduli of the dry friable sand mixture are:

$$K_{dry} = \left[\frac{\phi/\phi_c}{K_{HM} + 4 \cdot \mu_{HM}/3} + \frac{1-\phi/\phi_c}{K + 4 \cdot \mu_{HM}/3}\right]^{-1} - \frac{4}{3} \cdot \mu_{HM} \tag{3.3}$$

$$\mu_{dry} = \left[\frac{\phi/\phi_c}{\mu_{HM} + z} + \frac{1-\phi/\phi_c}{\mu + z}\right]^{-1} - z \tag{3.4}$$

where

$$z = \frac{\mu_{HM}}{6} \cdot \left[\frac{9 \cdot K_{HM} + 8 \cdot K_{HM}}{K_{HM} + 2 \cdot \mu_{HM}} \right] \tag{3.5}$$

- Thirdly, Gassmann theory (as explained in section 2.2) is applied on the the estimated dry bulk (K_{dry}) and shear (μ_{dry}) moduli for fluid substitution, thereby estimating the bulk moduli with various fluid saturations.

- Finally, Backus averaging method(discussed in section 2.3) is applied for the estimation of the effective, upscaled anisotropic parameters of the interbedded shale-sand sequences for net to gross range of 0 to 1. The shale in the sequence can be derived from typical shale properties from well log data in the study area. The shale properties used for this study is shown in table 2.2 and it is assumed to be completely impermeable to hydrocarbons with relatively constant porosity.

From the estimated effective parameters (C_{ij} and ρ), the anisotropic velocities (qP-, qSH- and qSV-wave velocities) propagating through the effective medium at any particular angle can then be estimated using equation 2.14 and 2.15. Consequently, the acoustic impedance and V_p/V_s can easily be computed and the rock physics templates can then be created as a cross-plot of these two attributes. Figure 3.6 and figure 3.7 show the created rock physics templates of V_p/V_s and acoustic impedance for varying net to gross and saturation from the above workflow, figure 3.6 is created for propagation angle of 0° (i.e vertical RPT) and figure 3.7 is created for propagation angle of 72° , which is typical of the studied deviated well. This rock physics templates are superimposed on the vertical and deviated well-log data and the results are presented in the next chapter.

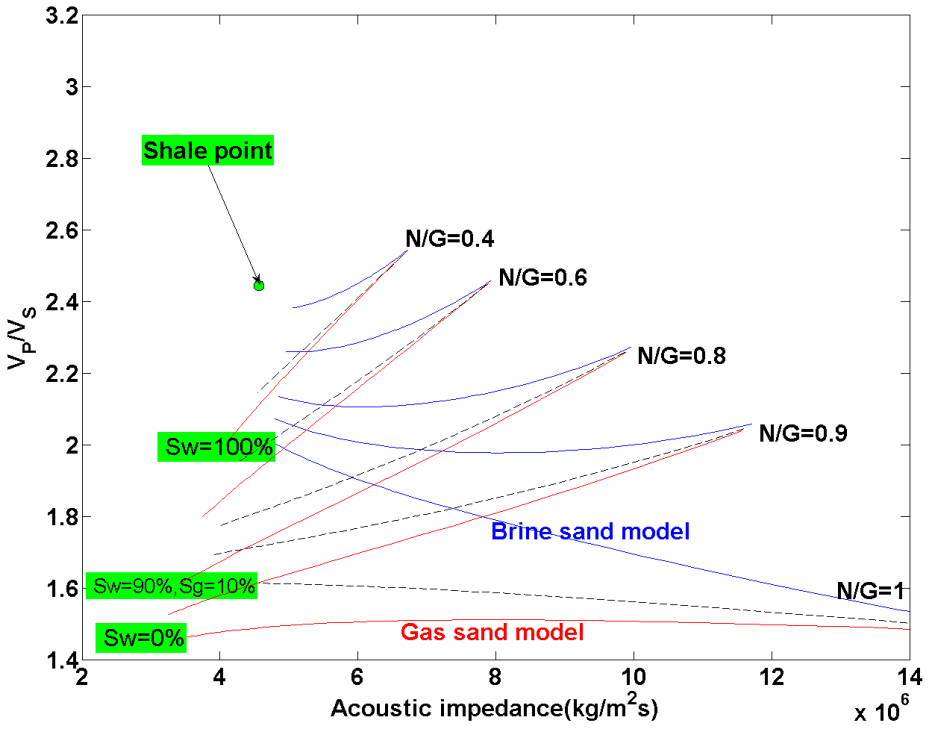

Figure 3.6: Rock physics templates of V_p/V_s and acoustic impedance for varying net to gross and saturation from this workflow, the template is created for propagation angle of $0°$ (i.e vertical RPT).

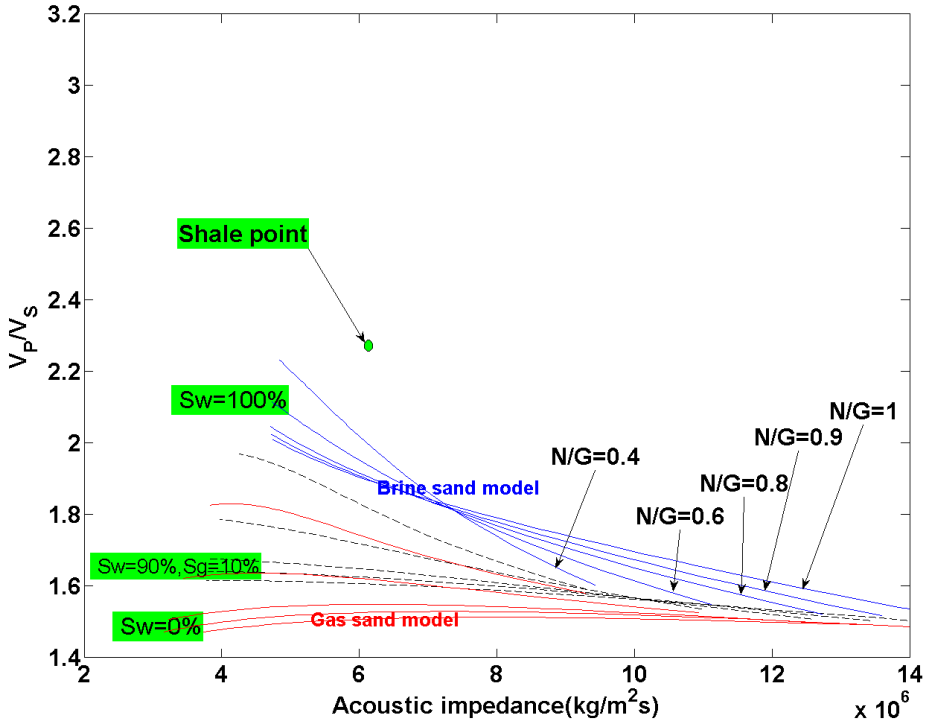

Figure 3.7: Rock physics templates of V_p/V_s and acoustic impedance for varying net to gross and saturation from this workflow, the template is created for propagation angle of $72°$(i.e nearly horizontal RPT).

3.3 Proposed method for anisotropy correction of sonic velocities

To correct for anisotropic effects, I introduce two factors termed P-wave and S-wave anisotropy factors. The P-wave anisotropy factor, denoted by α is the ratio of the modelled compressional velocities at the deviation angle of the well to the modelled vertical compressional velocities as shown in equation 3.6. The S-wave anisotropy factor, denoted by β is the ratio of the modelled shear velocities at the deviation angle of the well to the modelled vertical shear velocities as shown in equation 3.7.

The direction of a deviated well is defined by the degree by which the polar anisotropy axes is been rotated about the axis in the isotropic plane.

$$\alpha = \frac{V_{P(\theta)}}{V_{P0}}, \tag{3.6}$$

$$\beta = \frac{V_{S(\theta)}}{V_{S0}}, \tag{3.7}$$

where $V_{P(\theta)}$ and $V_{S(\theta)}$ are the modelled P-wave and S-wave velocity at the deviation angle of the well respectively. V_{P0} and V_{S0} are the modelled vertical P-wave and S-wave velocity respectively. Figure 3.8 shows the behavior of modelled quasi-P, SV- and SH-wave velocities as a function of the phase angle and the parameters for estimating the anisotropy factors (α and β).

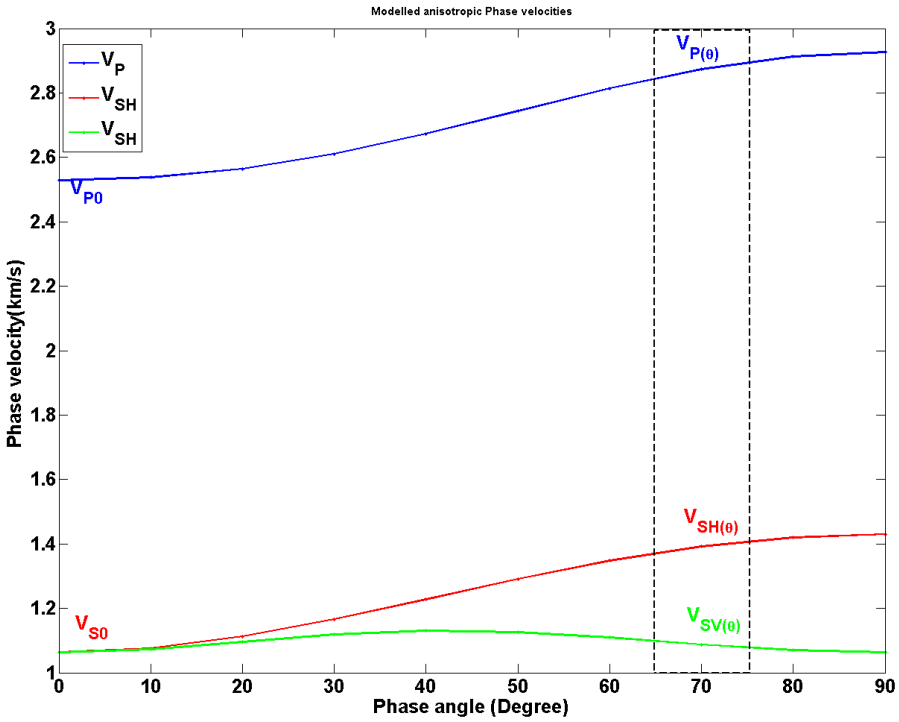

Figure 3.8: Modelled anisotropic phase velocities as a function of the phase angle with the anisotropy factor estimation parameters

From the estimation of these anisotropy factors, it is observed that $\alpha, \beta \geq 1$ and $\alpha \leq \beta$. The limitation of this method is the fact that it is only applicable for transversely anisotropic media with normal symmetry axis (VTI media).

In order to apply these anisotropy factors to the well log data, the factors are estimated for varying net to gross range of 0 to 1. The impact of these anisotropy factors is significant on reservoir with lower net to gross.

Therefore, given the deviation angle of the well and the net to gross, which is computed from the shale volume (Vsh) as explained in section 2.3,the anisotropy corrected velocities can then be easily computed using equation 3.8 and 3.9 below.

$$V_{Pcorr} = \frac{V_{P(\theta)}}{\alpha}, \tag{3.8}$$

$$V_{Scorr} = \frac{V_{S(\theta)}}{\beta}, \tag{3.9}$$

where $V_{P(\theta)}$ and $V_{S(\theta)}$ are the measured sonic P-wave and S-wave velocities of the deviated well and V_{Pcorr} and V_{Scorr} are the anisotropy corrected P-wave and S-wave velocity respectively. For a hor-

izontal or nearly horizontal beds with vertical symmetry axis, these anisotropy corrected velocities will be relatively the same as the measured velocities in vertical wells.

Certain variation in trends will occur on the rock physics template after the effect of anisotropy has been accounted for in a deviated well. Figure 3.9 and 3.10 show the rock physics template (RPT) before and after the anisotropy correction has been performed using the proposed method. Using the well input from the deviated well directly, the brine sand units and shale units superimposed on each other as seen in figure 3.9 and it is difficult to discriminate between the two lithology. However, after anisotropy correction has been applied on the data, there is a better discrimination between the shale units and brine sand units as shown in figure 3.10. Since the RPT shown in figure 3.9 and 3.10 is for clean sand saturated with brine, oil and gas, this method might seems insignificant, however, in heterogeneous reservoirs, when the sand is interbedded with shale (that is $1 > NG > 0$), the shaly oil-sand will superimpose on the brine sand, but after applying the anisotropy correction method, a better separation will be observed and consequently, enhancing the discrimination of different lithology with varying net to gross. This separation is observed when this method is applied on the provided real dataset.

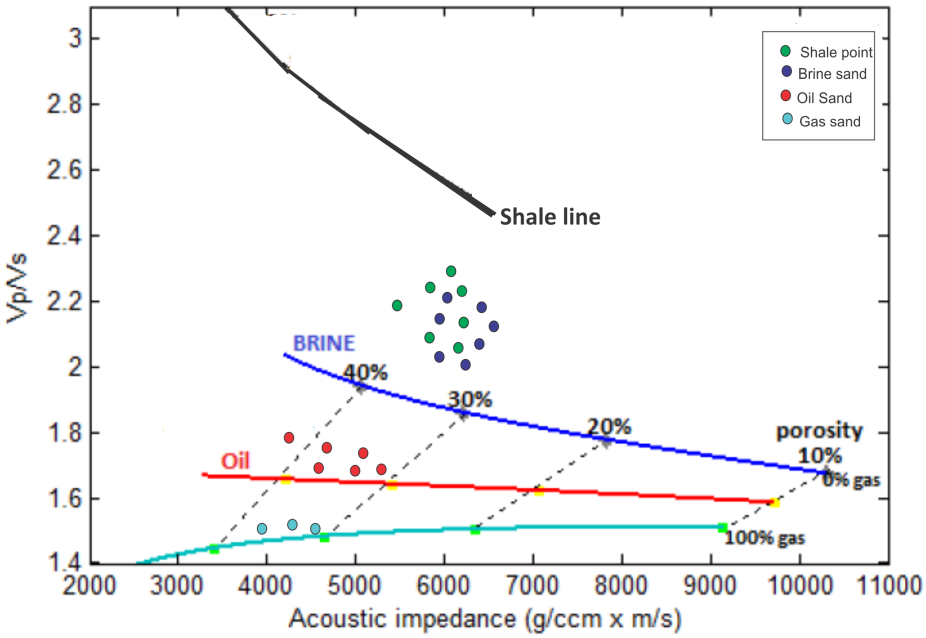

Figure 3.9: Rock physics template (RPT) before anisotropy correction is performed. Using the well input from the deviated directly, the brine sand units and shale units superimposed on each other and it is difficult to discriminate between the two lithology.

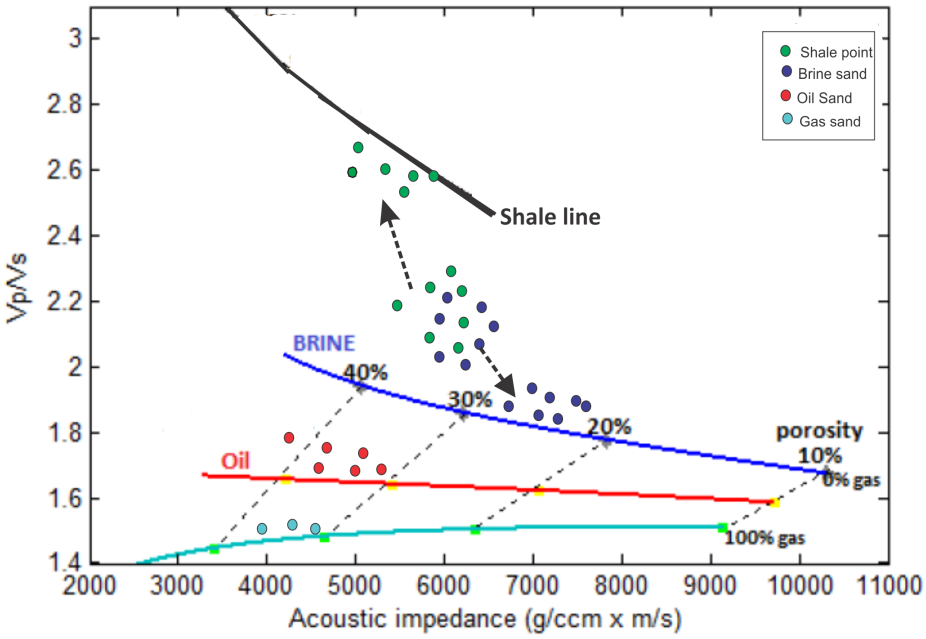

Figure 3.10: Rock physics template (RPT) after anisotropy correction has been performed using the proposed method. After the anisotropy correction has been applied on the data, there is a better discrimination between the shale units and brine sand units.

This methodology is applied to the deviated sonic log to correct for anisotropy and the results are presented in the next chapter.

3.4 Relating Thomsen parameters to vertical velocities

Vertical wells are essential in relating Thomsen parameters and anelliptic parameters with velocities. The importance is to determine how anisotropic the medium through which the well penetrate is. A clean sand and impermeable clean shale are defined from the vertical well data. The clean sand is determined from the well-log for data with net-to-gross of one and the impermeable shale is obtained from data with net-to-gross of zero. The major limitation of this relation is the assumption that sand and shale properties in thin layer where $1 > NG > 0$ are similar to those measured with NG=1 (clean sand) and with NG=1 (clean shale). The workflow in section 2.6 is then performed on these clean sand and shale using the net-to-gross from the well-log. Consequently the corresponding effective velocities, density and anisotropy parameters ($\varepsilon, \delta, \eta$ and σ) are estimated for the entire depth of the well log. The results are presented in the next chapter.

3.5 AVO inversion for rock physics attributes

Additional information about the lithology, net-to-gross and pore fluid of the study area can be extracted from the zero offset reflectivity (R(0)) and AVO gradient (G) from the horizon AVO attribute data. This can be achieved by inverting for the rock physics parameters (V_p/V_s and AI) from the provided AVO attributes (calibrated R(0) and G). The inversion of acoustic impedance is carried out using the zero offset reflectivity (R(0)) from the data using equation given below:

$$R(0) = \frac{AI_2 - AI_1}{AI_2 + AI_1}, \tag{3.10}$$

$$AI_2 = \frac{AI_2(R(0)+1)}{(1-R(0))}, \tag{3.11}$$

where AI_1 and AI_2 are the acoustic impedances of the overlying horizon (caprock) and underlying horizon respectively.

The inverted V_p/V_s is estimated from the shuey approximation in equation 2.24 and the expanded form of the equation is given by:

$$R(\theta) = R(0) + [R(0)A_0 + \frac{\Delta\sigma}{(1-\sigma)^2}]sin^2\theta + \frac{\Delta V_P}{V_P}(tan^2\theta - sin^2\theta), \tag{3.12}$$

where

$$\sigma = (\sigma_2 + \sigma_1)/2,\ \Delta\sigma = \sigma_2 - \sigma_1,$$

$$A_0 = B - 2(1+B)\frac{1-2\sigma}{1-\sigma},$$

$$B = \frac{\Delta V_P/V_P}{\Delta V_P/V_P + \Delta\rho/\rho},$$

and σ_1 and σ_2 are the poisson ratio of the overlying horizon (caprock) and underlying horizon respectively. Hilterman (1990) further simplified Shuey's equation with two assumptions. Firstly, by using only the first two terms and secondly, setting the poisson ratio (σ) to $1/3$ thereby making A_0 to be equal to -1. Equation 3.12 can then be simplified as follows:

$$
\begin{aligned}
R(\theta) &= R(0)(1 - sin^2\theta) + \frac{9}{4}\Delta\sigma sin^2\theta \\
&= R(0)cos^2\theta + \frac{9}{4}\Delta\sigma sin^2\theta \\
&= R(0) + (\frac{9}{4}\Delta\sigma - R(0))sin^2\theta \\
&= R(0) + Gsin^2\theta
\end{aligned}
\tag{3.13}
$$

Therefore,

$$
G \approx \frac{9}{4}\Delta\sigma - R(0), \tag{3.14}
$$

$$
\sigma_2 = \sigma_1 + \frac{4}{9}(G + R(0)), \tag{3.15}
$$

$$
V_p/V_{s2} = \sqrt{\frac{2 - 2\Delta\sigma_2}{1 - 2\Delta\sigma_2}}, \tag{3.16}
$$

where V_p/V_{s2} is the predicted (or inverted) V_p/V_s ratio of the underlying horizon. From the above equations, it is important to make assumption for the values of the acoustic impedance and Poisson ratio of the overlying horizon (caprock). From the well log analysis, it is found that the expected acoustic impedance of the capping Lista Fm is $6.54km/s * g/cm^3$. And the expected Poisson ratio of the Lista shale (σ_1) is estimated to be 0.39. It is assumed that the underlying horizon is representative for the Top Heimdal sandstones, and the thickness of the sands are above the seismic resolution and tuning thickness.

Then the crossplot of the estimated AI and V_p/V_s from this inversion process are superimposed on the rock physics model in figure 3.6. This process is performed for the two vertical wells and the observed trends and difference in net-to-gross of the two wells are shown and discussed in the next chapters.

Chapter 4

Results

This chapter presents the results of the analyses performed on the provided data. The focus is on the target zone of these data. I present various rock physics models in the previous chapter, in this chapter, these models are superimposed on the well log data and comparisons are made. Different lithologic and fluid trends and variations are also observed. The presentation of these results follows the sequential steps at which the works are carried out. Starting with the vertical well log (well 24/6-2) from the Alvheim field, the target zone is considered as shown in figure 4.1. This target zone contains both turbiditic oil and gas reservoir and the net to gross is below 1 since the reservoir sand is interbedded with laminated shale. This well is examined to better understand how lithology with different fluid contents varies on the rock physics templates. The rock physics template is created using propagation angle of 0° (i.e. vertical RPT) for models with varying net-to-gross (0.8-1) and varying gas saturation. And the well log data is then superimposed on this template as shown in figure 4.2.

Another vertical well is examined. In this case, the main purpose of considering this well is to compare the well with deviated well, that the results will presented later in this chapter. The vertical well (well 25/4-7) as detailed in section 3.1 is relatively close to the deviated well. The well is an oil discovery and the well log for the target zone is shown in figure 4.3. The well data is also superimposed on a vertical rock physics template as shown in fig 4.4. The vertical RPT is created for varying oil sand model since the well contains no gas discovery and for models with different net-to-gross.

Subsequently, the deviated well(well 25/4-K3H) is analysed. The well penetrates the same lobe structure as well 25/4-7 (as shown in figure 3.1). The well log for the target zone is shown in figure 4.5. The rock physics template superimposed on this deviated well data is created using propagation angle of 72° (i.e. nearly horizontal RPT) for models with different net-to-gross (0.8-1) and varying oil sand model. And the well log data is then plotted on this template as shown in figure 4.6.

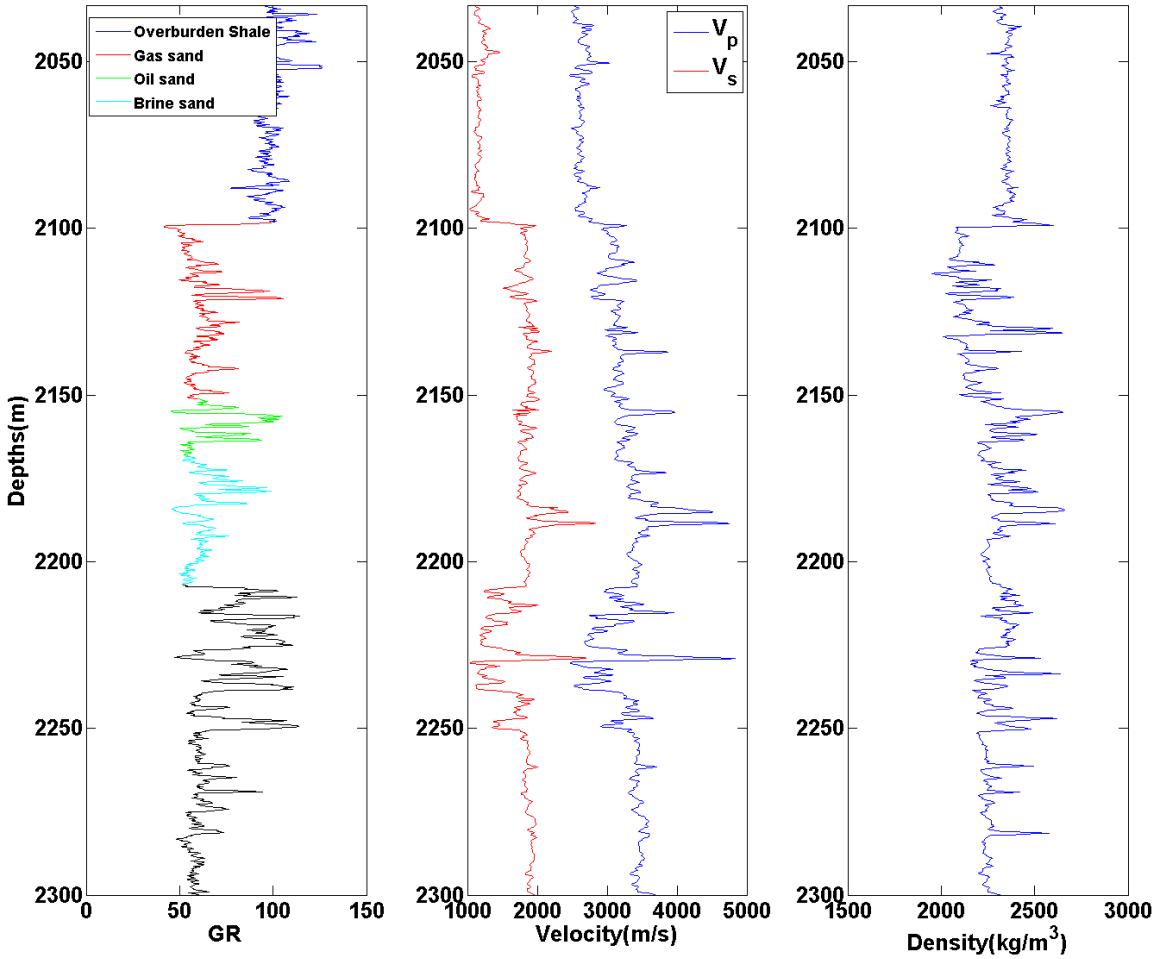

Figure 4.1: Well log data from the target zone of vertical well, well 24/6-2 of the Alvheim field from the North sea. The log includes the gamma ray (track 1), sonic compressional and shear wave(track 2) and density (track 3). The well has both oil and gas discovery and the reservoir sand is interbedded with laminated shale.

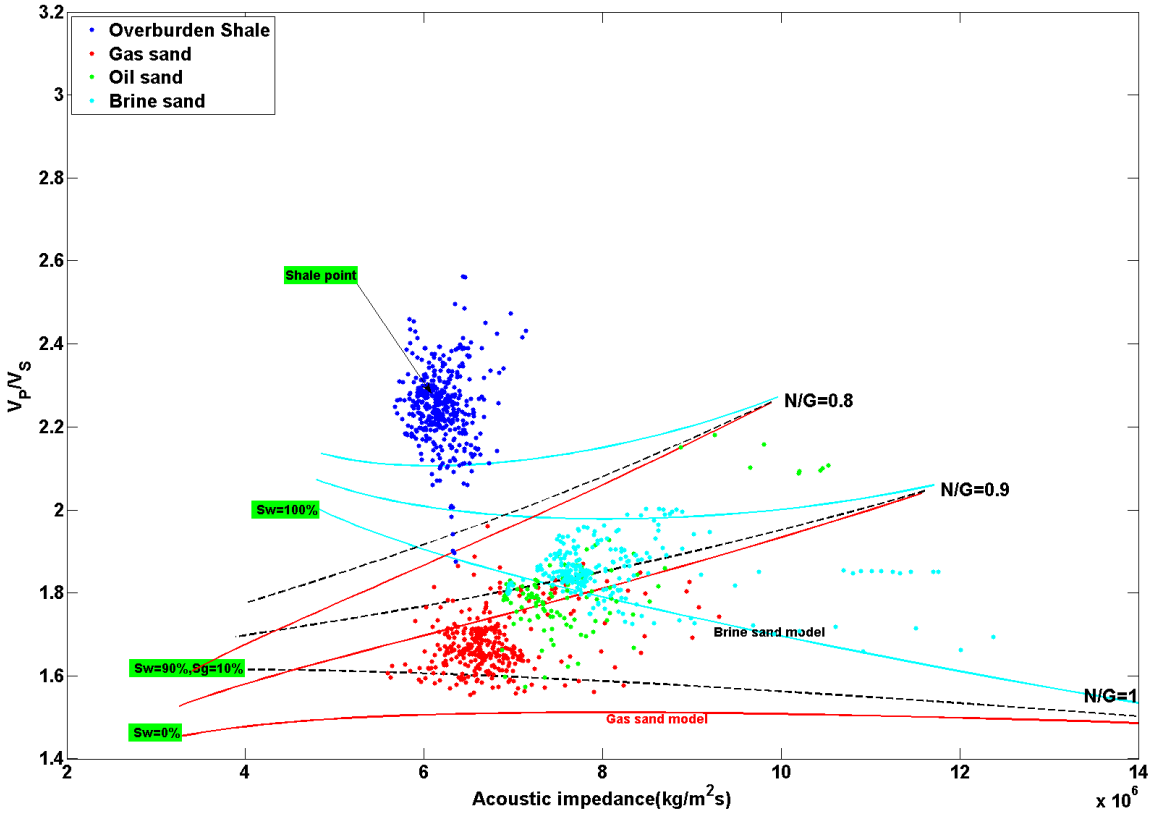

Figure 4.2: Vertical rock physics template of V_p/V_s versus acoustic impedance (AI) for models with different net-to-gross at varying gas saturation. Well log data from vertical well (well 24/6-2) is superimposed on this template

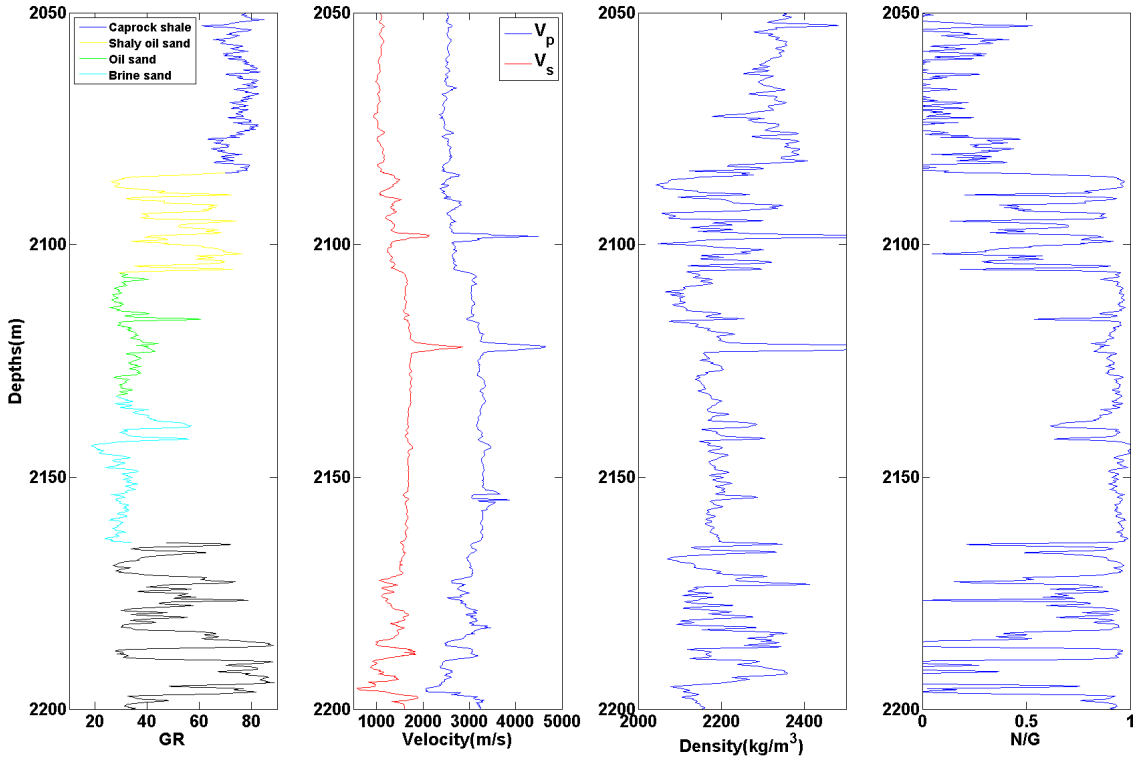

Figure 4.3: Well log data from the target zone of vertical well, well 25/4-7 of the Kneeler Structure from the North sea. The log includes the gamma ray (track 1), sonic compressional and shear wave(track 2), density (track 3) and net-to-gross (track 4). The well is an oil discovery and the reservoir sand is interbedded with laminated shale.

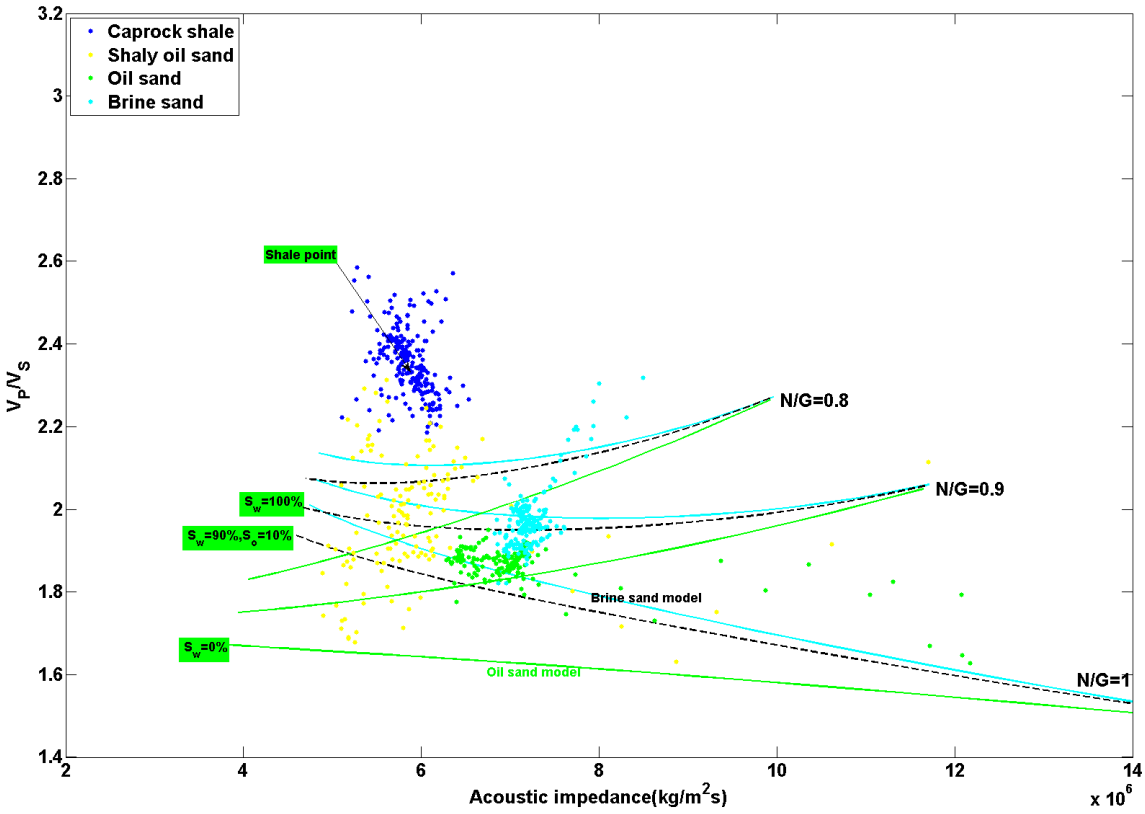

Figure 4.4: Vertical rock physics template of V_p/V_s versus acoustic impedance (AI) for models with different net-to-gross and varying oil sand model. Well log data from vertical well (well 25/4-7) is superimposed on this template

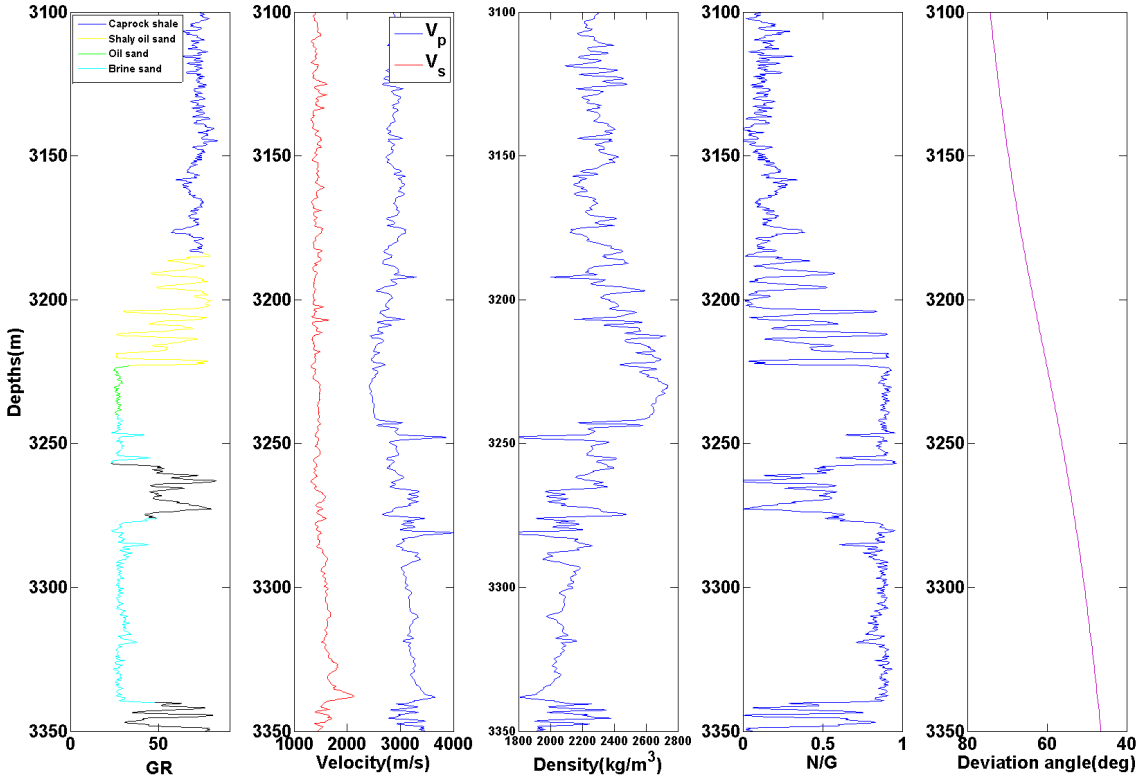

Figure 4.5: Well log data from target zone of the deviated well, 25/4-K3H from the North sea. The log includes the gamma ray (track 1), sonic compressional and shear wave(track 2), density (track 3) and net-to-gross (track 4) and apparent deviation angle (track 5). The well is an oil discovery and the reservoir sand is interbedded with laminated shale.

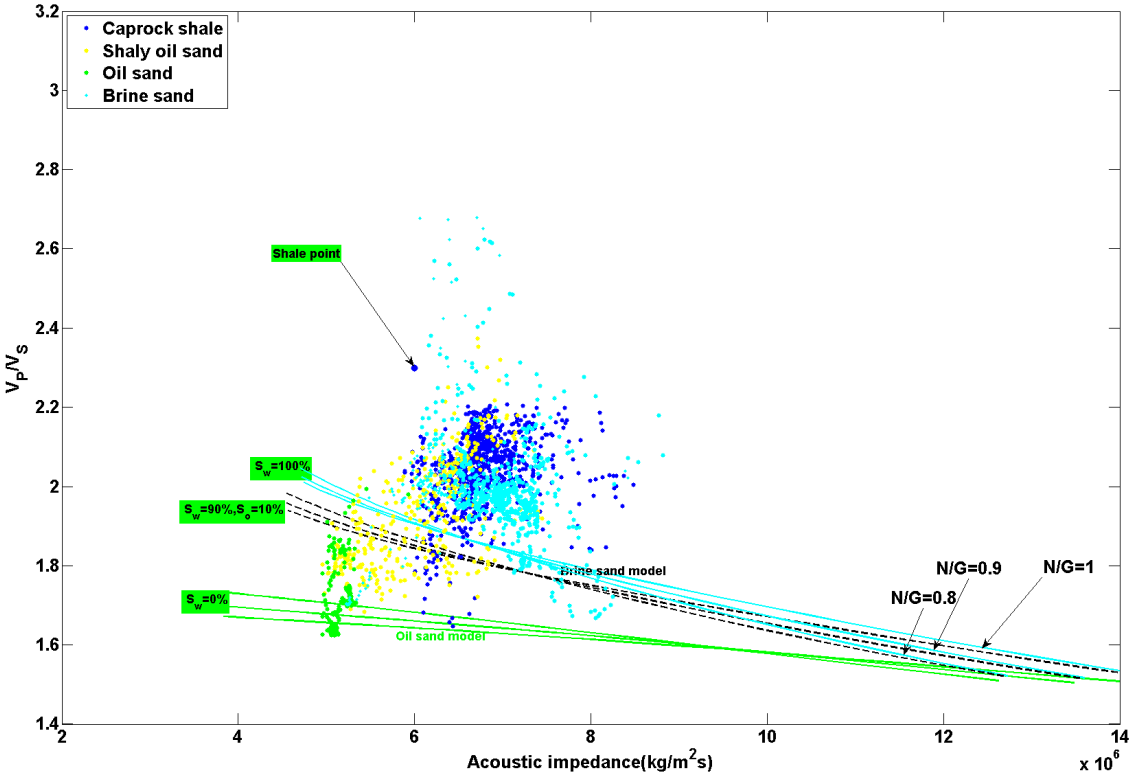

Figure 4.6: Horizontal Rock physics template of V_p/V_s versus acoustic impedance (AI) for models with different net-to-gross and varying oil sand model. Well log data from the target zone of the deviated well, 25/4-K3H is superimposed on this template

The magnitude of the anisotropy is determined by relating Thomsen parameters and anelliptic parameters to the vertical wells. Figure 4.7 shows the well log input and effective well log data of the provided vertical well estimated following the explanation in section 3.4. The Thomsen parameters and anelliptic parameters are estimated using equation 2.6 to 2.10.

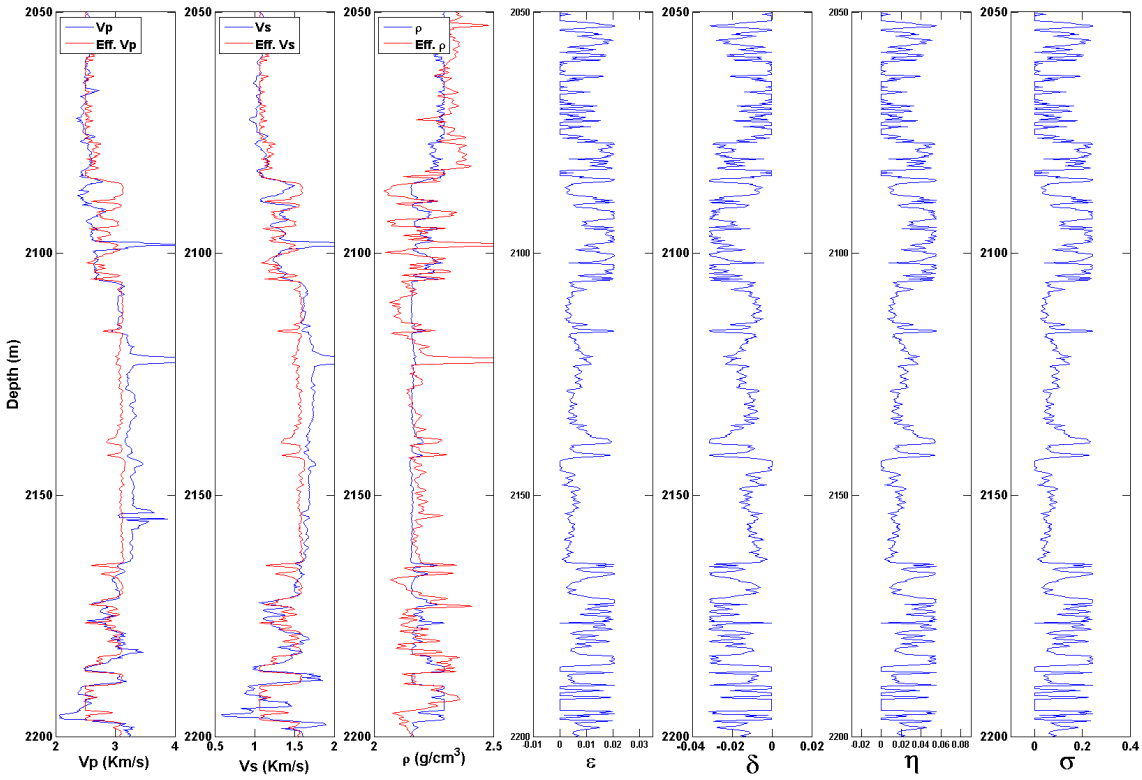

Figure 4.7: Well log input and effective well log data of the provided vertical well. The log inputs include the acquired and effective P-velocity (track 1), acquired and effective P-velocity (track 2), acquired and effective density (track3), Epsilon (track 4), delta (track 5), eta (track 6) and sigma (track4).

4.1 Anisotropy Correction results

The anisotropy correction method proposed in section 3.3 is applied to the deviated well to account for anisotropic effect on the well. The anisotropy corrected log is shown in figure 4.8. The corrected log is then superimposed on a vertical rock physics template as shown figure 4.9.

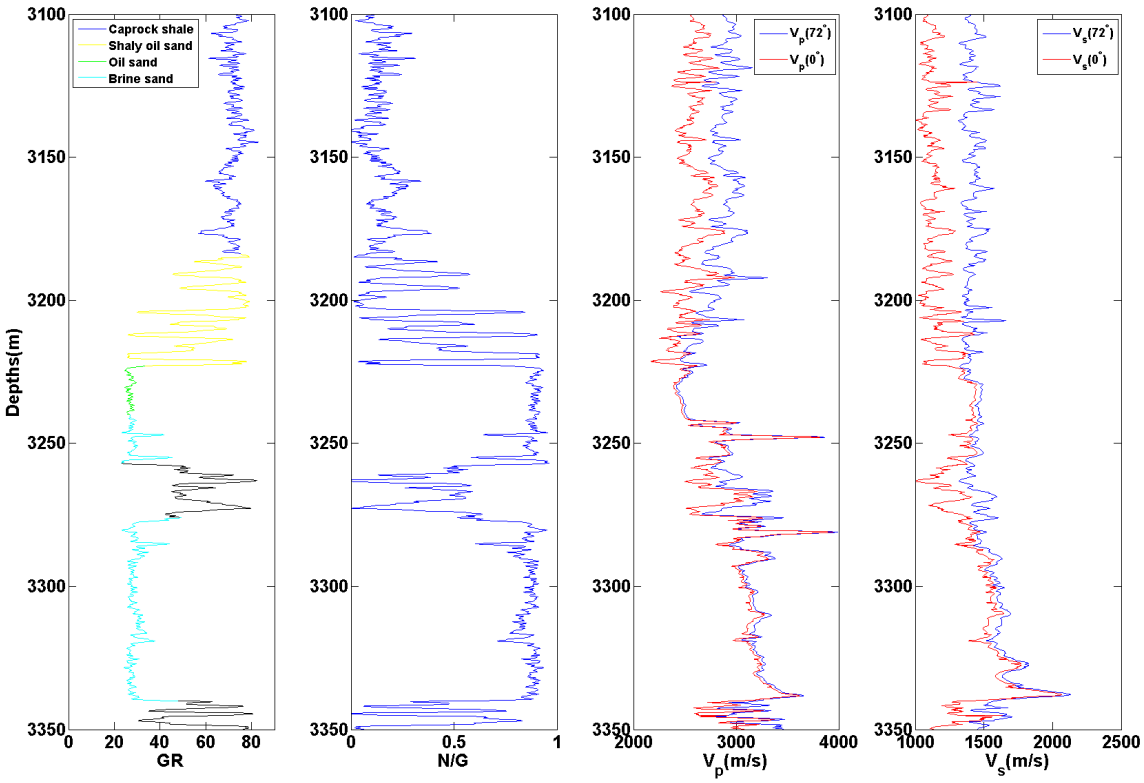

Figure 4.8: Well log of the anisotropy corrected well and the actual deviated well. The log inputs include the gamma ray (track 1), net-to-gross (track 2), sonic compressional log before(red) and after correction(blue) (track3) and sonic shear log before(red) and after correction(blue) (track4).

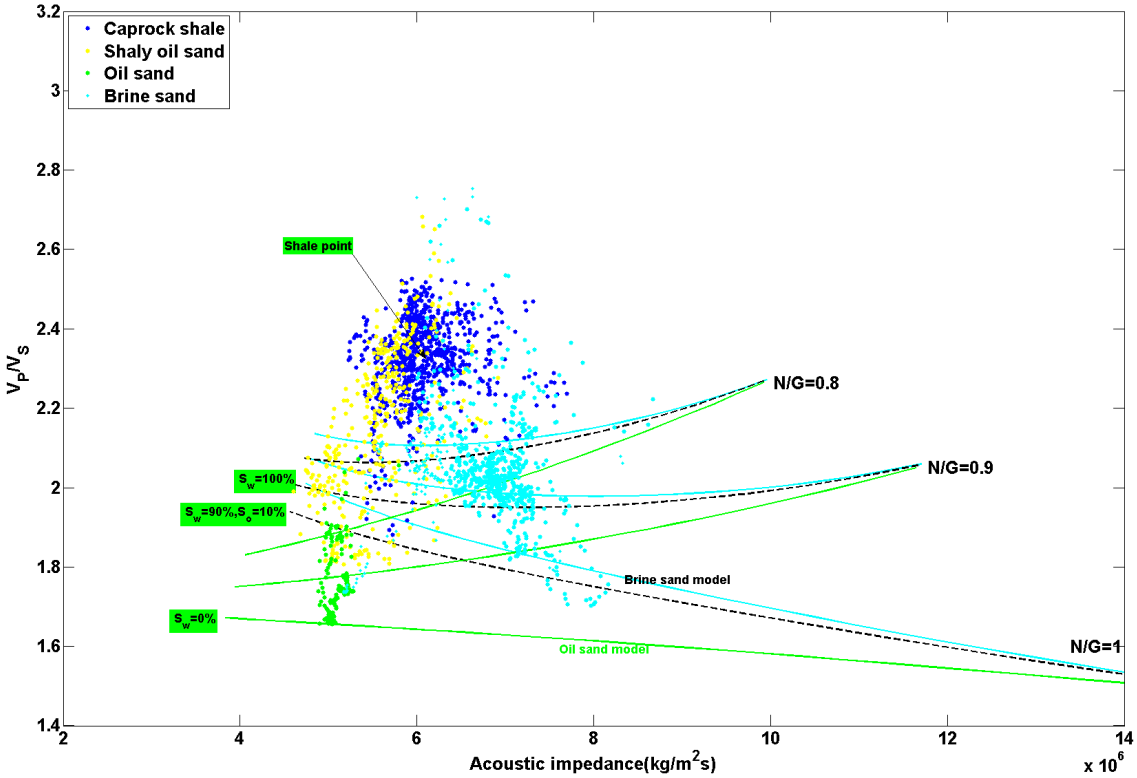

Figure 4.9: Vertical rock physics template of V_p/V_s versus acoustic impedance (AI) for models with different net-to-gross and varying oil sand model. The anisotropy corrected well log is superimposed on this template

Figure 4.10 to 4.13 show the rock physics models in a 3D cross-plot of AI versus V_P/V_S and NG for different net-to-gross and saturation at propagation angle of 0° and 72°. The porosity of the sand is kept constant at 0.40 and the well log data for vertical well, deviated well and anisotropy corrected well are superimposed on these 3D templates.

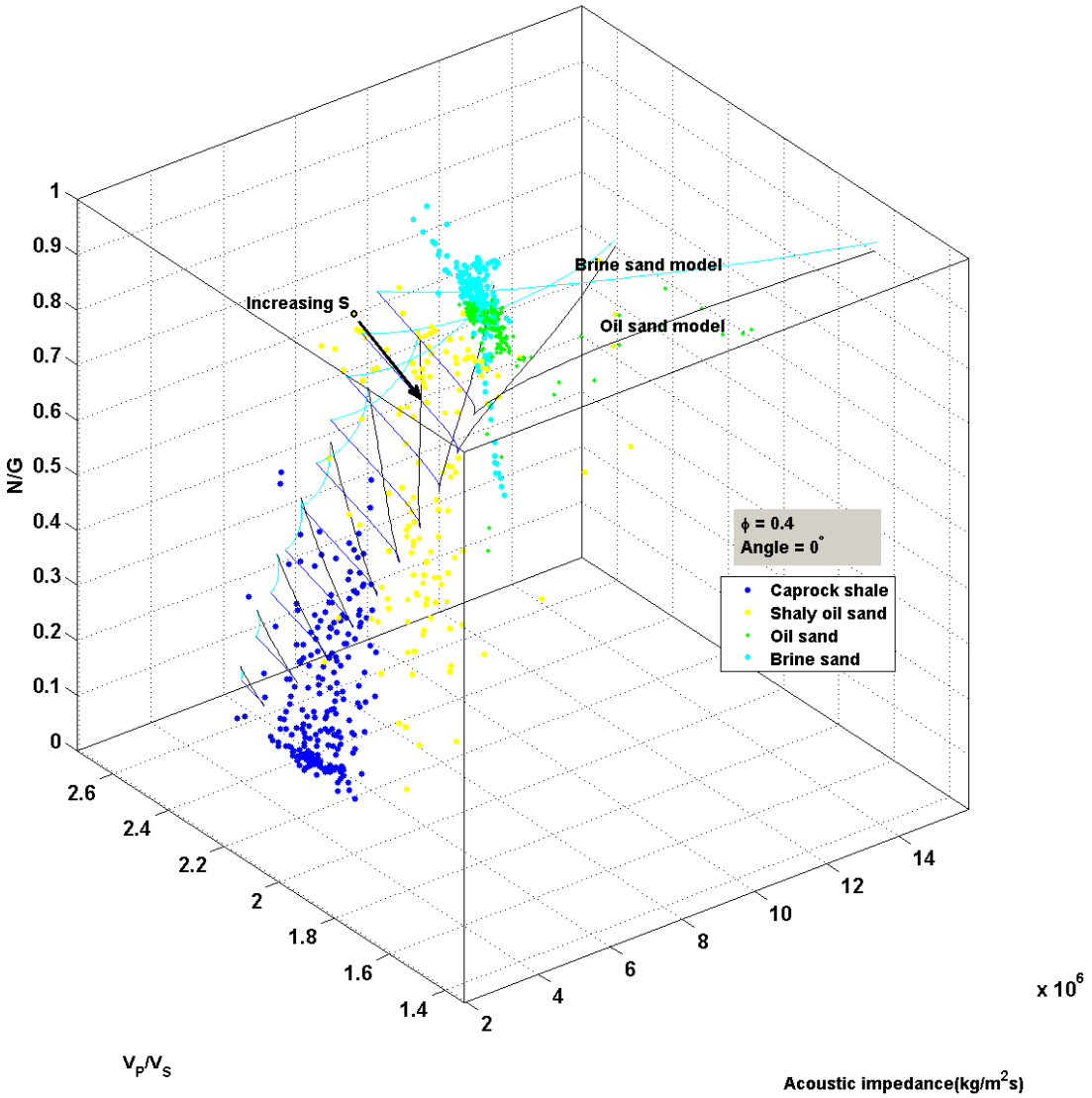

Figure 4.10: 3D Cross-plot of AI versus V_P/V_S and NG. The rock physics template model is created using propagation angle of $0°$ (vertical RPT) for different net-to-gross and saturation. The sand porosity remains constant at 0.40 and the well log data from the target zone of the vertical well, 25/4-7 is superimposed on this model. The well log data follows a particular trend.

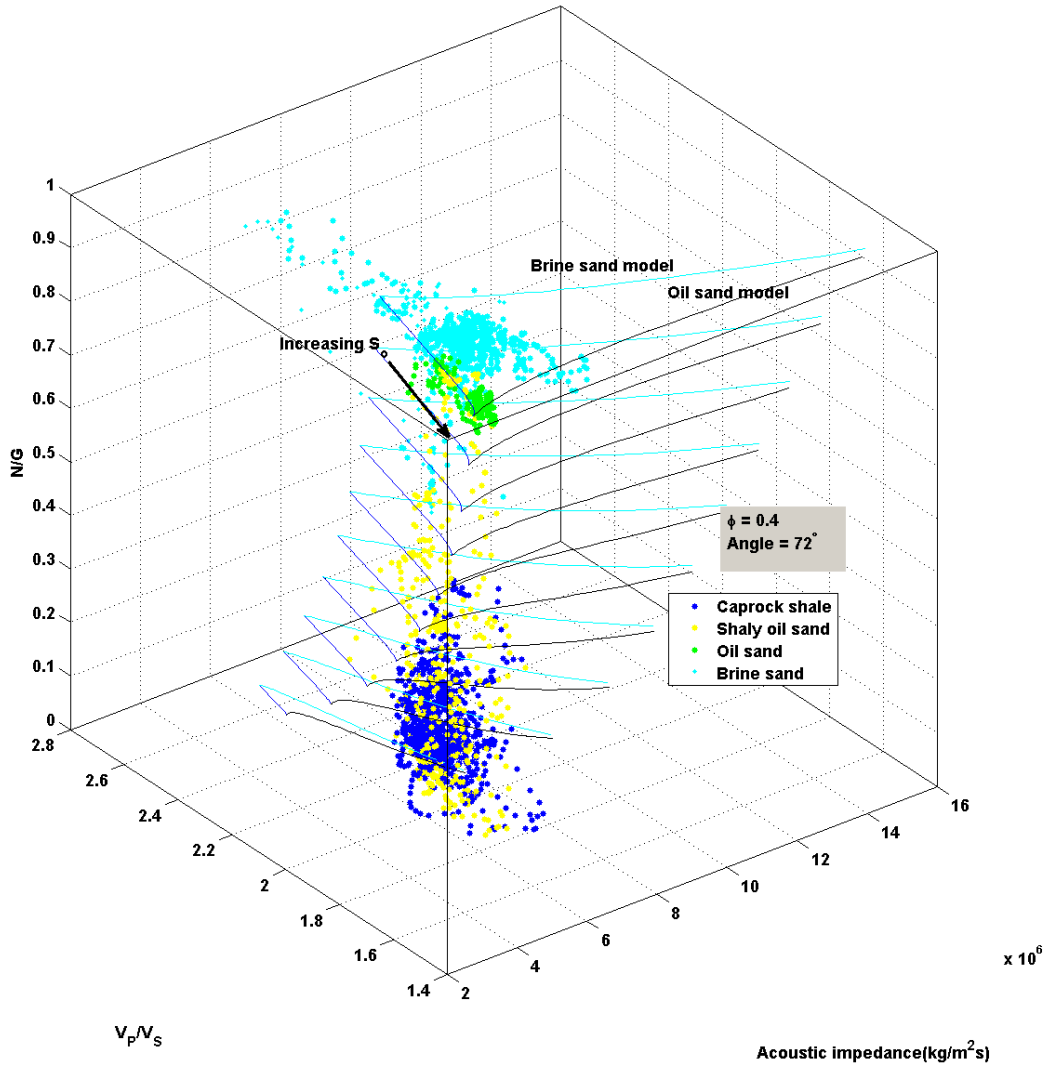

Figure 4.11: 3D Cross-plot of AI versus V_P/V_S and NG. The rock physics template model is created using propagation angle of 72° (vertical RPT) for different net-to-gross and saturation. The sand porosity remains constant at 0.40 and the well log data from the target zone of the deviated well is superimposed on this model. The well log data follows a different trend from that of vertical well in figure 4.10.

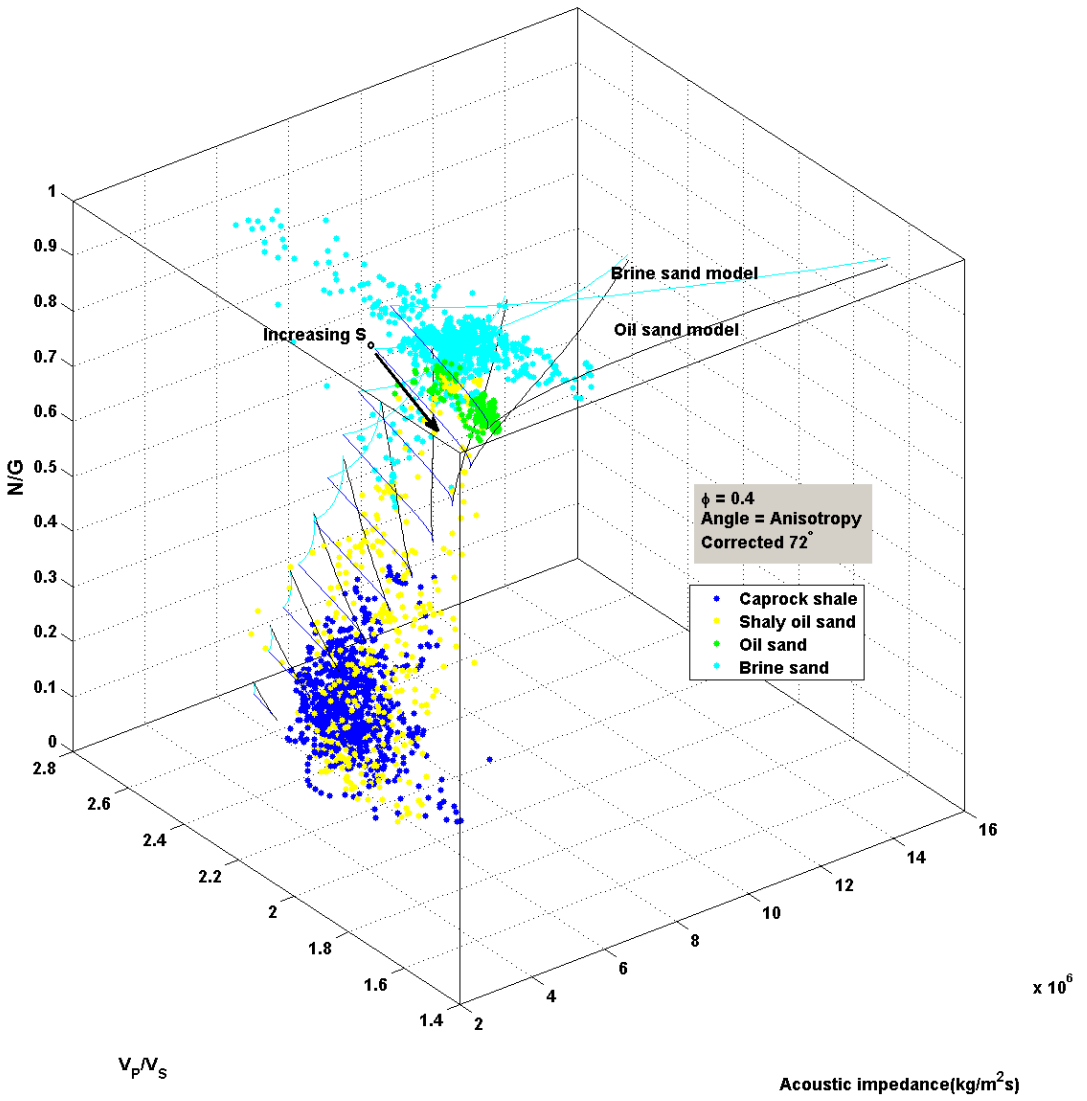

Figure 4.12: 3D Cross-plot of AI versus V_P/V_S and NG. The rock physics template model is created using propagation angle of $0°$ (vertical RPT) for different net-to-gross and saturation. The sand porosity remains constant at 0.40 and the well log data from the target zone of the anisotropy corrected deviated well is superimposed on this model. The well log data follows a similar trend as that seen on the vertical well in figure 4.10.

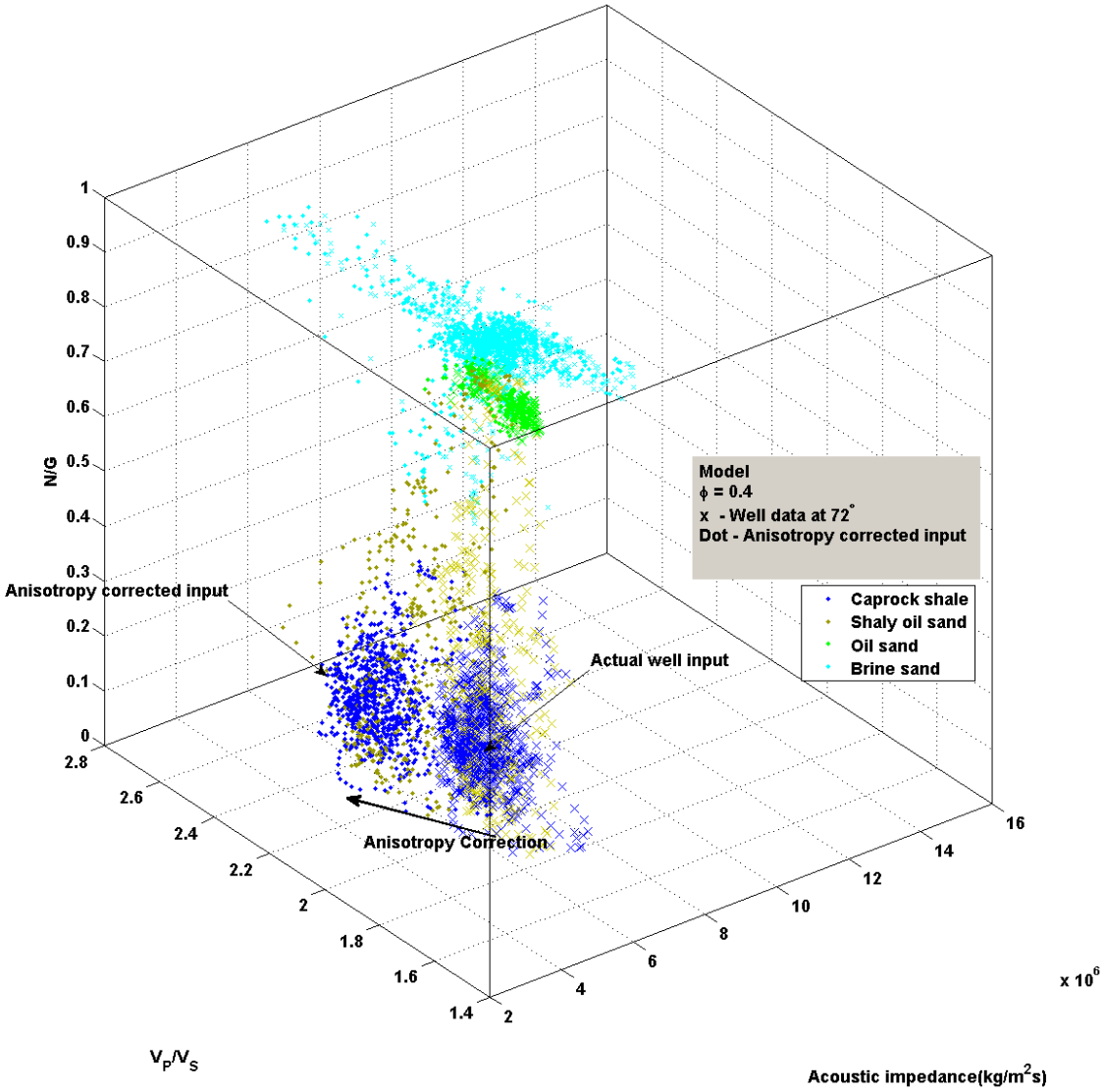

Figure 4.13: 3D Cross-plot of AI versus V_P/V_S and NG. The rock physics template model is ignored in order to easily observe the trend of the two wells plotted.. The deviated and anisotropy corrected wells are both plotted on this template and the variation on the trend can be observed as a result of anisotropy.

4.2 AVO inversion results

Following the AVO inversion procedure discussed in section 3.5, the cross-plot of the estimated AI and V_p/V_s from this inversion process are superimposed on the rock physics model in figure 3.6 and 3.7. This process is performed for the two vertical wells and the observed trends and difference in net-to-gross of the two wells. Figure 4.14 shows the calibrated AVO intercept for Horizon AVO attribute slides for the top of the reservoir at Alvheim field. The slide shows the location of the two

study wells. The blue and the black rectangles are the AVO anomalies around the two wells and the red rectangle represents the background trend. The AVO anomalies and background tend are cross-plot on a plot of intercept versus gradient as shown in figure 4.15. The inverted AI and V_p/V_s for the two vertical wells are superimposed on the vertical rock physics template with models of net-to-gross model and varying saturation as shown in figure 4.16 to 4.18.

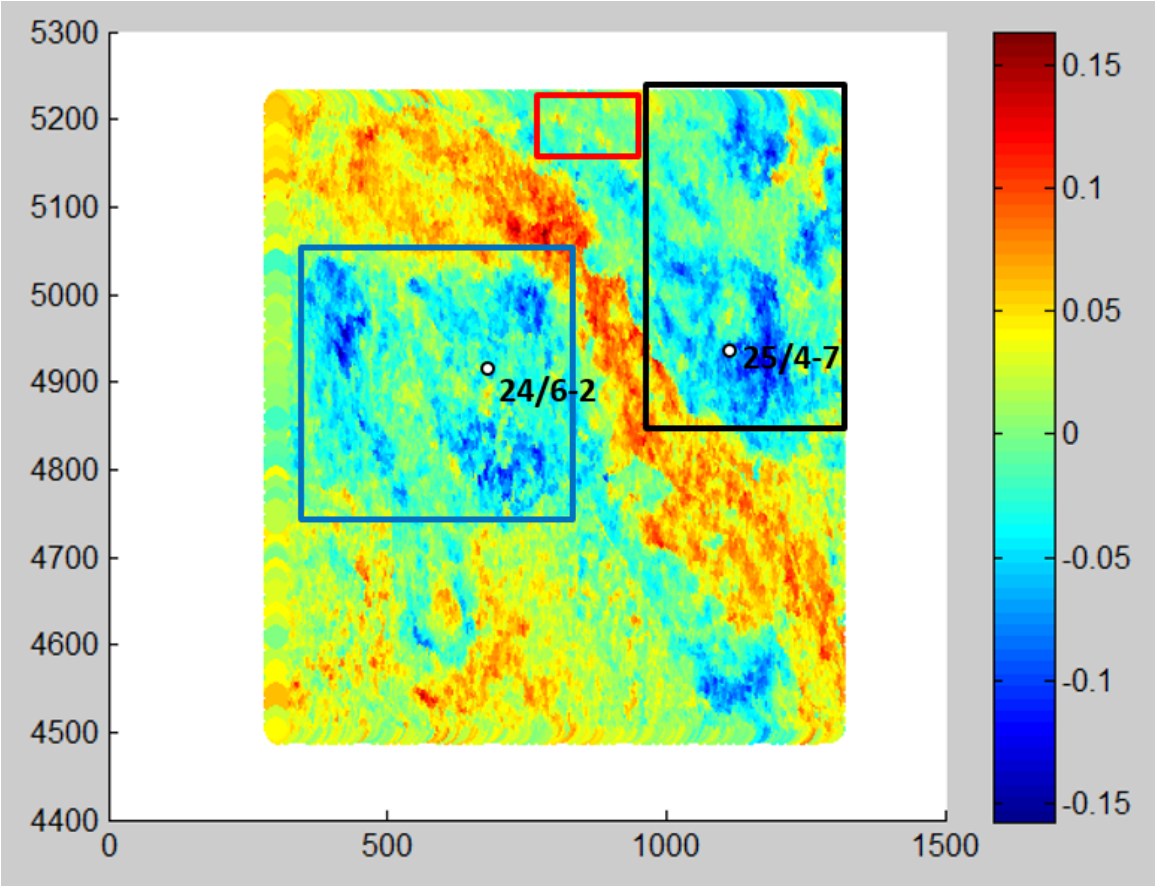

Figure 4.14: Calibrated AVO intercept for Horizon AVO attribute slides for the top of the reservoir at Alvheim field. The slide shows the location of the two vertical wells(well 25/4-7 and well 24/6-2). The blue and the black rectangles are the AVO anomalies around the two wells and the red rectangle represents the background trend.

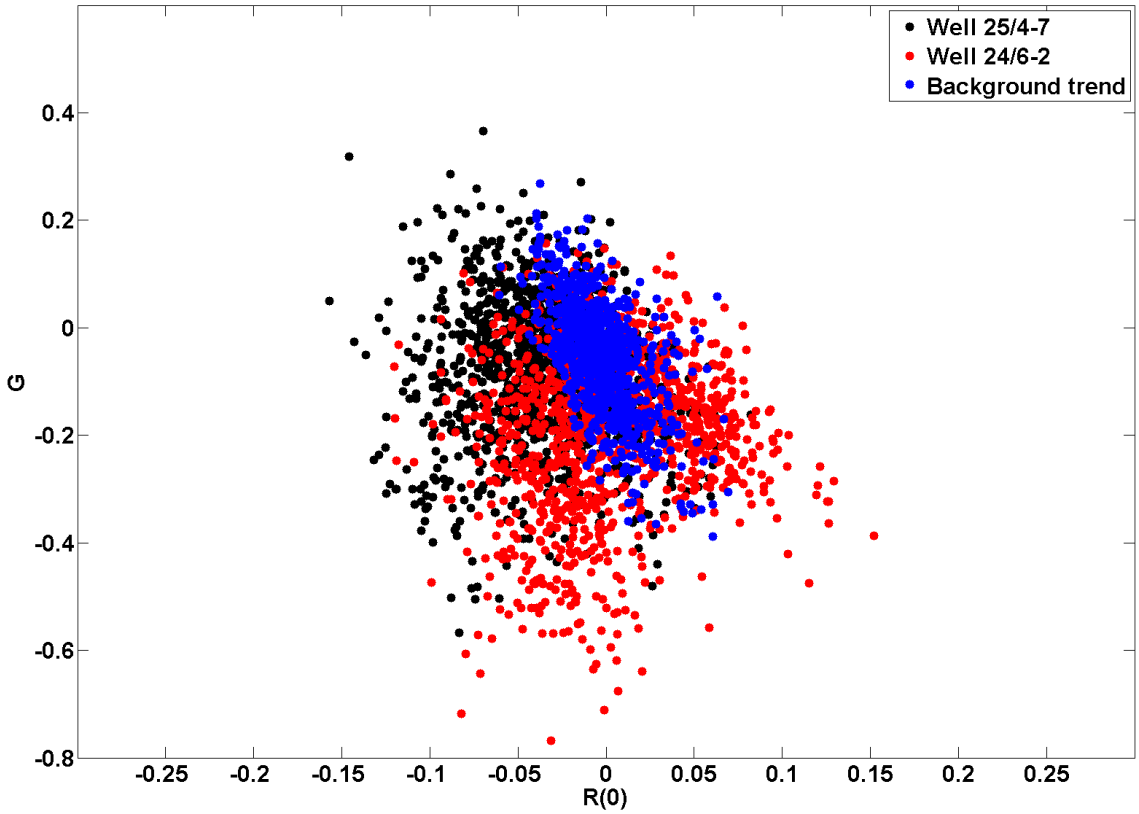

Figure 4.15: Intercept versus gradient cross-plot indicating background trend and the AVO anomalies around the two vertical wells(well 25/4-7 and well 24/6-2).

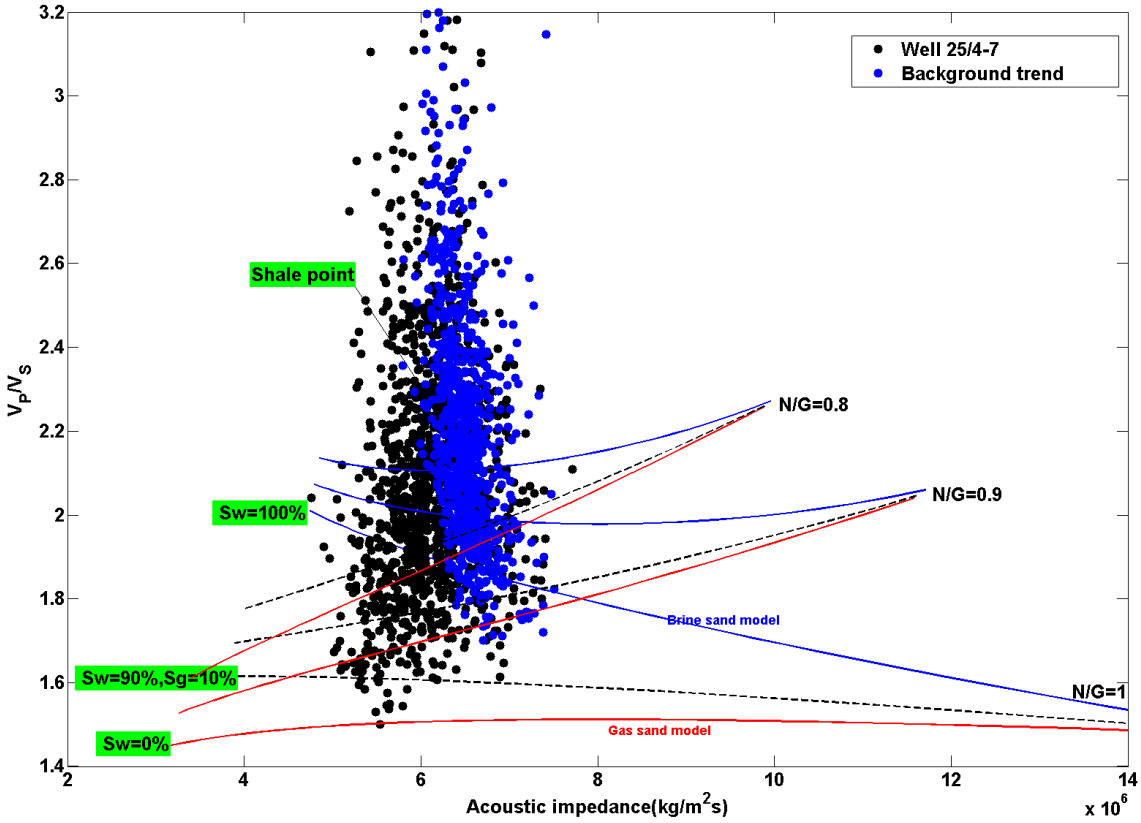

Figure 4.16: Vertical rock physics template with models of different net-to-gross ratios and varying saturation. The inverted AI and V_p/V_s from the zero offset reflectivity and gradient are superimposed on this template for anomalies around the vertical well 25/4-7 and the background trend

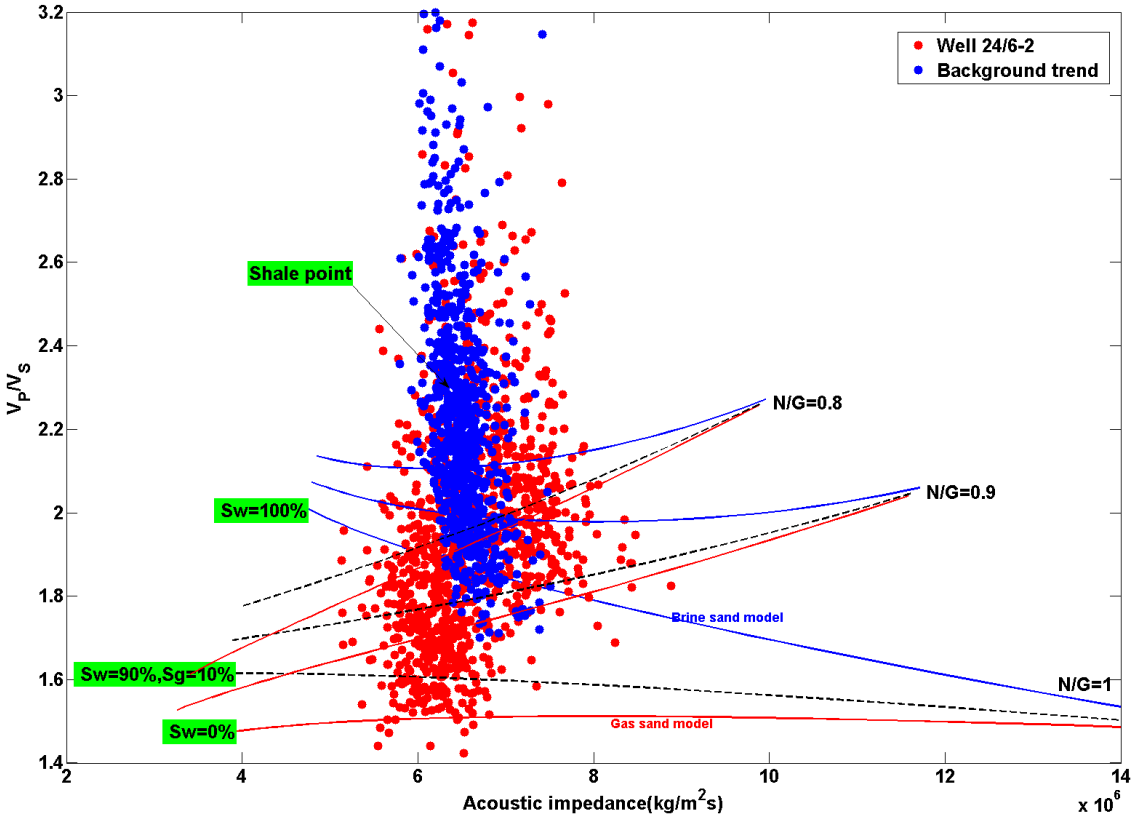

Figure 4.17: Vertical rock physics template with models of different net-to-gross ratios and varying saturation. The inverted AI and V_p/V_s from the zero offset reflectivity and gradient are superimposed on this template for anomalies around the vertical well 24/6-2 and the background trend

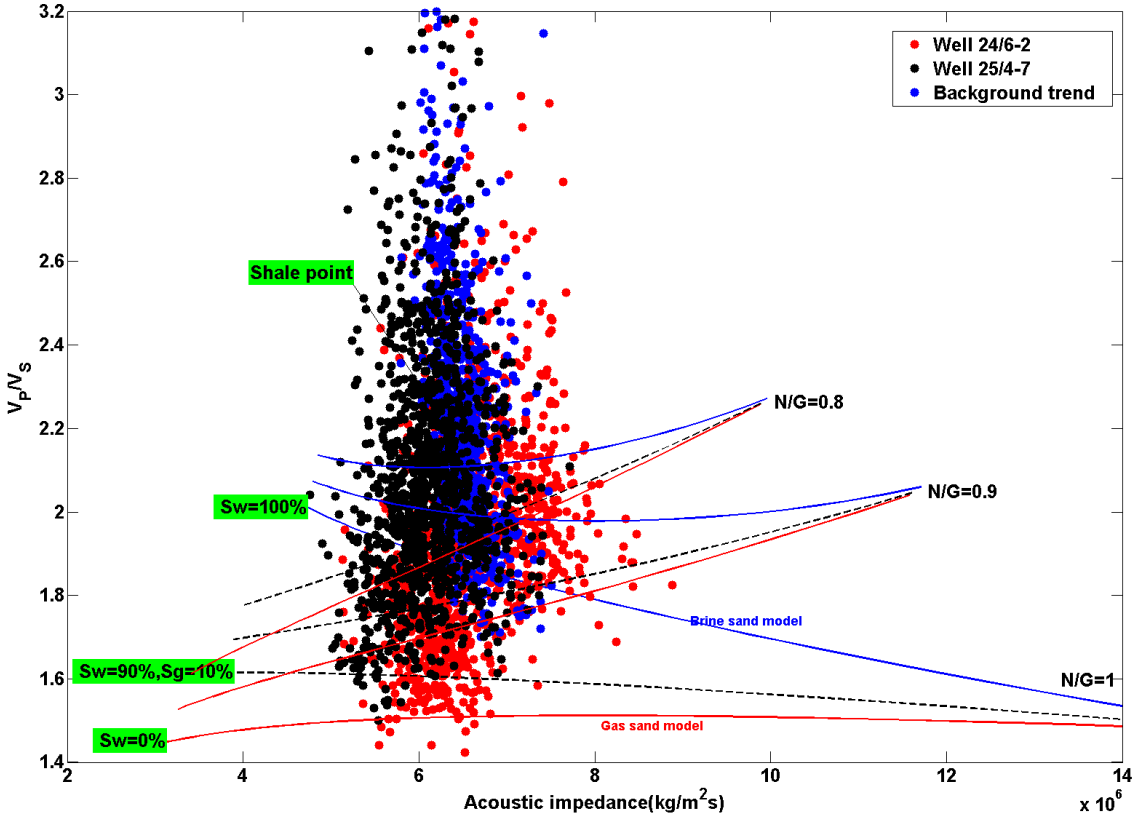

Figure 4.18: Vertical rock physics template with models of different net-to-gross ratios and varying saturation. The inverted AI and V_p/V_s from the zero offset reflectivity and gradient are superimposed on this template for anomalies around the two study wells and the background trend

Chapter 5

Discussions

This chapter is devoted to the interpretation of the observed trends and variation from the results of the analyses presented in the previous chapter. The study wells are from the North sea and all the wells penetrate oil and/or gas reservoirs. Anisotropy has significant effects on these reservoir as a result of heterogeneous sequence of the reservoir, which occurs at a much smaller scale compared to seismic wavelength.

Rock physics templates created for different net-to-gross at varying saturation in section 3.2 are applied in the interpretation of the observed trends and changes in reservoir parameters for the three studied wells. After accounting for anisotropy effects on the deviated well using the proposed method in section in 3.3, the corrected well is also superimposed on the rock physics model. The changes in the reservoir parameters as a result of this correction are then examined. The net-to-gross of the reservoir are not available on the well log data, however, I estimate the net-to-gross from the volume of shale (V_{sh}) from the well log data as explained in section 2.3. It is important to mention that the shale properties used for this study is chosen from the cap-rock shale above the reservoir and this might introduce certain errors in the result since the cap-rock shale properties are not also the same as that of the interbedded shale in the sequence.

The first well considered in this study is a vertical well that penetrate turbiditic oil and gas reservoir as shown in figure 4.1. This well is superimposed on a vertical rock physics template as seen in figure 4.2. The vertical rock physics model is created using propagation angle of 0° for models with three different net-to-gross(0.8, 0.9 and 1). For every net-to-gross, a 100% gas saturated model and 100% brine saturated model are created. Model with gas saturation of 10% is indicated by the black dashed line. It can be seen from this vertical RPT that the V_p/V_s ratios increase with decreasing net-to-gross for all porosity and saturation. The acoustic impedances however, decrease with decreasing net-to-gross for low porosity sands and to some certain extent increase with increasing N/G for high porosity sand. Based on this vertical rock physics template, it can be seen that it becomes difficult to differentiate fluid saturation effects from net-to-gross effect as a result of poor discrimination between fluid saturation and net-to-gross. For instance, an oil saturated shaly sand with N/G of 0.8 can be misinterpreted as a water saturated clean sand. From the superimposed well data, it can be

seen that the reservoir gas and oil saturated sand fit well for models with N/G of 0.9 and 1. The gas saturated sand as a result of heterogeneties spreads from above the 10% gas saturated model for clean sand(N/G=1) to region of gas model for sand of N/G of 0.9. It is therefore important to have the understanding of how the local geologic trends in term of the net-to-gross in order to enhance better interpretation from the rock physics template.

The second vertical well is considered next in this study. This well penetrate an oil reservoir as seen in figure 4.3. The well is also superimposed on a vertical RPT, however, since the reservoir contains no gas, a 100% oil saturated model and 100% brine saturated model are created for each net-to-gross model as shown in figure 4.4. The trends in this template follow the same pattern as the previous template. Focusing on the superimposed well data, it will be noticed that reservoir sands cluster in the models of N/G of 0.8 and 0.9. The oil saturated sands fit nicely with the oil sand model for N/G of 0.9, however, the shaly oil sands spread through models with N/G of 0.9, 0.8 and even lower N/G. This observed variations and trends will be of significance when comparing this well with deviated well.

The deviated well examined in this study is in close proximity with the vertical well that penetrate the oil reservoir as shown in figure 3.1. Therefore these two wells can be compared since both penetrate the same heterogeneous reservoir. The well is deviated between $45 - 73^{\circ}$ as seen on the well log in figure 4.5. The sonic velocities from the velocities are acquired at 72°. This well log data is superimposed on a horizontal rock physics model as seen in figure 4.6. This horizontal rock physics model is created in this case using propagation angle at which the sonic velocities of this well are acquired (72°) for models with three different net-to-gross(0.8,0.9 and 1). Unlike the vertical RPT, It is observed that there is better discrimination between the oil saturated sand model and brine saturated sand model irrespective of the N/G. However, differentiating sands with different N/G ratio becomes difficult. Considering well log data superimposed on this template, it will be observed that there is no separation between the brine sand, shaly oil sand and the cap-rock shale. Even though, the oil sands show small separation from the brine sand, the net-to-gross and cannot be accurately inferred. It can also be seen on the templates that shaly oil sands plot close to the gas sand and it even becomes difficult not just only to discriminate the net-to-gross but also the fluid saturation.

Performing anisotropy correction on the deviated well by employing the proposed method in section 3.3 consequently leads to the verticalization of the deviated well. It is important to mention that the anisotropy correction is dependent on the lithology. As it can be seen in figure 4.8, the velocities of anisotropic shales on the upper part of the well log are strongly affected by the correction, reducing

the velocities by as much as $400m/s$. The velocities in the shaly oil sands zone are moderately corrected. While the velocities in the oil and brine sand regions are relatively unaltered by the anisotropy correction. Ultimately, the anisotropy corrected deviated well has its velocities similar to that of the acquired velocities from the study vertical well.

The corrected well log is then superimposed on the vertical rock physics model as shown in figure 4.9 and it is observed that there is better discrimination of both fluid saturation and net-to-gross. The oil sands fall within N/G of 0.8-1 and the shaly oil sands match nicely for N/G of 0.9, 0.8 and even lower N/G. As seen on the template, there is better discrimination between brine sands and oil sands.

The question about the accuracy and preciseness of the proposed method for correcting anisotropy is examined using the 3D rock physics model of the cross-plot of AI versus V_p/V_s and N/G. Figure 4.10 shows the 3D rock physics model created for varying net-to-gross and saturation for the vertical well at constant porosity of 0.4. The superimposed vertical well shows a trend towards decreasing acoustic impedance as the N/G decrease and slight increase in V_p/V_s as the N/G increase. Following the same procedure, the deviated wells is plotted on 3D rock physics model created for varying net-to-gross and saturation at propagation angle of 72° with constant porosity of 0.4 as shown in figure 4.11. It is noticed that trend is different from that of a vertical well. The corrected well log is also superimposed on this template and it is observed that the trend follows similar pattern as that of the vertical well as shown in figure 4.12. In order to easily see the difference between the deviated and the anisotropy corrected well, I ignore the rock physics template as shown in figure 4.13. The anisotropy accounted for from the application of the proposed method is shown by the arrow indicated in figure 4.13.

Information about the lithology, net-to-gross, porosity and pore fluid of the study area are extracted from the zero offset reflectivity (R(0)) and AVO gradient (G) from the horizon AVO attribute data. The approach I consider is to invert for rock physics attributes from the available AVO attribute and examine the relationships between the two vertical wells based on how the attributes(variables) are grouped or clustered on the rock physics template in order to infer the net-to-gross and lithology of the reservoir. The AVO analysis is carried out assuming isotropic media. Figure 4.14 shows the calibrated AVO intercept for Horizon AVO attribute slides for the top of the reservoir at Alvheim field indicating the two study vertical wells. The anomalies around the wells are indicated by the blue and black rectangle and the background trend is indicated by the red rectangle. The AVO cross-plot of intercept and gradient are shown for the two wells in figure 4.15 and it can be seen how the anomalies deviated from the background. Based on the deviation from the background trend as seen

in figure 4.15, the top of the reservoir of well 24/6-2 have a class II AVO response whereas the other vertical well, well 25/4-7 shows a class III AVO anomaly.

The inverted acoustic impedance and V_p/V_s of well 25/4-7 and 24/6-2 are superimposed on the vertical rock physics template with models of different net-to-gross ratios and varying saturation as shown in figure 4.16 and 4.17 respectively. It is observed that these data points plot on models with different net-to-gross ratios. By superimposing the inverted acoustic impedance and V_p/V_s of the two wells on the same templates as shown in figure 4.18. It is interesting to see that the data points (indicated by the black dots) of well 25/4-7 fit nicely and have most of the clusters in the models with N/G of 0.8 and 0.9. Whereas, the data points (indicated by the blue dots) of well 24/6-2 fit nicely and have most of the clusters in the models with N/G of 1 and 0.9. However, one major limitation of this approach is that gas saturated sand may be misinterpreted as high net-to-gross reservoir sand. In figure 4.18, the porosity in well 25/4-7 seems to be slightly higher than the porosity in well 24/6-2.

Chapter 6

Conclusions

Velocities acquired in vertical wells are different from those acquired in deviated wells within the same depth limit of anisotropic reservoir. I have presented a methodology that correct for the effects of anisotropy, which consequently results in anisotropy corrected well with similar velocities as acquired vertical well. The proposed method is dependent on the lithology of the study reservoir. A limitation of the proposed methods is that it is only applicable to VTI media with horizontal or nearly horizontal beds. A good and improved well tie will be achieved using the anisotropy corrected well log with acquired vertical well. Also, discrimination of lithologies and fluid saturation on the rock physics template is improved as a result of the anisotropy correction. Further investigation is required for the application of the proposed method to other anisotropic symmetry such as orthorhombic and monoclinic.

Rock physics models are created for anisotropic heterogeneous sand-shale sequence. These models are varied as a function of angle, porosity, saturation and net to gross and are used for interpreting well log data from vertical and deviated wells. Anisotropic effect becomes more pronounced at high propagation angle and the variations of the geologic parameters are strongly influenced by the propagation angle. Thereby, making it important to account for these variation in order to attain a more precise reservoir characterization.

Horizontal and vertical rock physics templates are constructed for different net to gross at varying fluid saturation. Poor discrimination between fluid saturation and net-to-gross makes it difficult to differentiate between clean sand and heterogeneous sand with different fluid content in vertical RPT. AVO analysis performed in the studied area can better be improved by putting anisotropy into consideration. well 25/4-7 has reservoir sand with lower net-to-gross compared to reservoir sand in well 24/6-2.

References

Aki, K. and Richards, P. (1980). Quantitative seismology theory and methods.

Alkhalifah, T. (1997). Velocity analysis using nonhyperbolic moveout in transversely isotropic media. *Geophysics*, 62(6):1839–1854.

Alkhalifah, T. and Tsvankin, I. (1995). Velocity analysis for transversely isotropic media. *Geophysics*, 60(5):1550–1566.

Anderson, D. L. (1989). *Theory of the Earth*. Blackwell Scientific Publications.

Avseth, P., Mukerji, T., and Mavko, G. (2005). *Quantitative seismic interpretation: Applying rock physics tools to reduce interpretation risk*. Cambridge University Press.

Avseth, P., Mukerji, T., Mavko, G., and Dvorkin, J. (2010). Rock-physics diagnostics of depositional texture, diagenetic alterations, and reservoir heterogeneity in high-porosity siliciclastic sediments and rocks—a review of selected models and suggested work flows. *Geophysics*, 75(5):75A31–75A47.

Backus, G. E. (1962). Long-wave elastic anisotropy produced by horizontal layering. *Journal of Geophysical Research*, 67(11):4427–4440.

Banik, N. C. (1984). Velocity anisotropy of shales and depth estimation in the north sea basin. *Geophysics*, 49(9):1411–1419.

Castagna, J. P. and Swan, H. W. (1997). Principles of avo crossplotting. *The leading edge*, 16(4):337–344.

Connolly, P. and Kemper, M. (2007). Statistical uncertainty of seismic net pay estimations. *The Leading Edge*, 26(10):1284–1289.

Crampin, S. (1984). An introduction to wave propagation in anisotropic media. *Geophysical Journal International*, 76(1):17–28.

Dvorkin, J. and Nur, A. (1996). Elasticity of high-porosity sandstones: Theory for two north sea data sets. *Geophysics*, 61(5):1363–1370.

Foster, D. J., Keys, R. G., and Lane, F. D. (2010). Interpretation of avo anomalies. *Geophysics*, 75(5):75A3–75A13.

Gassmann, F. (1951). Elasticity of porous media. *Vierteljahrsschrder Naturforschenden Gesselschaft*, 96:1–23.

Golikov, P., Avseth, P., Stovas, A., and Bachrach, R. (2013). Rock physics interpretation of heterogeneous and anisotropic turbidite reservoirs. *Geophysical Prospecting*, 61(2):448–457.

Harris, P., Chazalnoel, N., and Americas, C. (2002). Anisotropic prestack depth migration: A case study. In *2002 SEG Annual Meeting*. Society of Exploration Geophysicists.

Hashin, Z. and Shtrikman, S. (1963). A variational approach to the theory of the elastic behaviour of multiphase materials. *Journal of the Mechanics and Physics of Solids*, 11(2):127–140.

Hilterman, F. (1990). Is avo the seismic signature of lithology? a case history of ship shoal-south addition. *The Leading Edge*, 9(6):15–22.

Hornby, B. E., Howie, J. M., and Ince, D. W. (2003). Anisotropy correction for deviated-well sonic logs: Application to seismic well tie. *Geophysics*, 68(2):464–471.

Ikelle, L. T. and Amundsen, L. (2005). *Introduction to petroleum seismology*. Society of Exploration Geophysicists Tulsa, OK.

Mindlin, R. (1949). Compliance of elastic bodies in contact. *J. Appl. Mech.*, page 259–268.

Ødegaard, E. and Avseth, P. (2003). Interpretation of elastic inversion results using rock physics templates. In *65th EAGE Conference & Exhibition*.

Rüger, A. (1998). Variation of p-wave reflectivity with offset and azimuth in anisotropic media. *Geophysics*, 63(3):935–947.

Rüger, A. (2001). *Reflection coefficients and azimuthal AVO analysis in anisotropic media*. Society of Exploration Geophysicists.

Shuey, R. (1985). A simplification of the zoeppritz equations. *Geophysics*, 50(4):609–614.

Stovas, A., Landrø, M., and Avseth, P. (2006). Avo attribute inversion for finely layered reservoirs. *Geophysics*, 71(3):C25–C36.

Thomsen, L. (1986). Weak elastic anisotropy. *Geophysics*, 51(10):1954–1966.

Thomsen, L. et al. (2002). *Understanding seismic anisotropy in exploration and exploitation*, volume 5. Society of Exploration Geophysicist.

Tsvankin, I. and Thomsen, L. (1994). Nonhyperbolic reflection moveout in anisotropic media. *Geophysics*, 59(8):1290–1304.

Vernik, L. (2007). Anisotropic correction of sonic logs in wells with large relative dip. *Geophysics*, 73(1):E1–E5.

Vernik, L., Fisher, D., and Bahret, S. (2002). Estimation of net-to-gross from p and s impedance in deepwater turbidites. *The Leading Edge*, 21(4):380–387.

Wang, Z. (2001). Fundamentals of seismic rock physics. *Geophysics*, 66(2):398–412.

Wild, P. et al. (2011). Practical applications of seismic anisotropy. *first break*, 29(5):117–124.

Winterstein, D. (1990). Velocity anisotropy terminology for geophysicists. *Geophysics*, 55(8):1070–1088.

Wood, A. (1941). A textbook of sound, 578 pp. *Bell, London*.

Appendix

MATLAB code for anisotropy modelling

```
%shale parameters
C11_shale = 19.7e9; C33_shale = 14.7e9; C13_shale = 11.1e9;
C44_shale = 2.6e9;  C66_shale = 4.7e9; rho_shale = 2.3;
%Sandstone parameters
Kfr_sand = 5e9; Kma_sand = 35e9; mu_sand = 3.5e9;
rhoma_sand = 2.65; % g/cm3
% Fluid parameters
Kw = 2.7e9; Ko = 1e9; Kg = 0.1e9;
rho_w = 1.02; rho_o = 0.75; rho_g = 0.2; % g/cm3
Sw =0.5; Sg = 0; So = 1-Sw-Sg; phi = 0.35;
theta = [0 10 20 30 40 50 60 70 80 90]; %group angle
NG = 0.5; % Net to gross
%fluid mixing law of wood
Kf = ((Sw/Kw)+ (Sg/Kg)+ (So/Ko))^-1;
% Gassmann equation and sandstone stiffness parameters
a = (Kfr_sand - Kma_sand)^2;
b = Kma_sand*(1-phi+(phi*Kma_sand/Kf)+ (Kfr_sand/Kma_sand));
C33_sand = Kfr_sand + (4/3 * mu_sand)+ (a/b);
C44_sand = mu_sand;  C11_sand = C33_sand;
C13_sand = C33_sand - (2*C44_sand);
C66_sand = C44_sand;
rho_f= (Sw*rho_w)+ (Sg*rho_g)+ (So*rho_o);
rho_sand = (phi*rho_f)+ ((1-phi)*rhoma_sand);
%Effective stiffness coefficients using backus
C33_eff = ((NG/C33_sand)+ ((1-NG)/C33_shale))^(-1);
C44_eff = ((NG/C44_sand)+ ((1-NG)/C44_shale))^(-1);
C13_eff = ((NG*C13_sand/C33_sand)+ ((1-NG)*C13_shale/C33_shale))*(
    C33_eff);
C11_eff = ((NG*(C11_sand- (C13_sand^2)/C33_sand))...
    + ((1-NG)*(C11_shale- (C13_shale^2)/C33_shale)))+ (C13_eff^2/C33_eff)
    ;
C66_eff = ((NG*C66_sand)+ ((1-NG)*C66_shale));
rho_eff = ((NG*rho_sand)+ ((1-NG)*rho_shale));
```

```
%% phase velocities
sin2 = sind(theta).*sind(theta); cos2 = cosd(theta).*cosd(theta);
VSH_theta = ((sin2.*C66_eff + cos2.*C44_eff)./rho_eff).^0.5;
d1= (C33_eff - C44_eff)^2;
d2= 2*((2*(C13_eff + C44_eff)^2) -(C33_eff - C44_eff)*(C11_eff + C33_eff
    -2*C44_eff))*sin2;
d3= ((C11_eff + C33_eff-2*C44_eff)^2 - 4*(C13_eff + C44_eff)^2)*sin2.*
    sin2;
D= (d1+d2+d3).^0.5;
VSV_theta = sqrt((0.5/rho_eff)*(C33_eff + C44_eff + ((C11_eff - C33_eff)
    *sin2) - D));
VP_theta = sqrt((0.5/rho_eff)*(C33_eff + C44_eff + ((C11_eff - C33_eff)*
    sin2) + D));
%% effective anisotropy paramters
epsilon =   (C11_eff - C33_eff)/(2*C33_eff)
delta = (((C13_eff + C44_eff)^2)-((C33_eff - C44_eff)^2))/((2*C33_eff)*(
    C33_eff - C44_eff))
gamma = (C66_eff - C44_eff)/(2*C44_eff)
%% PLOT
plot (theta,VP_theta,'MarkerSize',10,'Marker','.','LineWidth',2)
xlabel('Angles (Degrees)','FontWeight','bold');
ylabel('V_P(km/s)','FontWeight','bold')
title('Anisotropic P-Velocities','FontWeight','bold')
figure
plot (theta,VSH_theta,'MarkerSize',10,'Marker','.','LineWidth',2,'Color'
    ,[1 0 0])
hold on
plot (theta,VSV_theta,'MarkerSize',10,'Marker','.','LineWidth',2)
xlabel('Angles (Degrees)','FontWeight','bold');
ylabel('V_{SV}, V_{SH}(km/s)','FontWeight','bold')
title('Anisotropic S-Velocities','FontWeight','bold')
hleg = legend('V_{SH}','V_{SV}','location','northwest');
%%
figure
AI_theta = rho_eff * VP_theta; VP_VSH = VP_theta./ VSH_theta;
VP_VSV = VP_theta./ VSV_theta;
plot (AI_theta,VP_VSH,'MarkerSize',15,'Marker','.','Color',[1 0 0])
hold on
```

```
plot (AI_theta ,VP_VSV,'MarkerSize',15,'Marker','.')
xlabel('Acoustic impedance','FontWeight','bold');
ylabel('V_{P}/V_{S}','FontWeight','bold')
title('Modelling with increasing angle','FontWeight','bold')
hleg = legend('V_{SH}','V_{SV}','location','northwest');

% contour plots
figure
contourf(Sw, NG, epsilon)
colorbar
xlabel('Saturation','FontWeight','bold');
ylabel('Net to gross','FontWeight','bold')
title('\epsilon','FontWeight','bold','FontSize',30)

figure
contourf(Sw, NG, delta)
colorbar
xlabel('Saturation','FontWeight','bold');
ylabel('Net to gross','FontWeight','bold')
title('\delta','FontWeight','bold','FontSize',30)

figure
contourf(Sw, NG, eta)
colorbar
xlabel('Saturation','FontWeight','bold'); ylabel('Net to gross','
    FontWeight','bold')
title('\eta','FontWeight','bold','FontSize',30)

figure
contourf(Sw, NG, sig)
colorbar
xlabel('Saturation','FontWeight','bold');
ylabel('Net to gross','FontWeight','bold')
title('\sigma','FontWeight','bold','FontSize',30)
```

MATLAB code for Rock physics model

```
% Combined lamination and cementation modeling%
% Rock and Fluid properties
G=44e9; K=36.8e9; Kcl=25e9; Gcl=10e9; Koil=1e9;  Kbrine=2.75e9;
% Initiation of vectors
p4=[]; Vpsat3=[]; Vssat3=[]; Ksat3=[]; Gsat3=[]; Vpd3=[];
Vsd3=[]; ploty=[]; Keff=[]; AI_G=[]; PS_G=[];
%-------Input parameters--------
Vsh=  0.1;   %input('What is clay volume in sand beds)? ')
Vsst=1-Vsh;
d1= 0;            %Thickness of shale in the unit
d2= 1;            %Thickness of sand in the unit
por_shale = 0.3;           %Porosity of laminated shale in sand
por_shale2= 0.3;           %Porosity of interbedded shale
NG=d2/(d1+d2); NG_clr=(1-NG)*(1-por_shale2); pc=0.4;
n=20-34*pc+14*pc*pc; NG_qr=NG*(1-pc); NG_clm=NG_clr./(NG_qr+NG_clr);
NG_qm=NG_qr./(NG_qr+NG_clr);
%-----Mineral end point elastic parameters
Kmix=1./(((NG_qm)./K)+(NG_clm./Kcl));
Gmix=1./(((NG_qm)./G)+(NG_clm./Gcl));
Poiss_clay=(3*Kcl-2*Gcl)/(2*(3*Kcl+Gcl));
Poiss_qz=(3*K-2*G)/(2*(3*K+G));
Poiss_mix=(3*Kmix-2*Gmix)/(2*(3*Kmix+Gmix));
%Hertz-Mindlin modeling of high-porosity member elastic parameters
Khm_sh=((n^2*(1-pc)^2*Gcl.^2*20e6)./(18*3.14^2*(1-Poiss_clay).^2))
    .^0.33333;
Ghm_sh=( (5-4*Poiss_clay)./(5*(2-Poiss_clay)) ).*   (  (3*n^2*(1-pc)^2*
    Gcl.^2*20e6)./(2*3.14^2*(1-Poiss_clay).^2) ).^0.3333;
Khm_qz=((n^2*(1-pc)^2*G.^2*20e6)./(18*3.14^2*(1-Poiss_qz).^2)).^0.33333;
Ghm_qz=( (5-4*Poiss_qz)./(5*(2-Poiss_qz)) ).*   (  (3*n^2*(1-pc)^2*G
    .^2*20e6)./(2*3.14^2*(1-Poiss_qz).^2) ).^0.3333;
FactorB_sh=Khm_sh./(Kcl-Khm_sh) + 2.75e9./(pc.*(Kcl-2.75e9));
Khm_sh_br=Kcl*FactorB_sh/(1+FactorB_sh);
Ghm_sh_br=Ghm_sh;   por_sst2=[0:1:40];
for i=1:length(por_sst2)
    por_tot(i)=(NG*por_sst2(i)./100)+(1-NG)*por_shale2;
    por_sst(i)=por_sst2(i)./100;
```

```
34      Ktemp1_sand(i)=    (por_sst(i)/pc)/(Khm_qz+(4/3)*Ghm_qz);
        Ktemp2_sand(i)= ( 1-(por_sst(i)/pc) ) / (K+(4/3)*Ghm_qz);
36      Keff_sand(i)= (Ktemp1_sand(i)+ Ktemp2_sand(i))^(-1)-(4/3)*Ghm_qz;
        Gtemp1_sand(i) = ( por_sst(i)/pc) / ( Ghm_qz + (Ghm_qz/6)*( (9*
    Khm_qz+8*Ghm_qz)/(Khm_qz+2*Ghm_qz)) );
38      Gtemp2_sand(i) = (1-(por_sst(i)/pc)) / (G +(Ghm_qz/6)* (9*Khm_qz+8*
    Ghm_qz)/(Khm_qz+2*Ghm_qz) );
        Gtemp3_sand(i) = (Ghm_qz/6)*((9*Khm_qz+8*Ghm_qz)/(Khm_qz+2*Ghm_qz));
40      Geff_sand(i)=(Gtemp1_sand(i)+Gtemp2_sand(i) ).^(-1)-Gtemp3_sand(i);
        rho_sand(i)=2650*(1-por_sst(i));
42      Vp_sand_dry(i)=sqrt((Keff_sand(i)+(4/3)*Geff_sand(i))./rho_sand(i));
        Vs_sand_dry(i)=sqrt(   Geff_sand(i)./rho_sand(i));
44  Sw=0:0.1:1;
    for j=1:length(Sw)
46      Kfluid(j)=1./((1-Sw(j))./Koil + Sw(j)./Kbrine );
        rhofl(j)=(1-Sw(j))*750+Sw(j)*1050;
48      FactorB_qz(i,j)=Keff_sand(i)./(K-Keff_sand(i)) + Kfluid(j)./(por_sst
    (i)*(K-Kfluid(j)));
        Keff_sand_fl(i,j)=K*FactorB_qz(i,j)/(1+FactorB_qz(i,j));
50      Geff_sand_fl(i,j)=Geff_sand(i);
        rho_sand_fl(i,j)=2.65e3*(1-por_sst(i))+rhofl(j).*por_sst(i);
52      Vp_sand_fl(i,j)=sqrt( (Keff_sand_fl(i,j) + (4/3)*Geff_sand_fl(i,j))
    ./rho_sand_fl(i,j));
        Vs_sand_fl(i,j)=sqrt(   Geff_sand_fl(i,j)./rho_sand_fl(i,j) );
54  %---------- PART 3: Characterisitic shale properties
    Vp1=2348; Vs1=894; Rho1=2250;       AI1=Vp1.*Rho1;      PS1=Vp1./Vs1;
56  %---------- PART 4: Backus Average of sand-vector and shale
    f1=d1/(d1+d2);   f2=d2/(d1+d2);
58  C11(i,j)=f1*4*Rho1*Vs1^2*(1-(Vs1^2)/(Vp1^2))+f2*4*rho_sand_fl(i,j).*(
    Vs_sand_fl(i,j).^2).*(1-(Vs_sand_fl(i,j).^2)./(Vp_sand_fl(i,j).^2))
    + ( f1*(1-2*(Vs1^2)/(Vp1^2))+f2*(1-2*(Vs_sand_fl(i,j).^2)./(
    Vp_sand_fl(i,j).^2)))^2*(1/(f1/(Rho1*Vp1^2)+f2./(rho_sand_fl(i,j).*
    Vp_sand_fl(i,j).^2)));
    C33(i,j)=(1/(f1/(Rho1*Vp1^2)+f2./(rho_sand_fl(i,j).*Vp_sand_fl(i,j).^2))
    );
60  C44(i,j)=(1/(f1/(Rho1*Vs1^2)+f2./(rho_sand_fl(i,j).*Vs_sand_fl(i,j).^2))
    );
    C66(i,j)=f1*Rho1*Vs1^2+f2*rho_sand_fl(i,j).*Vs_sand_fl(i,j).^2;
```

```
C13(i,j)= ((f1*(1-(2*(Rho1*Vs1^2)/(Rho1*Vp1^2)))) + (f2.*(1-(2*(
    rho_sand_fl(i,j)*Vs_sand_fl(i,j).^2)/(rho_sand_fl(i,j)*Vs_sand_fl(i,
    j).^2))))).*(1/(f1/(Rho1*Vp1^2)+f2./(rho_sand_fl(i,j).*Vp_sand_fl(i,
    j).^2)));
Rhoav(i,j)=f1*Rho1+f2*rho_sand_fl(i,j);
%% phase velocities
theta = 0;
sin2 = sind(theta).*sind(theta);  cos2 = cosd(theta).*cosd(theta);
VSH_theta(i,j) = ((sin2.*C66(i,j) + cos2.*C44(i,j))./Rhoav(i,j)).^0.5;
D1(i,j)= (C33(i,j) - C44(i,j))^2;
D2(i,j)= 2*((2*(C13(i,j) + C44(i,j))^2) -(C33(i,j) - C44(i,j))*(C11(i,j)
     + C33(i,j)-2*C44(i,j)))*sin2;
D3(i,j)= ((C11(i,j) + C33(i,j)-2*C44(i,j))^2 - 4*(C13(i,j) + C44(i,j))
    ^2)*sin2.*sin2; D(i,j)= (D1(i,j)+D2(i,j)+D3(i,j)).^0.5;
VSV_theta(i,j) = sqrt((0.5/Rhoav(i,j))*(C33(i,j) + C44(i,j) + ((C11(i,j)
     - C33(i,j))*sin2) - D(i,j)));
VP_theta(i,j) = sqrt((0.5/Rhoav(i,j))*(C33(i,j) + C44(i,j) + ((C11(i,j)
    - C33(i,j))*sin2) + D(i,j)));
AI_theta(i,j) = Rhoav(i,j) * VP_theta(i,j);
VP_VSH(i,j) = VP_theta(i,j)./ VSH_theta(i,j);
VP_VSV(i,j) = VP_theta(i,j)./ VSV_theta(i,j);
end;
end;
ploty= VP_VSH;  plotx= AI_theta;
figure
pbsm = plot (plotx(:,11),ploty(:,11));
hold on
pgsm = plot (plotx(:,1),ploty(:,1),'Color',[1 0 0]);
hold on
pbgsm = plot (plotx(:,10),ploty(:,10),'k--');
figure % 3D PLOTS
ng_2= plotx - plotx+1; plot3 (plotx(41,:),ploty(41,:),ng_2(41,:));
hold on
plot3 (plotx(:,11),ploty(:,11),ng_2(:,11),'r');
plot3 (plotx(:,1),ploty(:,1),ng_2(:,1),'k');
hold off
```

MATLAB code for AVO inversion

```
load 'alvheim_data.mat'
Ro = seism_calibrated_2547(:,1);
Go = seism_calibrated_2547(:,2);
xline = seism_data_horiz_Alvheim(:,5);
inline = seism_data_horiz_Alvheim(:,4);
TWT = seism_data_horiz_Alvheim(:,3);
TWT2 = TWT(1:45090);
AI_lista = 6.54e6; % km/s*g/cm3
AI_cal = (AI_lista.*(Ro +1))./(1-Ro);
z1 = find(xline>4850 & xline<5050 & inline>1000 & inline<1300); % well
    25/4-7
z2 = find(xline>4720 & xline<5220 & inline>300 & inline<800); % well
    24/6-2
z3 = find(xline>4700 & xline<4800 & inline>1000 & inline<1200); % bg
Poisson_lista = 0.39; Poisson_cal = Poisson_lista + (4/9).*(Go + Ro);
a = 2-(2.*Poisson_cal);  b = 1-(2.*Poisson_cal); PS = (a./b).^0.5;
Roii2 = Ro(z2); Goii2= Go(z2);
plot(Roii2(1:15:end),Goii2(1:15:end),'.')
hold on
Roii3 = Ro(z3); Goii3= Go(z3);
plot(Roii3(1:end),Goii3(1:end),'r.')
axis([-0.3 0.3 -0.8 0.6])
xlabel('R(0)','FontWeight','bold');
ylabel('G','FontWeight','bold')
```